

2015

Annual Report Jahresbericht

**Remote Sensing
Technology Institute**

Department
Atmospheric Processors



Published by **German Aerospace Center (DLR)**
A member of the Helmholtz Association

Remote Sensing Technology Institute
Institut für Methodik der Fernerkundung (IMF)

Department
Atmospheric Processors (IMF-ATP)

Department
Head Prof. Dr. Thomas Trautmann

Editorial Team Prof. Dr. Thomas Trautmann
Dr. Manfred Gottwald

Layout Dr. Manfred Gottwald

Cover Bromine oxide at the end of the polar winter in 2014. Each view shows one month from March to May (Arctic) and October to December (Antarctica). The annual "bromine explosion" causes dense plumes of BrO over areas covered with sea ice. The full picture (see chapter 4.1) comprises 8 years of atmospheric sounding from 2007-2014.

Contents

1. Foreword	3
2. Atmospheric Remote Sensing – Missions and Sensors	5
2.1 SCIAMACHY Phase F Processor Development	5
2.2 SCIAMACHY Operations Support Phase F	10
2.3 The Sentinel-4 Level 2 Project	12
2.4 The Sentinel-5 Precursor Level 2 Project	14
2.5 MERLIN Level 0-1 Data Processing	17
3. Atmospheric Remote Sensing – Methods	19
3.1 Operational Atmospheric Composition SAF Trace Gas Column Products from GOME-2	19
3.2 Atmospheric Methane with SCIAMACHY: First DLR Operational Level 2 Data	21
3.3 Improvement of Total and Tropospheric NO ₂ Column Retrieval for GOME-2	23
3.4 Validation of Carbon Monoxide Vertical Column Densities Retrieved from SCIAMACHY Infrared Nadir Observations	25
3.5 Long-term Time Series of Satellite Based Tropical Tropospheric Ozone Columns	27
3.6 Improved OCRA Cloud Fraction Retrieval Over Bright Surfaces	29
3.7 Cloud Top Height and Optical Depth Retrieval using ROCINN	31
3.8 ADM-Aeolus Mie and Rayleigh Algorithm Performance Assessment	33
3.9 Development of Atmosphere-Water Coupled Radiative Transfer	34
3.10 First Retrieval Results of Atmospheric Temperature from ML-CIRRUS Campaign	36
3.11 Py4CATS – Python Tools for Computational Atmospheric Spectroscopy	38
3.12 A Look Into Various Regularization Parameter Selection Methods	40
3.13 The Invariant Imbedding T-Matrix Approach: Revision	42
3.14 A Combination of Rayleigh Scattering and Mach-Zehnder Interferometry to Violate the CHSH-Inequality	43
4. Atmospheric Remote Sensing – Applications	44
4.1 Bromine Oxide in the Polar Atmosphere	45
4.2 GOME-2 Volcanic SO ₂ Retrieval	47
4.3 Modeling Air Pollution in Beijing: Emission Reduction versus Meteorological Influence	49
4.4 The ESA-CCI GOME-type Total Ozone Essential Climate Variable	52
4.5 Analysis of MAX-DOAS measurements at UFS	55
4.6 Space-borne Remote Sensing of the Polar Atmosphere	58
4.7 Analysis of the Jacobian Matrices for the Atmospheres of Exoplanets	60
5. Documentation	63
5.1 Books and Book Contributions	63
5.2 Journal Papers	63
5.3 Conference Proceeding Papers and Presentations	64
5.4 Attended Conferences	68
5.5 Academic Degrees	69
Abbreviations and Acronyms	71

1. Foreword

With the current version of our annual report we have reached a milestone – one and a half decade of summarizing what we achieved in atmospheric remote sensing. This time span of 15 years covers almost the entire period our department exists. When the Remote Sensing Technology Institute was founded as one of the two partners of what today is DLR's *Earth Observation Center*, the goal was to establish a team which can excel in the development, implementation and application of methods for the retrieval of atmospheric parameters from space-borne remote sensing data.



The first annual report for the year 2001 was issued in a time when Europe, and we, had only a small stake in that field. Then, GOME on ERS-2 had proven that it provides reliable data for the monitoring of ozone. Other trace gases were on the wish list for being retrieved but required still considerable efforts by us and our national and international cooperation partners. With SCIAMACHY being readied for launch on the ENVISAT platform, a new and challenging instrument awaited our involvement. It exceeded expectations by far and when SCIAMACHY disappeared from the screens with the loss of ENVISAT in 2012, it had helped to strengthen our capabilities substantially. This is also true for our current sensors "of choice", GOME-2 on MetOp-A and MetOp-B. In the coming year these two atmospheric instruments will be joined by a third copy of GOME-2, ESA's Sentinel-5 Precursor mission and EUMETSAT's Sentinel-4 and Sentinel-5 undertakings. They will all contribute to the field of atmospheric composition. ESA's wind

mission ADM-Aeolus shall for the first time apply the tool of active atmospheric remote sensing on a European mission. Shortly later, DLR, together with CNES, will introduce the active approach on MERLIN for the retrieval of knowledge about the methane concentrations in the Earth's atmosphere. In all these projects our department either already contributes significantly or acquires considerable responsibilities in the corresponding ground segments.

This increase in atmospheric remote sensing opportunities is certainly reflected in the sequence of annual reports. While the contributions for the first issue only covered 32 pages, they now fill almost twice as much. Since 2001, many colleagues have contributed to our annual reports. Some of them are still active members of our department, some have taken on new tasks and several have meanwhile concluded their professional careers. The benchmark of 15 issues is a good opportunity to again acknowledge their past contributions. In the same sense we also like to thank our current staff for their efforts and achievements in the past year and their contributions to the present report.

Prof. Dr. Thomas Trautmann
Dr. Manfred Gottwald

2. Atmospheric Remote Sensing – Missions and Sensors

2.1 SCIAMACHY Phase F Processor Development

G. Lichtenberg, B. Aberle, A. Doicu, S. Gimeno García, S. Gretschan, M. Meringer, F. Schreier, D. Scherbakov, S. Slijkhuis

In the framework of the phase F activities of the SCIAMACHY Quality Working Group (SQWG) we continued our efforts for further improvements for both the level 0-1b and the level 2 processors.

Level 0-1b processor

Level 0-1b processing provides calibrated radiances. The calibration of the data is based on a combination of on-ground thermal vacuum measurements, on-ground ambient measurements (to correct for the different incidence angles of light) and in-flight measurements. Currently processor version V8.02 is operational and the corresponding data will become available in 2016. Table 2-1 lists the new developments for version V8 together with the changes planned for the next processor version 9. Its implementation started in 2015 and will proceed through 2016.

Change	Description
Version 8 (product release 2016)	
Stray light channel 3-8	Extend matrix correction approach
Memory effect correction limb	Improve the estimate of signal
PMD scaling non-linearity	Improve scaling for low signal cases
Hot pixel limb	More robust hot pixel detection
SAA check	Switched off for Etalon, not needed
Dark selection	Implement a selection option
New key data	New key data used for calculation
Degradation correction	Mirror model from SRON used to correct degradation
PMD m-factor correction	Included in level 1b product
Version 9 (planned release 2017)	
Degradation correction	Better correction from re-analysis of on-ground and in-flight calibration data
Bad pixel mask	Based thresholds on individual pixels instead of channel wide thresholds
Dark correction	Improve dark correction by using in-flight data for whole mission
Spectral calibration SWIR	Improve spectral calibration of the SWIR channels 6-8
Polarization calibration	Investigate improvement of the polarization correction
netCDF data format	Change format of the level 1 data to the standard netCDF format
Pointing	Improve misalignment correction

Table 2-1: Summary of changes for the coming Level 0-1 processor

Level 1b-2 processor

The Level 1b-2 processor delivers geophysical products processed from the level 1b product. For version 6 of the processor the following changes had been implemented:

- update of the development environment
- update of the AAI algorithm now using calculated ozone values
- introduction of cloud/ice separation
- introduction of noctilucent clouds (NLCs) in the limb cloud MDS
- introduction of nadir formaldehyde (HCHO)

- introduction of nadir glyoxal (CHOCHO)
- introduction of methane (CH₄) (see also chapter 3-2)
- extension of limb ozone profile upwards of 45 km
- introduction of tropospheric nitrogen dioxide (NO₂) total column from limb-nadir matching

The introduction of the limb-nadir matching required some re-structuring of the processor architecture. In the previous versions limb and nadir states were processed independently and in parallel on several computational nodes. The limb-nadir matching requires both types of measurements: Simply put, a stratospheric column is derived from a summation of appropriate limb measurements. Subsequently the nadir measurement of the same volume of air is subtracted from the stratospheric column which yields the tropospheric column (see Fig. 2-1).

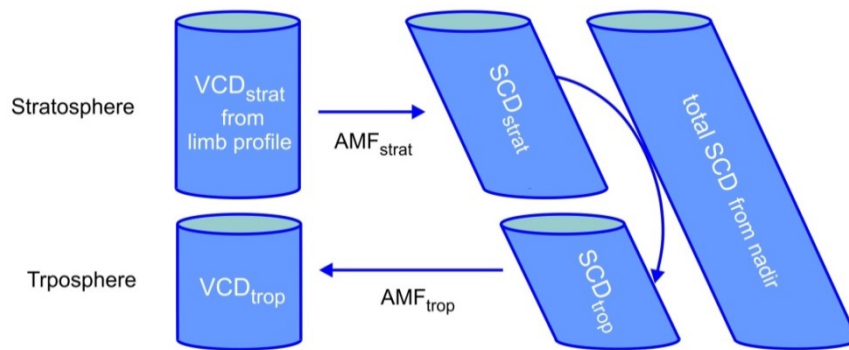


Fig. 2-1: Basic principle of limb-nadir matching as applied for tropospheric NO₂ retrieval.

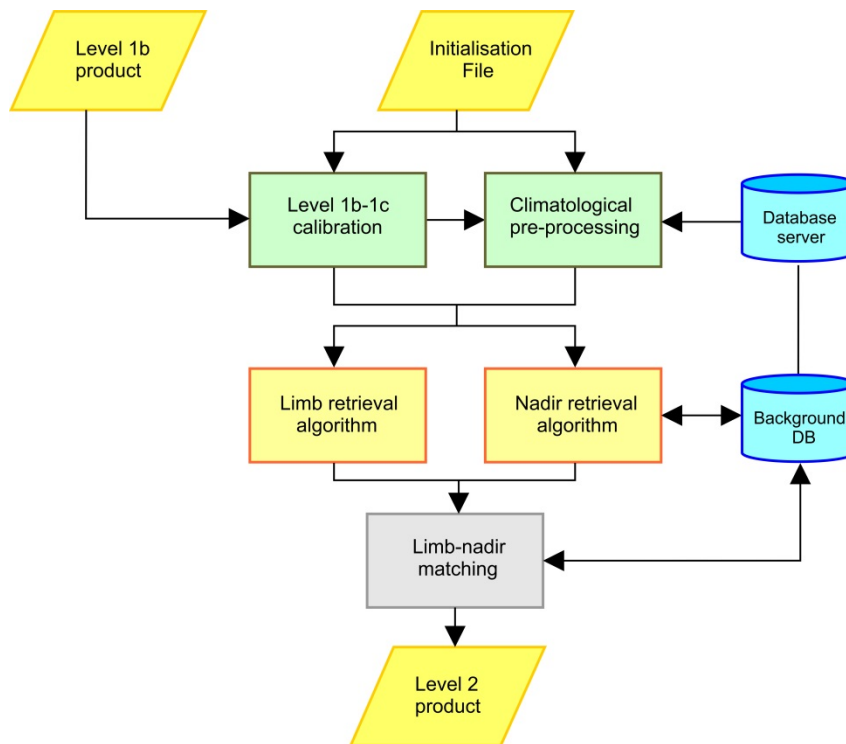


Fig. 2-2: Flowchart of the SCIAMACHY level 1b-2 processor with the newly integrated limb-nadir matching algorithm.

Technically the algorithm was implemented as a post-processing step: The parallel processing was still used for total trace gas columns, profiles and other geophysical parameters. However, after that step an additional limb-nadir processing module was introduced (see Fig. 2-2). This approach minimized the processing time and all the results from the limb and nadir retrievals were available for the retrieval of tropospheric columns. Because the selected setup is generic, the current implementation for tropospheric NO₂ will also be used for other tropospheric columns.

Level 1b-2 feedback in verification (example: CO retrieval)

Operational processors evolve constantly to be always state of the art. Usually the processing is split into a level 0-1b chain that produces radiances from raw data and a level 1b-2 chain that generates the geophysical products. This complicates the development and the verification of the processors. Therefore we developed an optimized scheme to ensure the correct implementation of the algorithms and to separate the effect of level 0-1b induced changes on level 2 data from the effect of level 1b-2 algorithm changes. For this purpose the verification occurs in two steps

- Check the correct implementation of each level 1b-2 algorithm using the current (operational) level 1b products derived by the operational level 0-1b processor.
- After step 1 was successfully achieved, use the now frozen level 1b-2 processor with the new level 1b products from the updated level 0-1b processor to identify changes.

The vanishing CO

The second test step for the CO total column for the processor combination level 0-1b V8 and level 1b-2 V6 showed that using the new level 1b products, the total columns of CO were a factor 3 smaller compared to the previous product using level 1b V7 product (see Fig. 2-3). The level 1b-2 CO algorithm itself had remained unchanged, therefore the cause of the different values had to be found in the change of the level 0-1b algorithms and their impact on the CO retrieval.

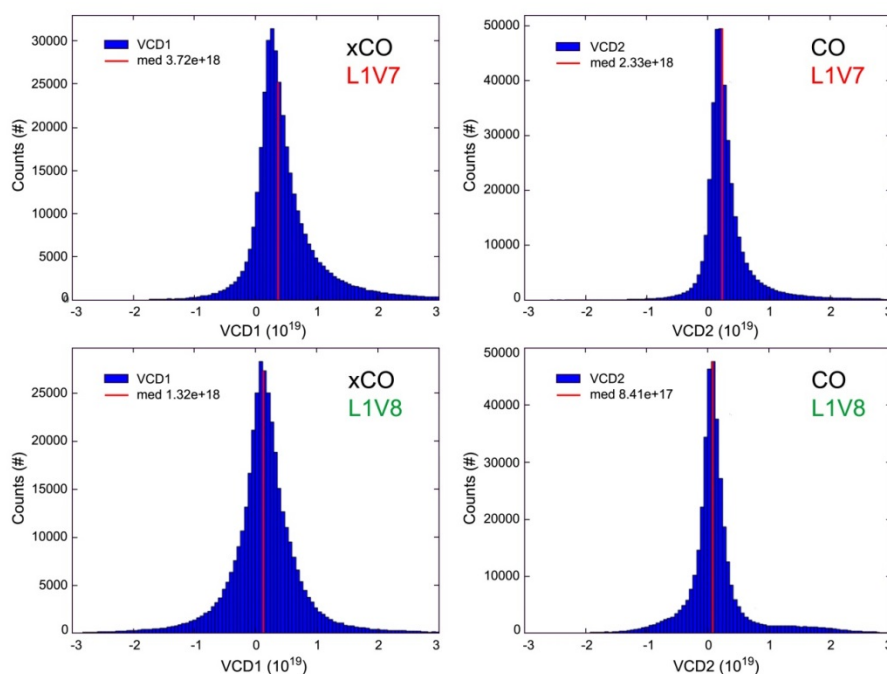


Fig. 2-3: Histogram of CO values from the verification data set with xCO (left) and CO (right).

For the coming data products, the unphysical CO values were corrected by adjusting the level 1b-2 fit settings. An evaluation based on 2004 data demonstrated that the CO values are again in a reasonable range and show the expected structures.

While the adjusted CO level 1b-2 algorithm delivered again reliable results, it was still required to identify the level 0-1b modification responsible for the decrease of the CO results by a factor of 3. Algorithm changes especially important for the SWIR range, when going from V7 to V8, included

- adjustment of the dark correction to exclude problematic measurements from the dark fit
- update of the radiometric calibration data
- introduction of a new degradation correction

First study results

Initially the investigation used the so-called "verification data set", produced for checking the correct implementation of the algorithms. For V7 it comprises 180 orbits from the years 2002-2008. The V8 dataset was extended to cover also the following years. Note that the datasets are not evenly distributed over the years (see Fig. 2-4).

Our study compared the following calibration parameters: Fixed Pattern Noise (FPN), leakage current and reflectances. Additionally we also investigated changes in the dead and bad pixel mask (Fig. 2-5). While this algorithm had not been modified, the data that are used to determine the bad pixels had changed. We performed a one-to-one orbit comparison for all datasets which were found valid in both versions (150 orbits).

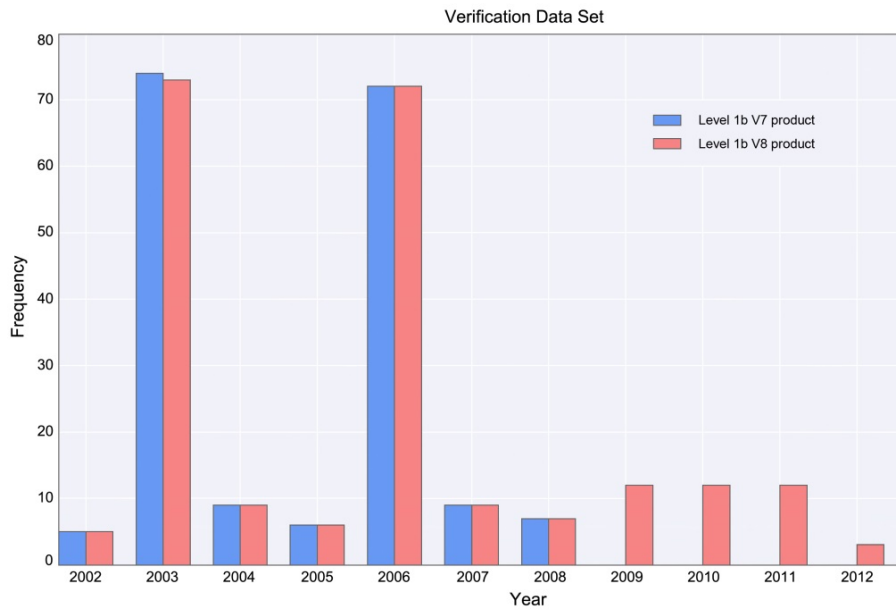


Fig. 2-4: Distribution of verification data sets.

The dead and bad pixel mask exhibited some changes. However they were insufficient to explain the observed factor 3 difference between the retrievals:

- 97.52% of the pixels in all observations were marked in the same way in both versions
- 2.05 % of the pixels were marked bad in V8 but not in V7 (Fig. 2-5) – note: the remaining percentage went from bad in V7 to good in V8

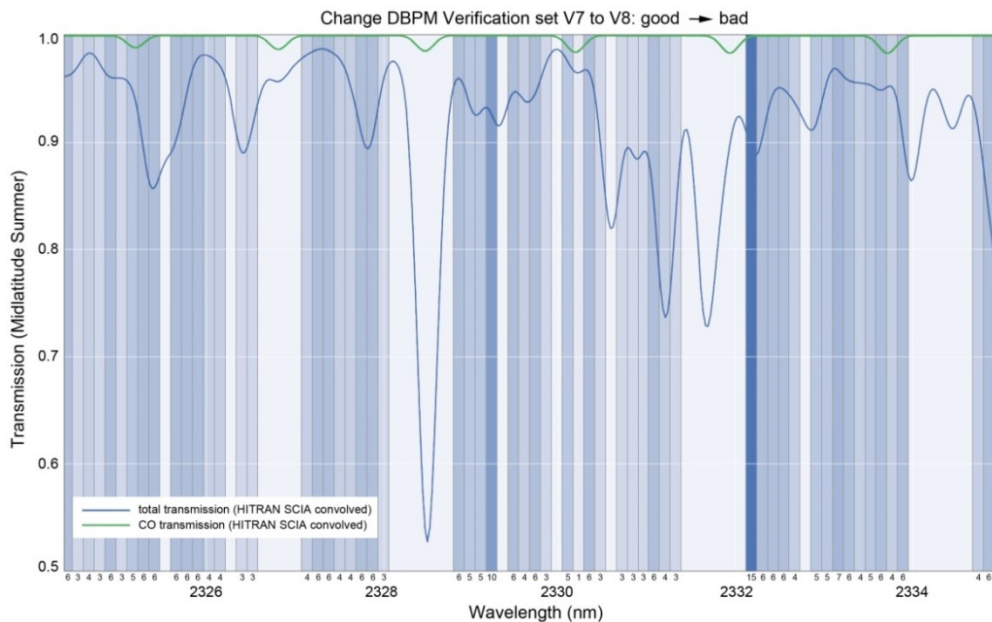


Fig. 2-5: Pixels that went from “good” to “bad” because of algorithm changes from V7 to V8 plotted on top of the atmospheric transmission in the CO retrieval window. The darker the shades the more pixel changes were observed in the data set. The numbers at the bottom show for how many orbits the pixel flag was changed.

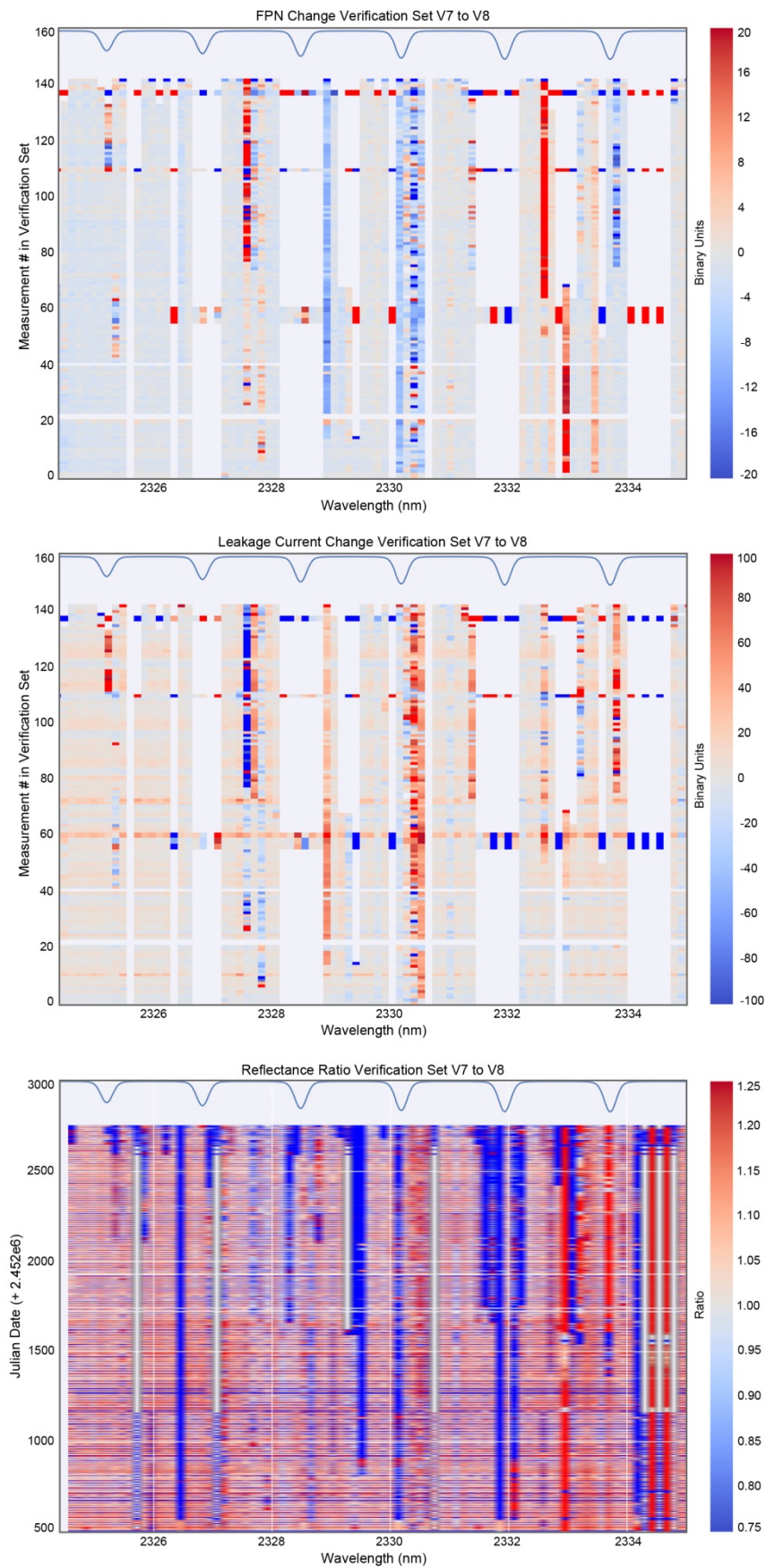


Fig. 2-6: Comparisons of calibration parameter changes with Fixed Pattern Noise (top), leakage current (middle) and reflectances (bottom). On top of the figures the scaled transmission of CO is shown. For the top figures we masked out bad pixels, for the reflectances we left them in to show their time evolution. The measurement number in the first two panels is equivalent to a time sequence.

On the other hand, fixed pattern noise and leakage current show a significant change for nearly all observations of the dataset near 2328 nm and near 2330 nm (Fig. 2-6). An earlier study using synthetic spectra had proven that perturbations of the radiance for the pixels around the CO absorptions near 2330 nm, 2334 nm and 2325 nm can change the retrieval by a factor 10 or more. Particularly the absorption at 2330 nm has a strong impact on the retrieval. Therefore the change in these calibration parameters had most likely triggered the observed behavior in the CO retrieval.

2.2 SCIAMACHY Operations Support Phase F

M. Gottwald, E. Krieg (TwIG), K. Reissig (IBR), J. How (TwIG), S. Noël, K. Bramstedt, H. Bovensmann (all IUP-IFE)

SCIAMACHY on ENVISAT had successfully studied the Earth's atmosphere between August 2002 and April 2012. The instrument's unique capabilities, including a wealth of observation geometries such as nadir, limb, Sun occultation and Moon occultation, made it an outstanding mission. A sensor with similar skills had not been in orbit before and is not planned in the near future. It is therefore well justified and considered indispensable to ensure availability of SCIAMACHY's measurement data for future users. Since these data had been acquired in various measurement configurations, it was commonly agreed that the long-term data preservation approach has to be accompanied by an activity aiming at storing also instrument operation and performance related knowledge for the same duration.

The SCIAMACHY Operations Support Team (SOST), formed by personnel from DLR's Earth Observation Center (EOC) and the Institute of Environmental Physics / Institute of Remote Sensing (IUP-IFE) at the University of Bremen was – in close cooperation with ESA – responsible for instrument operations and certain aspects of instrument performance monitoring. Since SOST-DLR covered most of the system related topics throughout the in-orbit phase, e.g. mission planning and command & control, a 2-year long phase F has been defined for SOST-DLR with the purpose to achieve suitable archiving for the related know-how. This phase F had started in May 2014 and will end in April 2016. It complements the phase F of the SCIAMACHY Quality Working Group (SQWG), which has the goal to further improve on algorithms, processors and products and prepare those for long-term data preservation.

Archived information content

The original archiving concept pursued a "classical" approach, i.e. collecting all specified information, storing them on dedicated accessible servers and providing associated documentation. However it became obvious very early in our work that this approach would quickly separate measurement data and corresponding operations information. Therefore SOST proposed a new concept by using the new level 1b product as "host" for the operations information. For this purpose the level 1b product will be expanded to include in a specific section the corresponding knowledge.

We have identified 9 chapters required to describe SCIAMACHY operations and performance for the period August 2, 2002 to April 8, 2012. These are

- **Reference Orbit:** Although the level 1b product provides in its header the state vector such that by using the ENVISAT CFI, orbit propagation and line-of-sight calculations can be performed with the most accurate orbit information, we included the reference orbit because it was the basis for all planning activities on SOST side.
- **ENVISAT Status:** Occasionally platform status changes impacted SCIAMACHY. Only these are archived. The events were usually related to platform anomalies or orbit manoeuvres.
- **SCIAMACHY Status:** This section provides information about the general status of the instrument. It includes availabilities, anomalies, specific non-routine measurement configurations and certain mission planning information.
- **SCIAMACHY Thermal:** Here the status of both the ATC and TC thermal system is reported, together with the PMD temperature. The ATC and TC information also includes the ATC and TC settings and the time when the settings have been changed.

- **SCIAMACHY Life Limited Items:** The temporal evolution of the LLI budgets can be found in this chapter. It is based on mission planning and SCIAMACHY history information which were a reliable prediction throughout the in-orbit phase.
- **SCIAMACHY State List:** The list of the 70 states stored on-board is given here. Changes in state titles only occur when a modification of the final flight state configuration changed the functionality of a state ID.
- **SCIAMACHY Measurement Tables:** This chapter provides the content of the 13 measurement state parameter tables. Each table is given with its full content of parameters for each orbit of the phase E history.
- **SCIAMACHY Housekeeping Telemetry:** The nominal instrument HK telemetry (readings with a rate of 1/16 Hz) was regularly provided by ESOC to SOST as 9 individual HK files. Each HK file contained HK parameters for a specific topic (e.g. detector thermal, OBM thermal, scanners, etc.). We include the content of all 9 HK files in the SCIAMACHY operations long-term archive.
- **SCIAMACHY Operations Change Requests:** In about 9 years of routine operations 50 OCRs were raised, issued, analysed and implemented. In order to give more insight into the purpose of a particular OCR, we also archive the request part of the OCR form. This allows to understand why certain instrument settings required changing in certain orbits.

No timelines and timeline related planning documents, e.g. the Orbit Sequence Definition File (OSDF), are stored. Because level 1b products are state-oriented, timeline information would not add to the understanding of the measurement data. Similarly, specific HK telemetry such as report formats or HK parameters read out with a rate $>1/16$ Hz, will not be preserved as part of the level 1b product. This telemetry was used for health & safety monitoring or supported anomaly analyses. It is not expected that corresponding activities will be required in the future.

Information for all 9 chapters has been assembled from various sources. These included

- planning documents exchanged between SOST and ENVISAT (FOS and PDGS),
- telemetry files received from FOCC,
- anomaly reports,
- instrument status information derived from the sources listed above,
- instrument status information derived from SOST's configuration controlled instrument Command & Control environment,
- and e-mails exchanged between SOST, ENVISAT and Astrium in cases of deviations from routine operations or implementation of non-standard procedures.

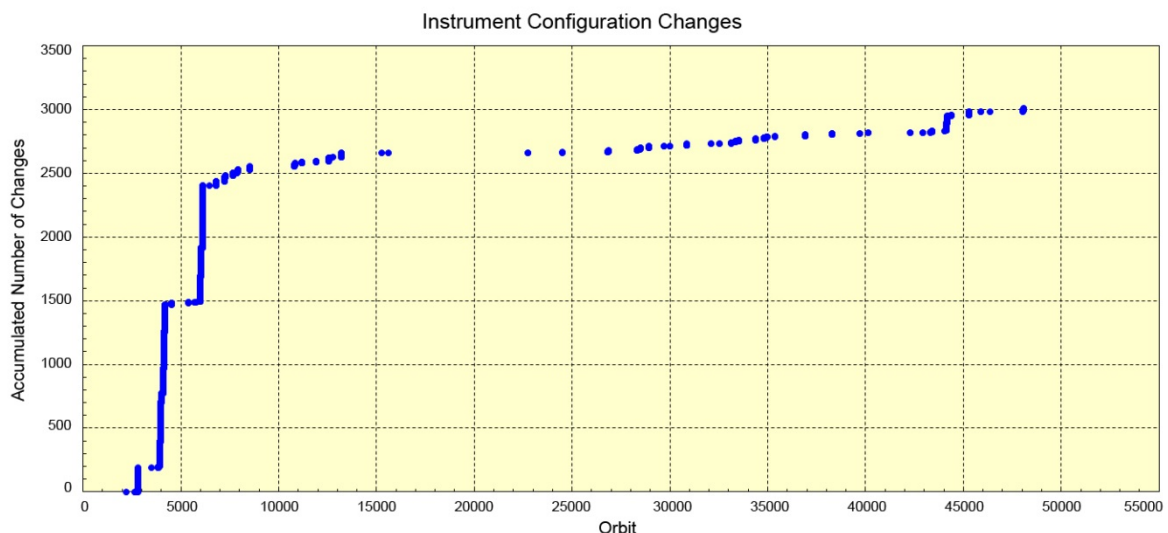


Fig. 2-7: Sequence of instrument reconfigurations since orbit 2204. Most of the modifications occurred in the early part of the routine operations phase. From about orbit 7000 on, the curve reflects the rate of issued Operation Change Requests.

Particular emphasis was put on the need to finally end up with a complete and conflict free sequence of operations information. A challenging aspect was here to generate the entire sequence of the 13 measurement parameter table configurations. Between orbits 2204 and 52867 3010 CTI uploads occurred in total (Fig. 2-7). Usually more than one CTI upload was executed in the idle phase prior to the start of the first timeline in an orbit. This resulted in only 464 orbits where the onboard configuration of SCIAMACHY was changed.

The level 1b product is orbit oriented. This is different for a considerable fraction of the operations and performance information which exists more on an "event-driven" basis (e.g. anomalies). Therefore, in all such cases the information had to be expanded between those "events" to reflect the complete status or configuration sequence.

In 2015 the content of all 9 chapters has been assembled, verified and stored in a database. This database serves as input when the new level 1b product will be generated. It also facilitates further usage of operations information. Since all 9 chapters together provide a rather complete view of about 10 years of SCIAMACHY operations, additional applications, e.g. calendar-type overviews, could emerge. This would form valuable add-ons to the presently specified SOST-DLR phase F results.

2.3 The Sentinel-4 Level 2 Project

D. Loyola, R. Lutz, M. Pedernana, and S4-Team

The Sentinel-5 Precursor (S5P), Sentinel-4 (S4), and Sentinel-5 (S5) missions are dedicated to monitoring the composition of the atmosphere for the operational Copernicus Atmosphere Services including the monitoring of air quality, stratospheric ozone and solar radiation, and climate monitoring. S5P will be a dedicated satellite operated by ESA whereas both S4 and S5 missions will be carried on meteorological satellites operated by EUMETSAT.

Sentinel-4 is a mission providing atmospheric composition data on European basis with an hourly revisit time, thereby covering the diurnal variation of atmospheric constituents (O₃, SO₂, NO₂, HCHO, CHOCHO, aerosol etc.). The S4 mission is defined as an Ultraviolet-Visible-Near-Infrared nadir (UVN) spectrometer on each of the geostationary Meteosat Third Generation Sounder (MTG-S) platforms.

Key features of the S4/UVN instrument are the spectral range from 305 nm to 500 nm with a spectral resolution of 0.5 nm for the UV visible, and 750 nm to 775 nm (oxygen A-band) with a spectral resolution of 0.12 nm in the NIR, in combination with a low polarization sensitivity and a high radiometric accuracy. The spatial sampling distance varies across the geographic coverage area and takes a value of 8 × 8 km² at a reference location at 45°N.

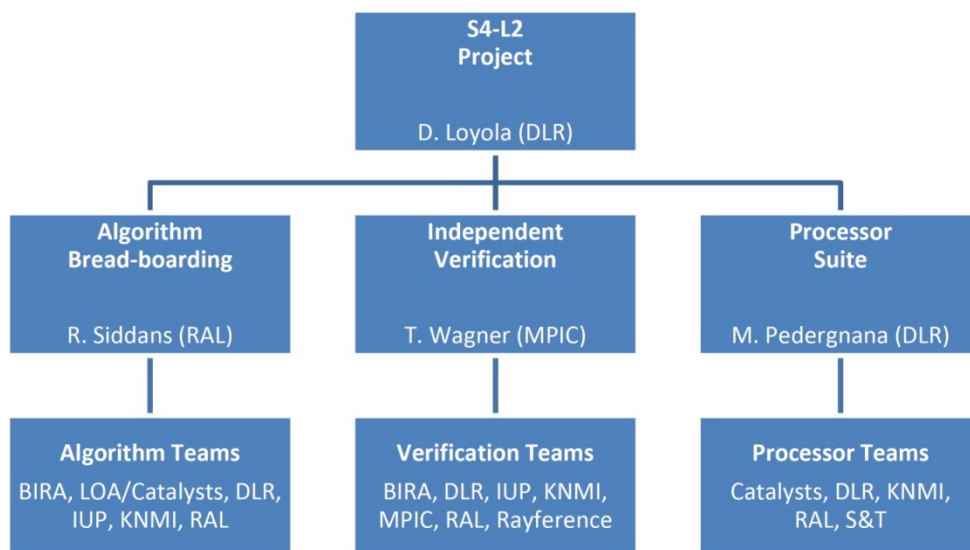


Fig. 2-8: Sentinel-4 Level-2 Project Organization.

The ESA level 2 project

The kick-off of the ESA S4 level 2 (L2) project took place in June 2015; the project will include the commissioning phase of the first MTG-S satellite with a foreseen launch date around 2020. Overall project coordination has been assigned to DLR (Fig. 2-8). RAL (UK) coordinates the algorithm bread-boarding activities performed by the algorithm teams of BIRA (BE), LOA (F) / Catalysts (A), DLR, IUP-UB (D), and KNMI (NL). The independent verification work is coordinated by MPIC (D) and covers the work of the verification teams of BIRA, DLR, IUP-UB, KNMI, RAL, Rayference (BE), and S&T (NO). Finally DLR coordinates the processor suite activities of the processor teams of Catalysts, DLR, KNMI, RAL, and S&T.

The objective of the S4 L2 project is to develop the Sentinel-4 level 2 bread-boarding algorithms, independent verification algorithms, prototype processors and ultimately the operational S4 L2 processors to be integrated into the MTG L2 Processing Facility (MTG L2PF) at EUMETSAT. Table 2-2 lists the products being developed under the L2 project with their corresponding threshold and goal accuracies.

Product	Threshold	Goal	Scenario
O₃ total column	4%	3%	SZA < 60°, VZA < 60° all clouds
Tropospheric O₃	40%	25%	SZA < 60°, VZA < 60° CF < 20%
Tropospheric NO₂	troposphere 50 %	troposphere 1.5*10 ¹⁵ molec/cm ² or 30%	SZA < 60°, VZA < 60° CF < 20%
SO₂	total column 100%	total column 1.0*10 ¹⁶ molec/cm ² or 80 %	SZA < 60°, VZA < 60° CF < 20% Pollution
HCHO	total column 100%	total column 1.5*10 ¹⁶ molec/cm ² or 50%	SZA < 60°, VZA < 60° all clouds
CHOCHO	n/a	total column 7.0*10 ¹⁴ molec/cm ² or 50%	SZA < 60°, VZA < 60° CF < 20% column > 5.0*10 ¹⁴ molec/cm ²
Aerosol layer height	1 km	n/a	SZA < 60°, VZA < 60° AOD > 0.3, ALH > 1.5 km
Aerosol Index	0.5	0.3	SZA < 60°, VZA < 60° cloud-free
AOD total column	0.05	n/a	cloud-free
Cloud properties	n/a	n/a	n/a
Surface	first BRDF parameter 0.01	n/a	SZA < 60°, VZA < 60° cloud-free, homogeneous

Table 2-2: Sentinel-4 level 2 products with target/goal performances

The first project review (PCR) was successfully finished in December 2015. The work in 2016 towards the Preliminary Design Review (PDR) will mainly focus on development of retrieval algorithms, generation of test data, and consolidation of the engineering interphases for the processors.

The EUMETSAT MTG L2PF project

The operational processing of Sentinel-4 and -5 level 1 and level 2 products will be performed at EUMETSAT. Thales (F) is coordinating the MTG L2PF project for developing the ground-segment components needed for the generation of the L2 products from all MTG sensors.

The S4 L2 processors, being developed as part of the ESA project, will be integrated into the L2PF with DLR providing the scientific/technical support for S4/UVN.

2.4 The Sentinel-5 Precursor Level 2 Project

D. Loyola, P. Hedelt, W. Zimmer, and S5P-Team

The Sentinel-5 Precursor (S5P), Sentinel-4 (S4) and Sentinel-5 (S5) missions are dedicated to monitoring the composition of the atmosphere for the operational Copernicus Atmosphere Services including the monitoring of air quality, stratospheric ozone, solar radiation and climate monitoring. S5P will be a dedicated satellite operated by ESA whereas both S4 and S5 missions will be carried on meteorological satellites operated by EUMETSAT.

The TROPospheric Monitoring Instrument (TROPOMI) is the instrument on board of S5P. It is conceived as a partnership between ESA and Dutch Space, KNMI, SRON and TNO, on behalf of NSO. TROPOMI is a space-borne nadir viewing spectrometer with bands in the ultraviolet and visible (270 to 495 nm), the near infrared (675 to 775 nm) and the shortwave infrared (2305 to 2385 nm). TROPOMI combines daily global coverage with a high spatial resolution of $3.5 \times 7 \text{ km}^2$ in order to focus on the troposphere where concentrations of trace gas and aerosol species rapidly change.

Operational processor UPAS

The UPAS processor for S5P became more mature in the course of developments during the last years. There was a successful delivery for the UPAS version 0.9 to ESA in November 2015 with the following features:

- **Big Data:** S5P will provide more than 21 million single measurements per day which is around a factor 100 more data than GOME-2. The architecture of UPAS and the retrieval algorithms are optimized for handling this huge amount of data. The system uses multi-threading capabilities at different levels, a usable scalability was attested which is important for an effective use of the multi-core and memory resources available.
- **Reliability:** For operational software that should work standalone in a 24/7 environment, reliability and stability are of course one of the most important requirements. The UPAS processors passed all acceptance tests without a single failure.
- **Stable Interfaces:** At this late stage, changes in interfaces become more expensive with each release. Therefore, it is vital to foresee and implement changes as soon as possible. As a final optimization step, the level 1b team implemented a new binning scheme, leading to a substantial level 1b product change. Although tight on time due to the unforeseen nature of the change, UPAS 0.9 included the necessary changes at delivery.
- **Feature Complete:** The features for the S5P operational algorithms had to be implemented, tested and declared fully functional. This includes the NRT and offline variant of the Cloud, O_3 , SO_2 and HCHO product, as well as the O_3 tropospheric and background processor product.

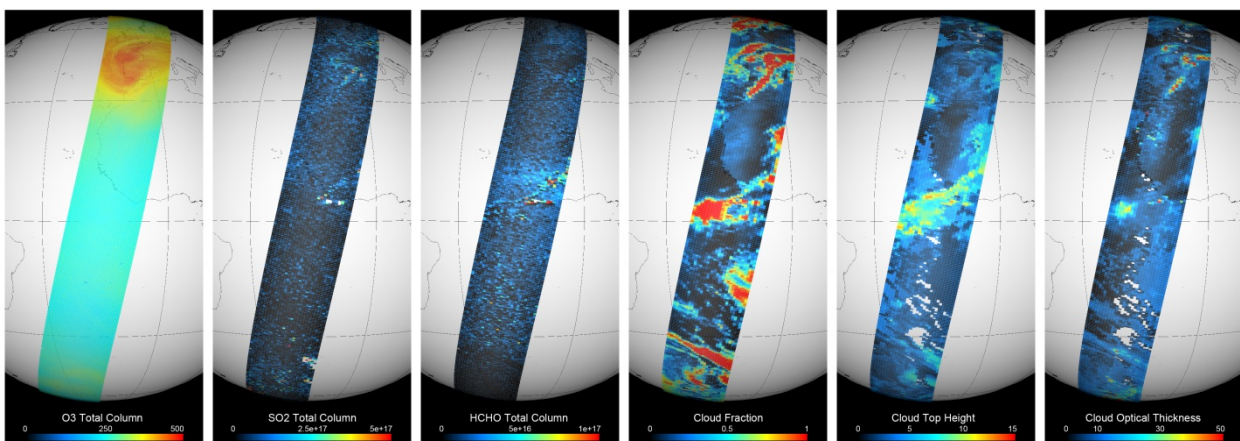


Fig. 2-9: Trace gas (O_3 , SO_2 , and HCHO) and cloud products (fraction, height, and optical thickness) generated with UPAS.

UPAS version 0.9 was used to estimate the need for computing resources in the operational Payload Data Ground Segment (PDGS). Therefore, especially the computational intensive algorithms, had to be included in a way that represents the final performance. This includes the DOAS fit for each product,

and the radiative transfer LIDORT modules, especially the direct fitting for the O_3 offline product (GODFIT algorithm). The performance evaluation tests run by PDGS showed that the UPAS performance is in line with the performance predicted in the Software System Requirements document.

UPAS 0.9 was successfully reviewed, only a minor update was needed in order to include UPAS in the PDGS version prepared for the ground segment acceptance review. This is the most important review prior to the satellite launch. Fig. 2-9 shows examples of products generated with UPAS 0.9 taking as input GOME-2 data reformatted to be compliant with the S5P L1b product format.

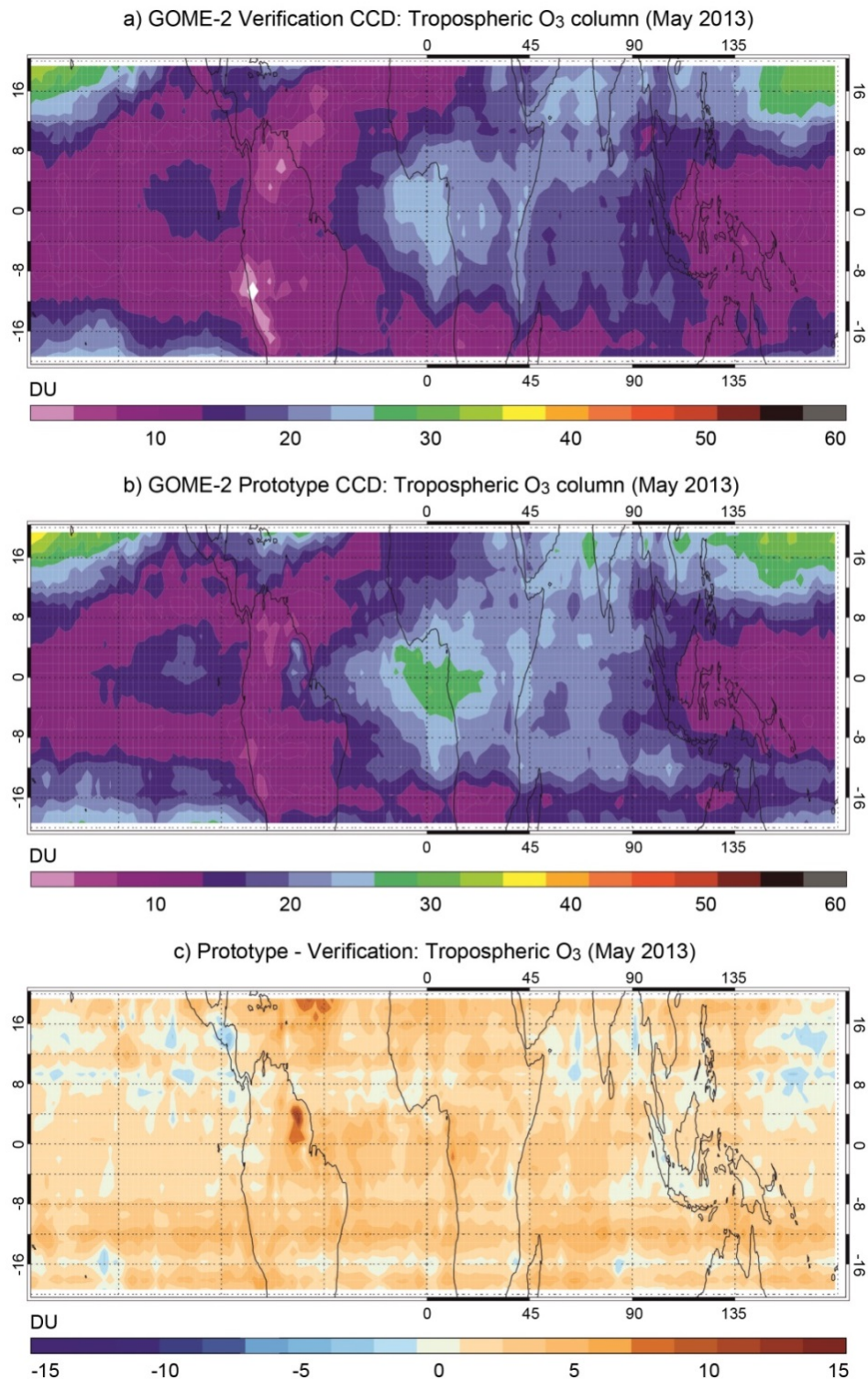


Fig. 2-10: Tropical tropospheric ozone column derived with the convective cloud differential technique for May 2013 with the verification algorithm (a), the operational algorithm (b), and the absolute differences between the two algorithms (c).

Independent verification

A novel component of the S5P L2 project is the verification of the operational algorithms with independent retrieval algorithms. This exercise allowed finding and solving some problems in the operational and verification algorithms and giving us confidence that the S5P L2 operational products will represent the state-of-science in the UVNS retrieval.

The verification activities are coordinated by the University of Bremen (IUP-IFE) with DLR participating as developer of operational algorithms and as provider of independent retrieval algorithms. Fig. 2-10 shows the results of the operational (DLR) and of the verification (IUP-IFE) Tropical Tropospheric Columns of Ozone algorithm compared with each other and with collocated tropospheric ozone columns below 200 hPa derived from the Southern Hemisphere ADditional OZonesondes (SHADOZ) network. The agreement between both columns is very good ($0.9 < \text{correlation coefficient } R < 0.99$, RMS between 4 and 9 DU and the biases less than 2 DU in most of the cases). Comparison with ozone sondes showed that the operational algorithm provided a slightly better correlation.

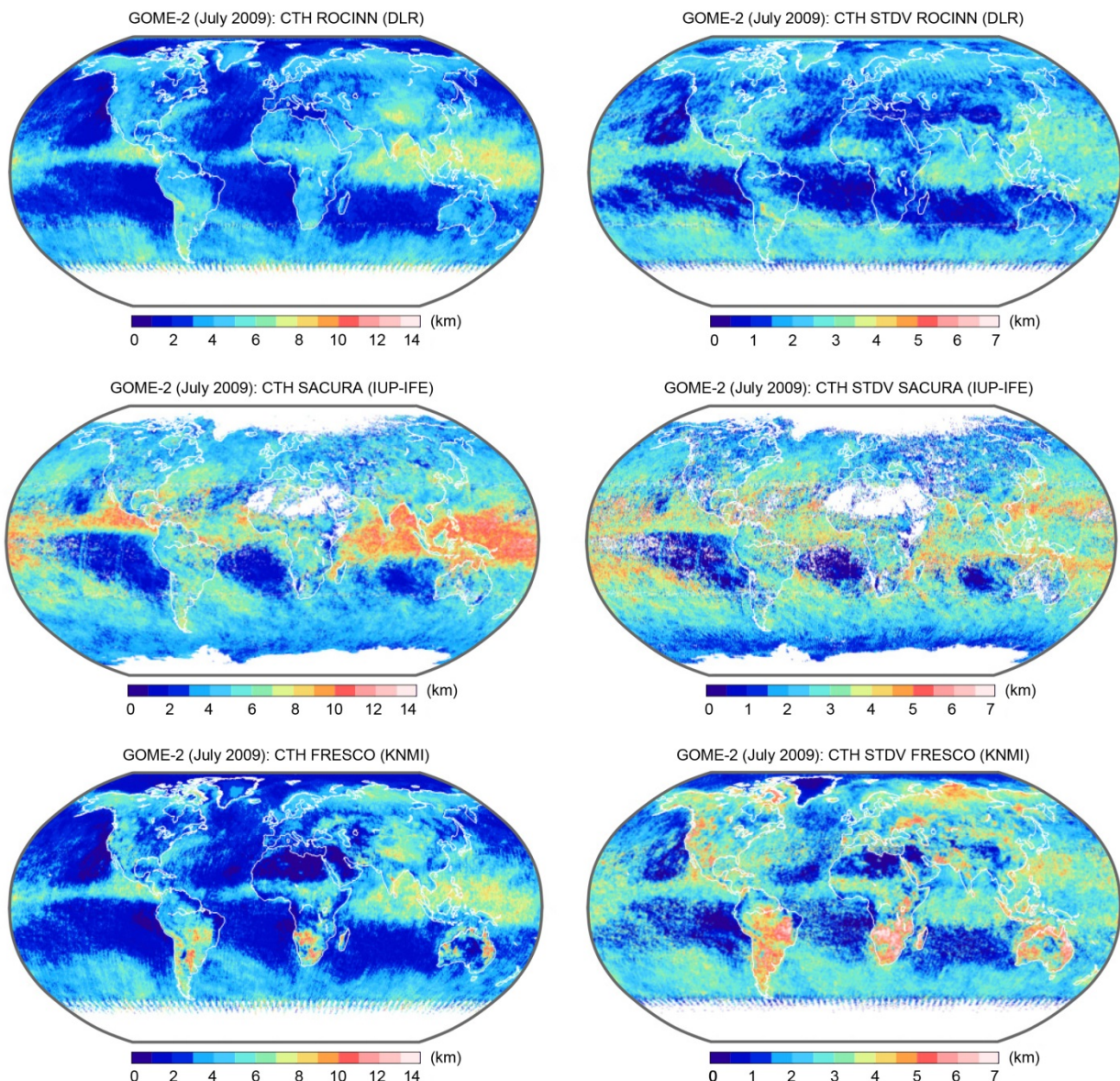


Fig. 2-11: Average (left column) and standard deviation (right column) for cloud height from GOME-2 measurements for July 2009 derived with the operational algorithm ROCINN (DLR, top row), and the verification algorithms SACURA (IUP-IFE, middle row) and FRESCO (KNMI, bottom row).

For some products it was necessary to first align the radiative transfer (RT) models used by the operational and verification algorithms before comparing them. In the case of clouds, it has been

shown that the RT models LIDORT and SCIATRAN can agree up to a systematic relative residual of less than 0.5% in the strong absorption of oxygen. The treatment of clouds as scattering layers by the operational algorithm ROCINN (DLR) has provided more accurate cloud altitudes than the ones retrieved with the Lambertian model, as proved in the analysis of real and synthetic data sets together, delivering an average bias lower than ± 1 km for all case studies. ROCINN cloud heights are accurate also with respect to the underlying surface albedo and optical thickness, given a near-nadir observational geometry. Fig. 2-11 illustrates the verification results using GOME-2 data with the operational algorithm ROCINN (DLR), and the verification algorithms SACURA (IUP) and FRESCO (KNMI).

S5P Launch and beyond

Both the TROPOMI instrument and the S5P satellite are flight-ready. The S5P launch is currently foreseen for October 2016. The S5P work at DLR-IMF will be continued in 2016 with national funding and the ESA/ESTEC S5P L2 project. Additionally it is expected that the ESA/ESRIN S5P Mission Performance Center (MPC) project will be started in Q2/2016. This project will cover the complete S5P mission of at least seven years.

2.5 MERLIN Level 0-1 Data Processing

G. Lichtenberg, M. Hamidouche, B. Aberle

Methane (CH₄) is one of the strongest greenhouse gases and contributes significantly to global warming. For identifying its sources and sinks and the related processes, accurate measurements of the atmospheric CH₄ content with high spatial resolution are mandatory. The German-French MERLIN mission will achieve this goal. It will be the first Integrated Path Differential Absorption (IPDA) Lidar mission in space. CH₄ will be measured with high accuracy by sending two laser pulses to the ground, one with a wavelength centered in the CH₄ absorption at 1645.552 nm (λ_{on}) and one directly outside the absorption at 1645.846 nm (λ_{off}). The ground spot of the MERLIN laser will be about 100 m wide. In order to obtain sufficient signal-to-noise several shots have to be co-added. Current baseline is to co-add the signal for a footprint of 50 km, i.e. to co-add 50 shots. From the comparison of the backscattered intensity of both lines the differential absorption optical depth (DAOD) of CH₄ can be determined which finally permits to derive the CH₄ content of the atmosphere.

The share of MERLIN responsibilities tasks Germany with the instrument development, the monitoring of its in-orbit performance and the level 0-1 processing. Our French partners provide the satellite platform and its operations and the ground segment for the operational processing, including the level 1-2 processing. The algorithms for level 0-1 and 1-2 processing will be defined by both parties in collaborative effort.

High level architecture and embedding in ground-segment

The level 0-1 processing is split in three major parts (Fig. 2-12). They include

- **Level 0 Decommutation**
The level 0a data contain raw data packets which are transferred from the platform together with auxiliary information about the type of the data packages. In order to make the data usable for subsequent algorithms, the data have to be decommutated, i.e. the byte stream has to be converted to instrument parameters and measurement results, associated with a measurement time and written to a standard format, e.g. netCDF. This level 0b (L0b) product no longer contains a sequence of data packages which consist of byte sequences, but individual variables and instruments parameters with proper attributes and time stamps.
- **Adding Positional Data**
For the calculation of the geolocation, the platform attitude, platform position and an orbit propagator to calculate the geolocation at any point in the orbit are required. CNES will take the timing information and the positional data from the platform, the decommutated timing information for each shot from the L0b product and will derive the satellite position and attitude per shot. This information will later be used in the level 0-1 processor to determine the exact geolocation of each measurement.

- **Level 0b-1 Processing**

This is the main processing step. It converts intensity as a function of time from the pair of pulses (λ_{on} and λ_{off}) into DAOD. The processor design is currently derived from the Algorithm Theoretical Baseline Document (ATBD) which mathematically describes all the algorithms needed to go from instrument measurements to CH₄ concentrations.

The level 0-1 processor will be developed at DLR-IMF in Oberpfaffenhofen and will then - after thorough testing - be embedded into the CNES operational ground segment at Toulouse (Fig. 2-13). CNES uses the so-called Phoebus system to manage all processes in the ground segment. This system is capable to

- start and stop processes (pre, main, post)
- define the chain of processes to be executed
- allocate needed resources to the processor
- transfer messages to/from processes to outside world

The level 0-1 processor will be started by Phoebus and picks up data from the allocated working directory. Important messages or signals from the processor will be relayed by the PIK library, i.e. the sole communication interface between Phoebus and the processor, to the Phoebus main control which sends them to the operator or to a logging service. Important messages from the ground segment to the processor will be transferred by Phoebus via PIK. The level 1 products generated by the processor will be picked up by Phoebus and send to the archive, where they are accessible to the level 1-2 processor and users.

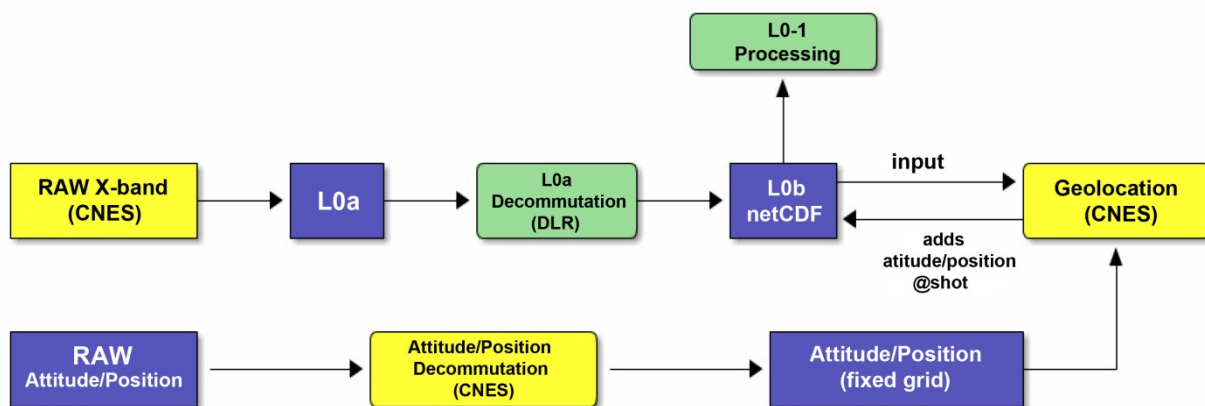


Fig. 2-12: High level description of the Level 0-1 processing chain.

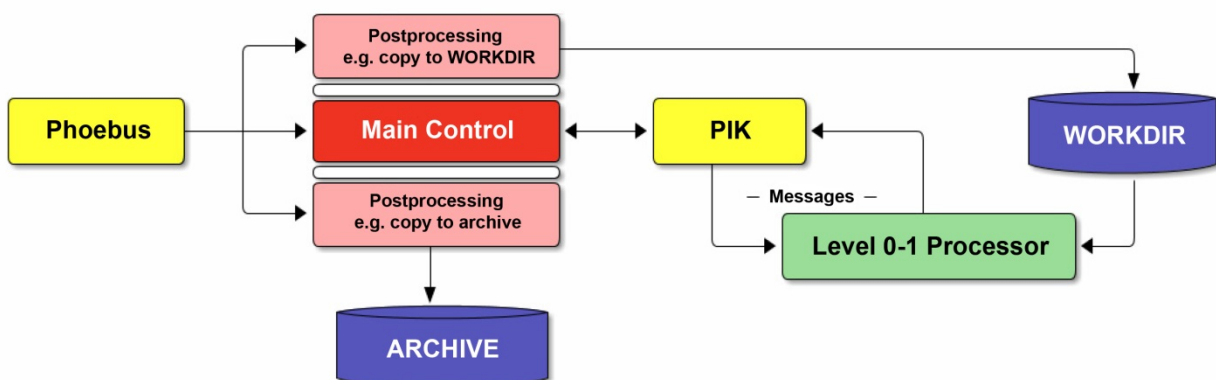


Fig. 2-13: Embedding of the Level 0-1 processor in the CNES ground segment.

The generic level 0-1 processing framework GCAPS, which was already used for the operational SCIAMACHY level 0-1 processor will also be employed for the MERLIN level 0-1 processor. The next steps in processor development will be the development of the detailed design based on the ATBD and subsequently a first implementation for initial performance testing.

3. Atmospheric Remote Sensing – Methods

3.1 Operational Atmospheric Composition SAF Trace Gas Column Products from GOME-2

P. Valks, N. Hao, P. Hedelt, M. Begoin, M. Grossi, S. Liu, K.-P. Heue, R. Lutz, S. Gimeno García, D. Loyola

The operational GOME-2 trace gas column and cloud products from MetOp-A and MetOp-B are provided by IMF-ATP in the framework of EUMETSAT's Satellite Application Facility on Atmospheric Composition Monitoring (AC SAF, formerly Ozone Monitoring SAF – O3M SAF) (Hassinen *et al.* 2015). The current GOME-2 trace gas products of the AC SAF include total ozone, total and tropospheric NO₂, SO₂, BrO, formaldehyde (HCHO) and water vapor. The AC SAF trace gas column products are generated operationally at DLR using the GOME Data Processor (GDP). In 2015, the new GDP version 4.8 used for the reprocessing of the GOME-2 trace gas columns has been reviewed by EUMETSAT (see below) and the tropical tropospheric ozone product has become operational (see chapter 3-5). The GOME-2 trace gas column data from MetOp-A and -B are used in the near-realtime (NRT) system of the Copernicus Atmospheric Monitoring Service (CAMS). During the second Continuous Development and Operation Phase (CDOP-2) of the AC SAF (2012-2017), the focus is on the development of new and better products, on new dissemination methods and on improved user services. New GOME-2 trace gas column products, developed in the framework of CDOP-2 include total OCIO, tropospheric ozone, BrO and glyoxal, as well as NO₂ and water vapor climate products.

The new processor version 4.8 for GOME-2 on MetOp-A and -B

In November 2015, an Operational Readiness Review (ORR) of the new GDP version 4.8 for the retrieval of the GOME-2 trace gas column products from MetOp-A and -B was carried out successfully. The GDP 4.8 is used for the operational NRT and off-line processing, as well as for the reprocessing of the GOME-2 trace gas column products for the complete MetOp-A and -B missions. The GDP 4.8 includes improvements in the GOME-2 total ozone, NO₂, SO₂ and HCHO column algorithms (Valks *et al.* 2015). The algorithm developments for NO₂ and SO₂ are described in chapters 3-3 and 4-2. Important improvements were also made in the retrieval of the GOME-2 cloud properties using the OCRA & ROCINN algorithms. The OCRA algorithm has been enhanced by the implementation of correction schemes for instrumental degradation of the PMD data as well as for scan angle dependencies, and an improved sunglint detection has been implemented. New corrections for the GOME-2 instrument degradation in the O₂ A-band and a new inversion scheme (Tikhonov regularization) have been implemented in the ROCINN algorithm used for the retrieval of the cloud pressure and albedo (see also chapter 3-7).

All the operational trace gas column products based on the GDP 4.8 have been validated with ground-based measurements for the complete GOME-2 mission from 2007 to 2015. The validation revealed that the reprocessed GOME-2 trace gas column data from MetOp-A and -B are within the targeted accuracy requirements and that their physical consistency has overall improved. The comparison of the GOME-2 total ozone columns with ground-based Dobson and Brewer measurements shows that the GDP 4.8 improves the retrieved ozone columns from MetOp-B, and largely removed the scan angle dependency issues in the GOME-2 ozone columns. Fig 3-1 illustrates the total ozone column from GOME-2 for 2 and 4 October 2015 over the Antarctic, as retrieved with the GDP 4.8. On 2 October 2015, the ozone hole expanded to its peak of 28.2×10^6 km², as a result of the unusually cold temperature and weak dynamics in the Antarctic stratosphere. Throughout October, the ozone hole remained large and set many daily records.

The validation of the GOME-2 HCHO columns with ground-based MAX-DOAS observations in Beijing, Burundi and Brussels are very encouraging since a good overall agreement is obtained between GOME-2A and -B and the MAX-DOAS measurements at the three stations. The improved GOME-2 HCHO columns from the GDP 4.8 have been used to estimate biogenic volatile organic compounds (BVOC) emission fluxes in the Changbai Mountain temperate forest (Bai *et al.*, 2015). As HCHO is considered as the main oxidation product of isoprene and monoterpenes, it is necessary to investigate the link between HCHO and BVOC emissions. Good relationships were found between BVOC emission fluxes and GOME-2 HCHO VCDs in the Changbai Mountain temperate forest, which means that the satellite data provides a reliable estimate of BVOCs emission.

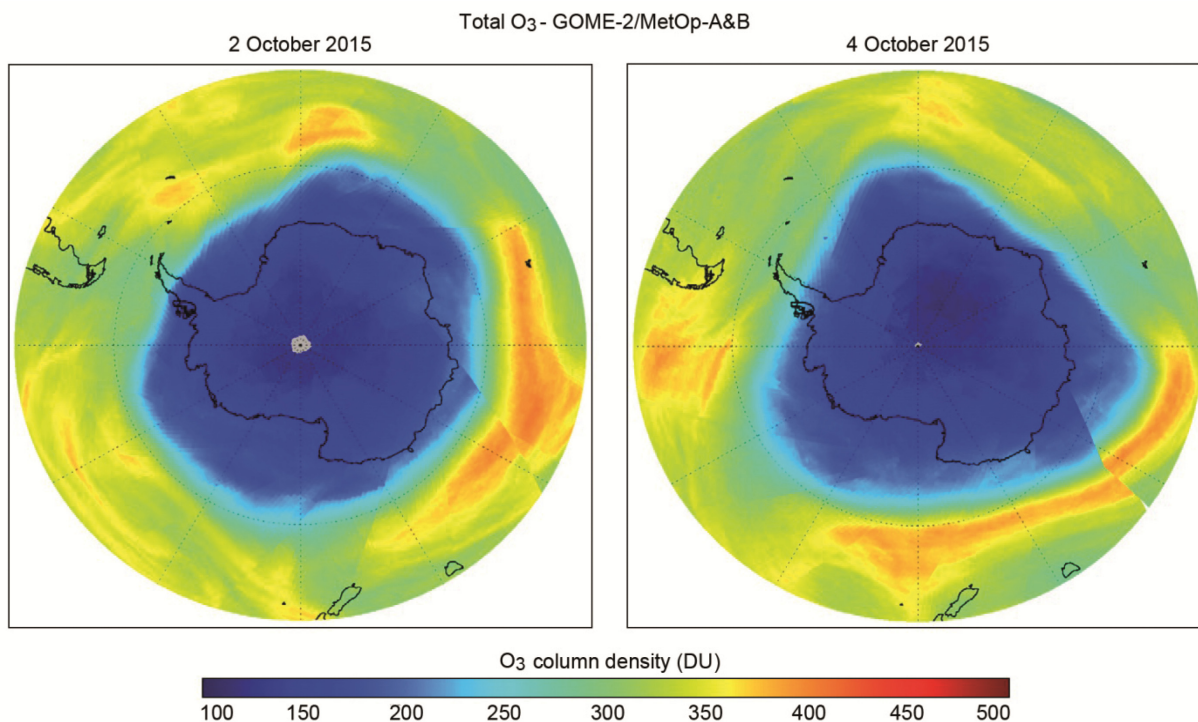


Fig. 3-1: Total ozone maps for 2 and 4 October 2015 based on data from GOME-2A and GOME-2B.

References

Bai, J., Duhl, T., Hao, N.: Biogenic volatile compound emissions from a temperate forest, China: model simulation. *Journal of Atmospheric Chemistry* (10874), 1-31, doi: 10.1007/s10874-015-9315-3, 2015.

Hassinen, S., Balis, D., Bauer, H., Begoin, M., Delcloo, A., Eleftheratos, K., Gimeno García, S., Granville, J., Grossi, M., Hao, N., Hedelt, P., Hendrick, F., Hess, M., Heue, K.-P., Hovila, J., Jönch-Sørensen, H., Kalakoski, N., Kiemle, S., Kins, L., Koukouli, M.E., Kujanpää, J., Lambert, J.-C., Lerot, C., Loyola, D., Määttä, A., Pedernana, M., Pinardi, G., Romahn, F., van Roozendaal, M., Lutz, R., De Smedt, I., Stammes, P., Steinbrecht, W., Tamminen, J., Theys, N., Tilstra, L.G., Tuinder, O.N.E., Valks, P., Zerefos, C., Zimmer, W., Zyrichidou, I.: Overview of the O3M SAF GOME-2 operational atmospheric composition and UV radiation data products and data availability. *Atmospheric Measurement Techniques Discussion*, 8, 6993–7056, 2015.

Valks, P., Loyola, D., Hao, N., Hedelt, P., Slijkhuis, S., Grossi, M., Begoin, M., Gimeno García, S., Lutz, R.: Algorithm Theoretical Basis Document for GOME-2 Total Column Products of Ozone, Minor Trace Gases and Cloud Properties (GDP 4.8 for O3M-SAF OTO and NTO). DLR/GOME-2/ATBD/01, Iss./Rev.: 3/A, March, 2015.

3.2 Atmospheric Methane with SCIAMACHY: First DLR Operational Level 2 Data

M. Hamidouche, G. Lichtenberg, S. Gimeno Garcia, M. Meringer, F. Schreier

SCIAMACHY on ENVISAT has probed a large number of atmospheric trace gas species. Amongst these is methane (CH_4), which is particularly interesting as it is one of the most abundant greenhouse gases in the Earth atmosphere and it contributes significantly to climate change. This makes methane a key gas to probe. Both its geographical distribution and temporal variation are parameters of paramount interest.

Level 1b-2 operational processor: Methane

The Level 1b-2 operational processor uses level 1b products to generate the trace gases columns and the clouds parameters as part of the level 2 products. Methane has been included in the chain of the DLR operational processor (see also chapter 2-1 of the current report). The retrieval uses DLR's BIRRA (Beer InfraRed Retrieval Algorithm) algorithm yielding nadir CH_4 concentrations from SCIAMACHY's SWIR channel 6 at $1.6 \mu\text{m}$. Integration of BIRRA required expanding the operational SCIAMACHY level 1b-2 processor. Ultimately, methane retrieval is part of the latest version of the processor (V6.0).

The level 2 product provides the vertical column density (VCD), given in molecules/ cm^2 , as illustrated in Fig. 3-2. Furthermore, to derive the dry air mixing vertical ratio XCH_4 , corrections for cloud effects as well as transmission changes have to be implemented. This occurs by normalizing the gas by a relatively more stable, homogeneous and yet simultaneously measured gas (Gimeno Garcia et al. 2011). The selected trace gas is carbon dioxide (CO_2) since it can be retrieved from the same channel as CH_4 , channel 6. In addition, its spectral traces reside close to the CH_4 band. CO_2 column values are computed by the operational processor as part of channel 6 data processing. Finally, both XCH_4 and the CH_4 product are included in the processor Level 2 data.

Tests and comparison: Verification and validation

Our work also comprises the verification and validation of methane data from the SCIAMACHY operational processor. This validation study uses level 2 CH_4 data of the year 2004. They have been generated from level 1b data V8. The tests are based on two separate comparisons: Firstly with existing level 2 SCIAMACHY methane data produced by IUP-IFE, University of Bremen and SRON institute and secondly with methane retrieved from ground-based measurements such as TCCON (Total Carbon Column Observing Network) and ESRL (Earth System Research Laboratory) Global Monitoring

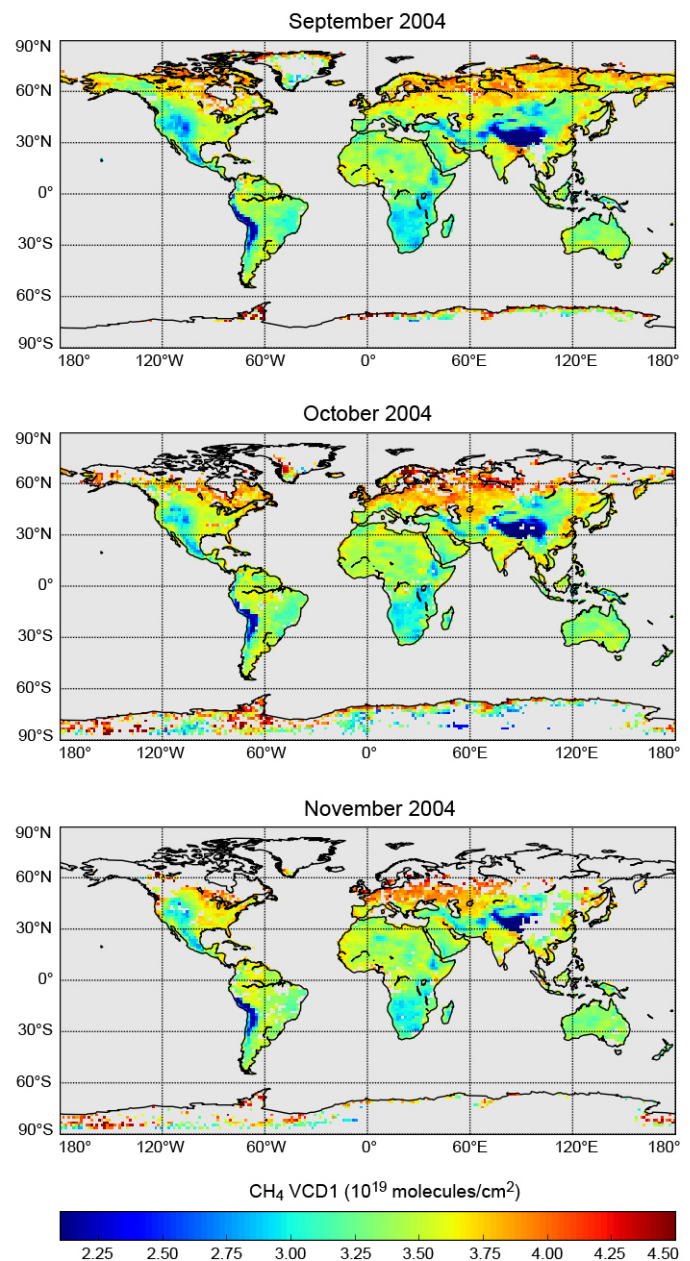


Fig. 3-2: Example of monthly averaged maps with a spatial resolution of $1.5^\circ \times 1.5^\circ$ of the Methane VCD distribution over land from September to November 2004. The product is derived with the SCIAMACHY L1b-2 operational processor (V6).

Division (GMD).

The core of this first comparison is checking the stability within error bars of the monthly values and the consistency of the global gas distribution between the different methane products. Fig. 3-2 shows some of the results for three successive months in 2004. The values remain consistent overtime. They also fall within the error bars of the existing SCIAMACHY values produced by IUP-IFE institute at the University of Bremen and those generated by SRON (see also Fig. 3-3).

Fig. 3-3 shows the monthly averaged XCH₄ ESRL GMD data in a North African site in the Sahara compared to SCIAMACHY values in the same geographical location (over a 4° × 4° region around the ESRL site). SCIAMACHY data from both the SRON and DLR operational processors are shown for comparison and consistency. Our data are on average uniform and agree with up to 3% with ESRL data and up to 4% with SRON's.

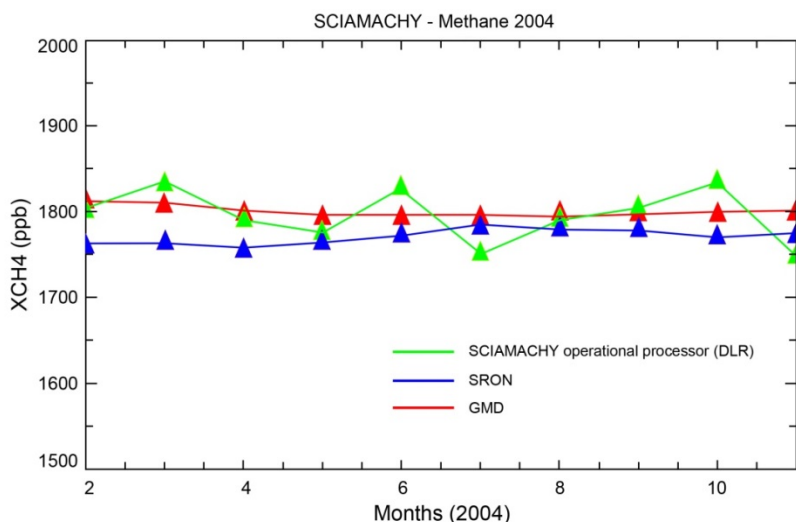


Fig. 3-3: XCH₄ data comparison between the ESRL GMD at the Assekrem site in the Sahara in North Africa (shown in red), SRON SCIAMACHY L2 data (blue), and data from our operational processor (green). The data are monthly averaged from February until November 2004.

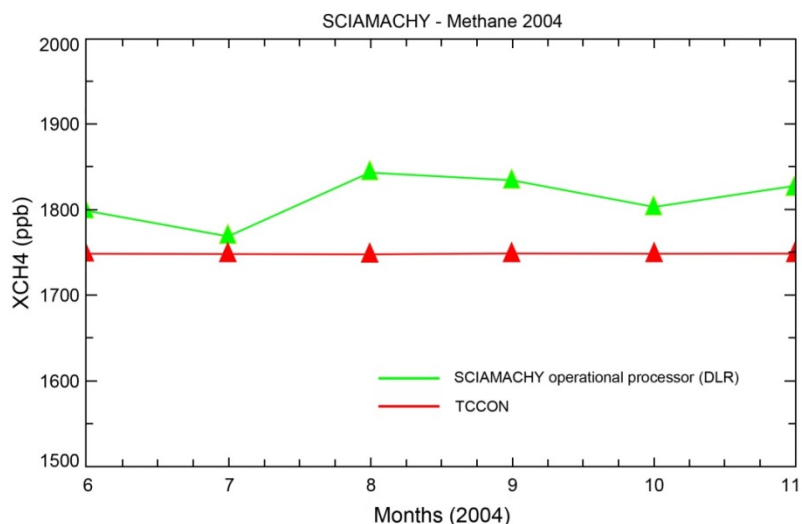


Fig. 3-4: XCH₄ data comparison between our data and TCCON's site at Park Falls in North America. The SCIAMACHY data are measured around the geographical location of the site. The data are monthly averaged from June until November 2004.

Although not many available CH₄ TCCON data in 2004 exist, a further comparison is run against this set data. The Park Falls TCCON site, located in North America, measured only six months of data between June and November 2004. Fig. 3-4 illustrates the corresponding XCH₄ monthly averaged values compared against our data over a 4° × 4° region around the Park Fall site. Overall the values are consistent and deviate only slightly from each other by up to 6%.

The first DLR's operational processor generated CH₄ data show an overall agreement with ground based measurements. The deviation between SCIAMACHY data and ground based corresponding values are not significant and lie within a few percent only from each other. Nevertheless, it is hard to settle with these results as the comparison was run for a period of less than a year only. In order to make solid statistical comparisons, we plan to pursue the tests for several additional months and, when available, with further geographical sites.

References

Gimeno García, S., Schreier, F., Lichtenberg, G., Slijkhuis, S.: Near infrared nadir retrieval of vertical column densities: methodology and application to SCIAMACHY. *Atmospheric Measurement Techniques*, 4/12, 2633-2657, 2011.

3.3 Improvement of Total and Tropospheric NO₂ Column Retrieval for GOME-2

S. Liu, P. Valks

Nitrogen dioxide (NO₂) plays a significant role in atmospheric chemistry. It is related to ozone destruction in the stratosphere, and is regarded as an important air pollutant and ozone precursor in the troposphere. Started in 2015, this PhD-project addresses the development and refinement of novel scientific algorithms for the retrieval of total and tropospheric NO₂ columns to fully exploit the capabilities of the Global Ozone Monitoring Experiment (GOME-2) satellite instrument aboard the MetOp platforms and the forthcoming European satellite mission Sentinel-5 Precursor.

The differential optical absorption spectroscopy (DOAS) method is applied to determine the NO₂ slant columns from GOME-2 in the visible wavelength region (425-450 nm). Initial total NO₂ vertical columns are calculated by an air mass factor conversion using the LIDORT model and a stratospheric NO₂ climatology. To estimate the stratospheric component, a spatial filtering algorithm is applied. Tropospheric air mass factors are computed using monthly averaged NO₂ profiles from the MOZART-2 chemistry transport model, and the tropospheric NO₂ columns can be determined (*Valks et al. 2011*).

In the past year, our research focused on two parts of the NO₂ retrieval algorithm. In the DOAS fit, a larger 425-497 nm wavelength fitting window is used to determine the NO₂ slant column density. Theoretically the retrieval quality will be improved, since more spectral points are included in the fit. However, spectral interference with other absorbing trace gases also increases. Therefore, additional cross-sections for liquid water and desert are included in the DOAS fit to reduce systematic errors, as well as Eta and Zeta calibration functions (*Richter et al. 2011*). The use of the larger 425-497 nm fitting window results in an increase in the retrieved NO₂ columns from GOME-2, as illustrated in Fig. 3-5.

Secondly, a new surface Lambertian equivalent reflectance (LER) climatology based on GOME-2 observations for 2007-2013 (*Tilstra et al. 2014*) is used for the calculation of the Air Mass Factor (AMF). In contrast to the currently used surface LER climatology based on GOME/ERS-2 data, the new surface LER climatology is consistent with the GOME-2 NO₂ observations (i.e. illumination conditions and instrument characteristics). The GOME-2 surface albedo climatology takes advantage of newer observations, smaller footprint size, and an improved LER algorithm. The effect of the new surface albedo climatology on tropospheric NO₂ column retrieval is shown for January 2008 in Fig. 3-6. Differences between the two surface LER datasets, such as the snow and sea ice coverage, pixel-to-pixel variability and instrumental performance, have a large effect on the retrieved tropospheric NO₂ column.

Future work will concentrate on the improvement of the Stratosphere-Troposphere Separation (STS) algorithm, since the uncertainty from stratospheric column estimation is one of the main sources of error in the calculation of the tropospheric NO₂ column. Intercomparisons of the GOME-2 NO₂ measurements from MetOp-A and B, and comparisons with other NO₂ satellite products shall be performed. Furthermore, the use of GOME-2 tropospheric NO₂ data for air quality applications will be illustrated for China and Europe, and time-series of tropospheric NO₂ are analyzed to investigate trends in air pollutants.

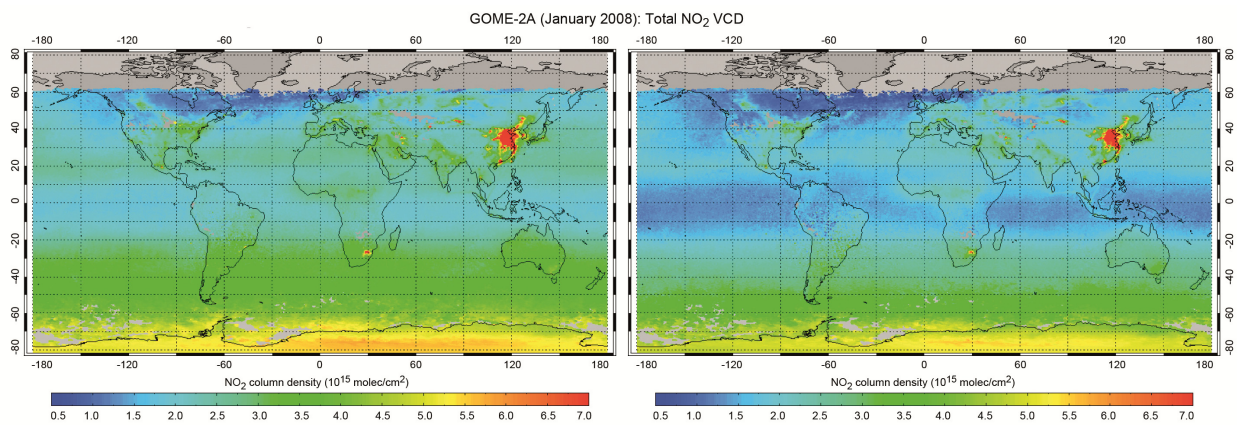


Fig. 3-5: Global total NO₂ column distribution in January 2008 as measured by GOME-2/MetOp-A using a large 425-497 nm wavelength fitting window (left) and the standard 425-450 nm wavelength fitting window (right).

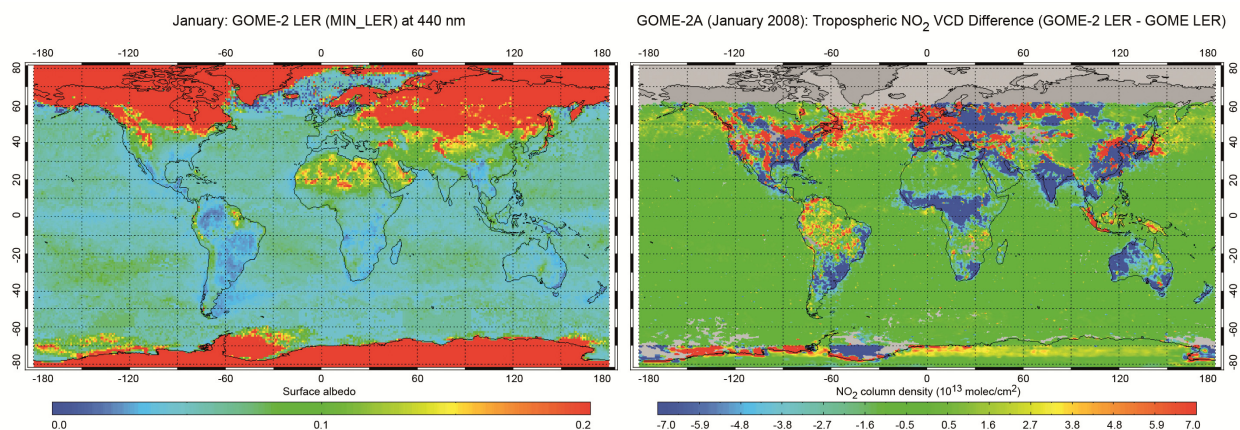


Fig. 3-6: Map of surface LER data for the month of January based on GOME-2 observations (Tilstra et al. 2014) (left). The right panel shows the difference between the tropospheric NO₂ columns in January 2008 retrieved using the new GOME-2 surface LER climatology and the old one based on GOME/ERS-2 data.

References

Richter, A., Begoin, M., Hilboll, A., Burrows, J.P.: An improved NO₂ retrieval for the GOME-2 satellite instrument. *Atmospheric Measurement Techniques*, 4, 1147-1159, 2011.

Valks, P., Pinardi, G., Richter, A., Lambert, J.-C., Hao, N., Loyola, D., Van Roozendaal, M., Emmadi, S.: Operational total and tropospheric NO₂ column retrieval for GOME-2. *Atmospheric Measurement Techniques*, 4, 1491-1514, 2011.

Tilstra, L.G., Tuinder, O.N.E., Stammes, P.: GOME-2 surface LER product - Algorithm Theoretical Basis Document. KNMI Report O3MSAF/KNMI/ATBD/003, Issue 1.6, November 13, 2014.

3.4 Validation of Carbon Monoxide Vertical Column Densities Retrieved from SCIAMACHY Infrared Nadir Observations

P. Hochstaffl (Innsbruck University and IMF-ATP), F. Schreier, S. Gimeno García, G. Lichtenberg

Carbon monoxide (CO) and methane (CH₄) are key species of the Earth's atmosphere. Accordingly, a large number of spaceborne sensors are observing these species in the microwave, thermal and near infrared (NIR). For the analysis of short wave infrared (SWIR) spectra measured by SCIAMACHY and similar instrument(s), the Beer InfraRed Retrieval Algorithm (BIRRA) had been developed in our department. BIRRA is a separable least squares fit of the measured radiance with respect to molecular column densities and auxiliary parameters (optional: surface albedo, baseline, slit function width, and wavenumber shift). BIRRA had been implemented in the operational SCIAMACHY L1 to 2 processor for the retrieval of CO and CH₄ from channel 8 and 6, respectively. For our validation study we required a higher degree of flexibility and therefore used the BIRRA prototype version instead.

Verification and validation are critical elements of any code development, and mandatory for the assessment of spaceborne remote sensing products. Here we report on intercomparisons of CO columns estimated from SCIAMACHY with coincident and co-located retrievals provided by ground-based Fourier transform infrared spectroscopy. More specifically, we have used data from several NDACC (Network for the Detection of Atmospheric Composition Change) and TCCON (Total Carbon Column Observing Network) stations. Like SCIAMACHY's channel 8 the TCCON instruments utilize the 2.3 μm-band of carbon monoxide, whereas NDACC observes the CO mid infrared absorption. Unfortunately, however, TCCON became operational only in the mid of the last decade, so validation data are rarely available for the early years of the ENVISAT mission providing "good" CO retrievals.

The results indicate the importance of appropriate sampling areas around the station, calibration of level 1 data, and post-processing of the BIRRA retrievals, especially filtering. Because of the weak CO signal in channel 8, column densities retrieved from individual spectra corresponding to a single ground pixel cannot be used "as is", i.e. the columns have to be averaged in space and time. Furthermore,

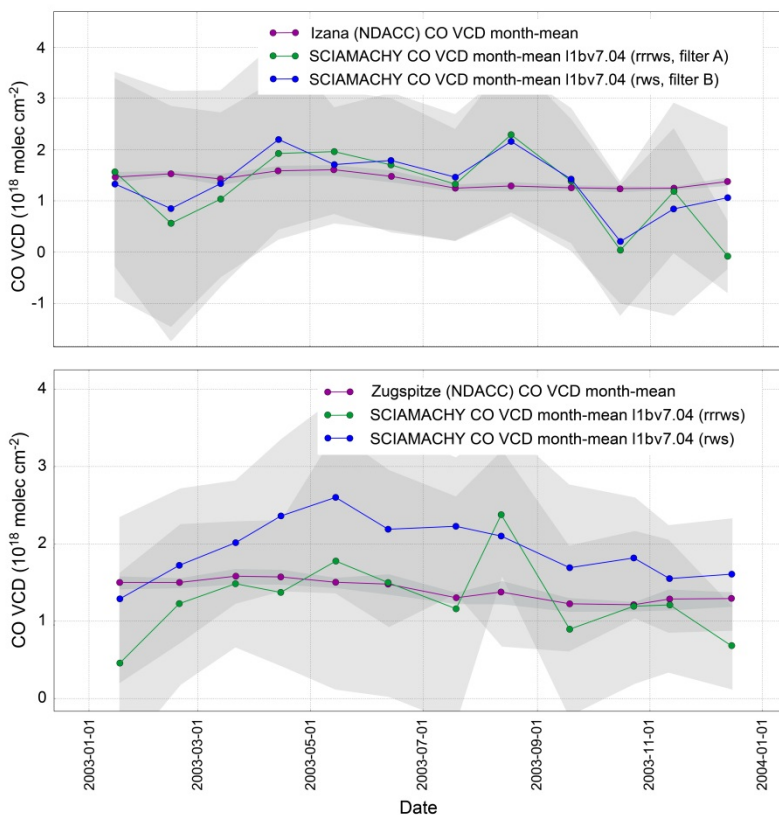


Fig. 3-7: Comparison of SCIAMACHY versus ground-based CO columns. Top Impact of different filters. Bottom: Impact of auxiliary fit parameters – reflectivity polynomial.

"suspicious" level 2 products, e.g. from fits with failed convergence, large error bars, or columns significantly deviating from some preselected confidence interval, have to be filtered out. Fig. 3-7 (top) compares CO columns derived from BIRRA and filtered with two different criteria with coincident CO columns above the NDACC Izana station. Among the auxiliary parameters fitted by BIRRA in addition to the molecular density scaling factors, the order of the reflectivity polynomial has a significant impact on the quality of the retrieval as demonstrated in Fig. 3-7 (bottom).

Ideally BIRRA columns should resemble the columns measured from the ground-based station both in magnitude and in its temporal behavior. Because of the large scatter/variability of the CO columns measured by SCIAMACHY, polynomial and sinusoidal fitting has been used to better visualize the trends. In Fig. 3-8 fits of the BIRRA columns and

the corresponding NDACC columns are compared for the Zugspitze and Jungfraujoch mountain stations. Finally, the BIRRA columns in the Toronto (Fig. 3-9 top), Izana, and Jungfraujoch area exhibit a large deviation from the corresponding ground-based measurement in August 2003, indicating an instrument anomaly. Despite some missing TCCON observations in 2007, the comparison in the bottom panel of Fig. 3-9 confirms consistent trends of both datasets.

The increased deviations of the spaceborne and ground-based columns in the later years of the mission clearly demonstrate the impact of SCIAMACHY's degrading channel 8 detector. Nevertheless, the CO columns derived from SCIAMACHY and NDACC/TCCON largely agree within the error bars.

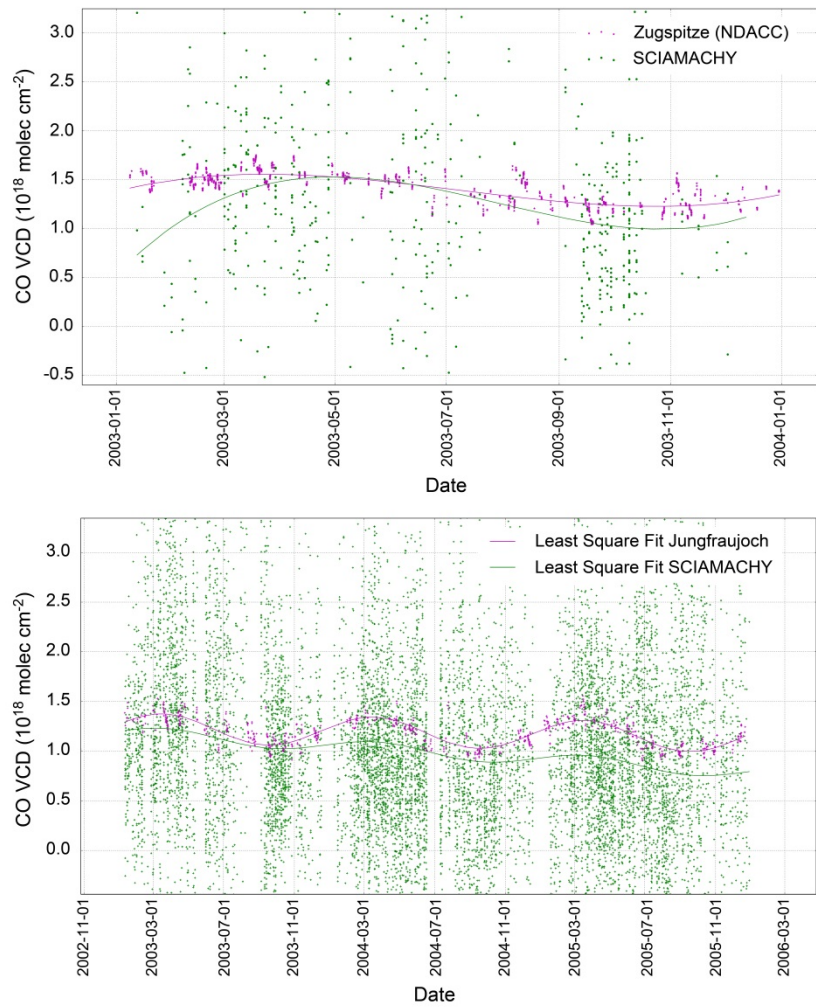


Fig. 3-8 (top): Polynomial fit of CO columns observed by SCIAMACHY and the NDACC Zugspitze station (top) and sinusoidal fit for NDACC Jungfraujoch station (bottom).

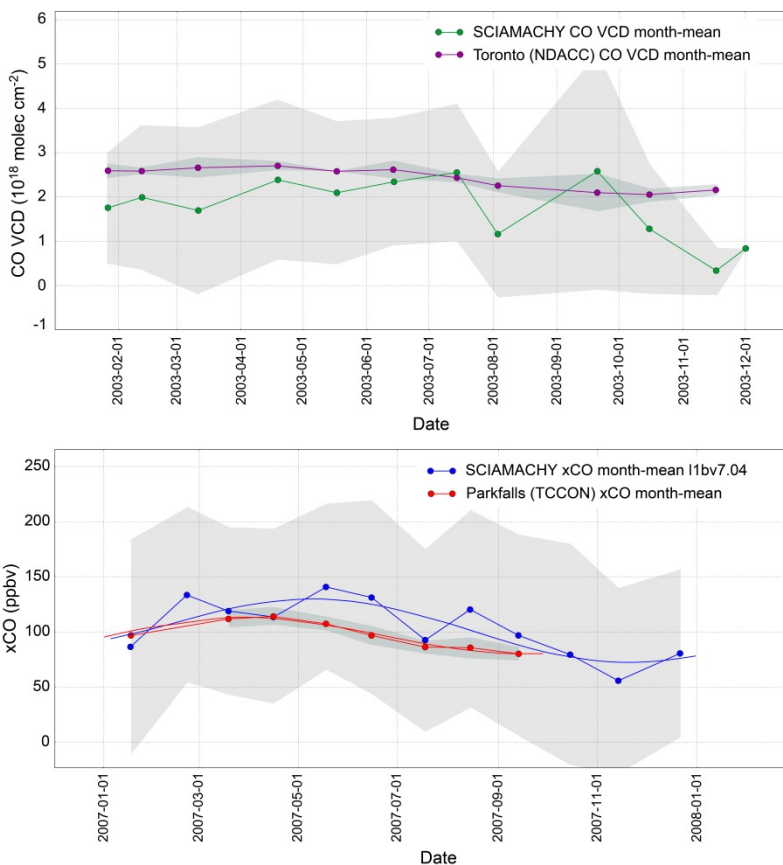


Fig. 3-9 (left): Comparison of monthly mean CO columns from SCIAMACHY versus Toronto NDACC station (top) and Park Falls TCCON station (bottom).

3.5 Long-term Time Series of Satellite Based Tropical Tropospheric Ozone Columns

K.-P. Heue, D. Loyola, P. Valks, M. Coldewey-Egbers

Within the ESA Ozone-CCI project the tropospheric column was retrieved based on the GODFIT level 2 product which was generated within the Ozone Climate Change Initiative (CCI) project. This product has a very high stability with respect to instrumental effects, and moreover, the complete dataset of the European satellite missions delivering ozone products, i.e. GOME, SCIAMACHY, OMI and GOME-2, were re-analyzed with this processor. Therefore this dataset offers a good basis to examine long time trends.

Tropospheric ozone retrieval

For the retrieval of the tropical tropospheric ozone columns (TTOC) the convective cloud differential (CCD) algorithm is used. The CCD method is based on the total ozone column data product (level 2) and the respective cloud product. The basic idea is to subtract an estimate of the stratospheric column from the total column to retrieve the tropospheric column. With the CCD method the stratospheric ozone column (SOC) is determined by the observed ozone column above high reaching clouds (*Valks et al. 2014*). Because clouds shield the ozone below their altitudes this approach is well suitable to estimate the SOC. Due to this shielding effect the tropospheric ozone column is only included in the observed total column during cloud free observations. The cloudy observation with high cloud cover and high cloud altitude are used to determine the SOC, whereas the average total ozone column (TOZ) is calculated from the cloud free observations (cloud fraction less than 10%). Therefore the data are sampled on a certain grid and period, e.g. $1.25^\circ \times 2.5^\circ$ and one month of GOME-2 observations.

The stratospheric ozone column is determined over a reference region in the East Indian Ocean to the Pacific (70° E to 170° W). The convection in this region is strong and the local ozone concentration is low. Thereby we assume that the SOC is independent of the longitude and of the time (constant for one month) These two assumptions are only valid in the tropics, which limits the algorithm to 20° S to 20° N. The mitigation of the Inter-tropical Convergence Zone (ITCZ) is considered by using averages over certain latitude bands (1.25°).

For this study we used the GODFIT level 2 ozone data (*Lerot et al. 2010*) for the instruments GOME, SCIAMACHY, OMI and GOME-2. These four instruments together cover a period of 20 years from 1995 to 2015. The spectra observed by the satellites are all analyzed with the same algorithm. GODFIT uses a least-squares fitting inverse algorithm including direct multi-spectral radiative transfer simulation of earthshine radiances and Jacobians with respect to total ozone, albedo closure and other ancillary fitting parameters. The shielded ozone column below the cloud (= ghost column) is included by the fit's a priori profile. Also the local variations of tropospheric ozone are considered by using an ozone climatology for the troposphere based on OMI-MLS data (*Lerot et al. 2014*).

In contrast to the CCD retrieval described in *Valks et al. (2014)* the SOC results from the difference between total ozone column and the ghost column

$$SOC=TOZ - ghost$$

Further retrieval of the TTOC then follows the steps described above.

Harmonization

The long-term trend of tropospheric ozone is currently an issue of great scientific interest. Before calculating the trend for the 20 years of tropospheric ozone columns as observed by the four sensors GOME to GOME-2, the individual drifts of the instruments have to be taken into account. For the harmonization we selected SCIAMACHY on ENVISAT (2002-2012) as reference and compared the other data relative to SCIAMACHY. SCIAMACHY only showed a small drift compared to the ozone sondes.

For the correction a linear function and a combination of sine and cosine functions was fitted to the averaged differences between the TTOC of the other observers and SCIAMACHY (Fig. 3-10). Naturally the difference between SCIAMACHY and itself is zero. For GOME and OMI the correction is close to zero also compared to the fit's uncertainty (1σ fitting error). Therefore we decided not to include the linear fit here and just add the average offset between these sensors and the reference. Especially as for GOME even a small slope in the fit leads to large uncertainties when extrapolating back from 2002 to 1995. Only for GOME-2 a real offset and a trend is observed.

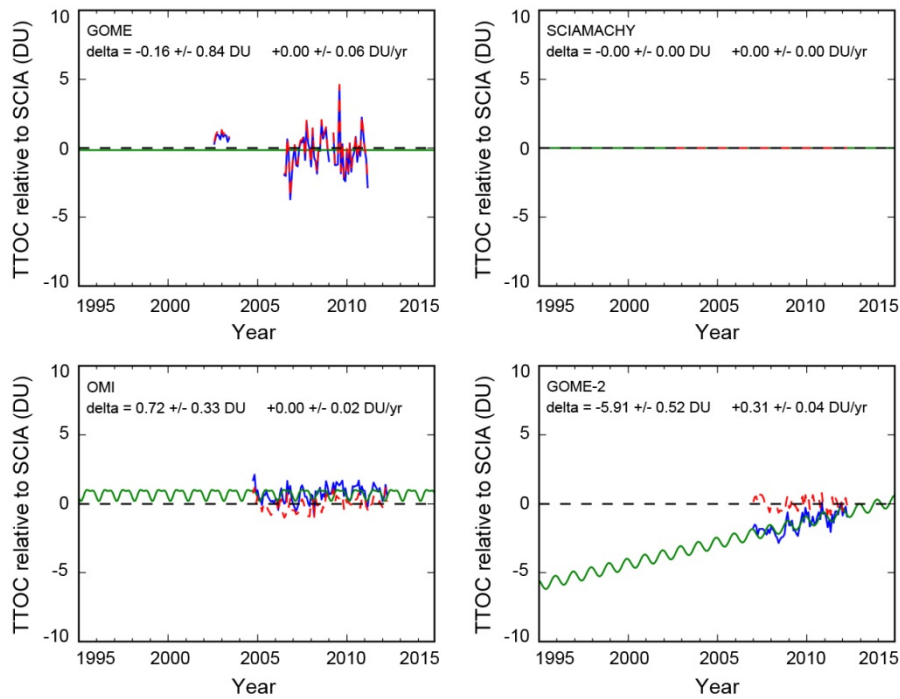


Fig. 3-10: Offset between the other sensors and SCIAMACHY, in blue the original offset, the green line denotes the fitted offset, and the dashed red line shows the corrected difference between the two sensors. For completeness SCIAMACHY is included in the figure; however the difference vanishes of course.

Trend fitting

After the harmonization a trend for 20 years of tropical tropospheric ozone can be derived. Therefore we gridded the monthly data to a $5^\circ \times 5^\circ$ grid for the individual sensors. Together with the linear term, a constant offset, a combination of sine and cosine functions (with the periods: 1 year, 6 month and 4 month) and indices for Quasi-Biennial Oscillations (QBO) and El Niño were fitted to the data of each grid cell. We considered each observation of the four sensors as individual data point and did not average all data points per month. The difference to the averaging approach however was small. The global trend map is shown in Fig. 3-11, areas with significant trends (the trend was larger than twice the fit error) were marked with crosses. The maximum trends reached up to 0.13 DU/yr over the last 20 years, and can be found close to the central African west coast, similar values are found over the central Pacific. A significant declining trend is observed over Central America. The largest decline in this region is 0.13 DU/yr. A stronger decrease (0.16 DU/yr) is found over South America at $\sim 17.5^\circ$ S. However, close to the edges of the tropics the CCD retrieval is unstable. In this region many data are missing from the GOME observations during the austral winter months. A comparable cause can be excluded over Central America.

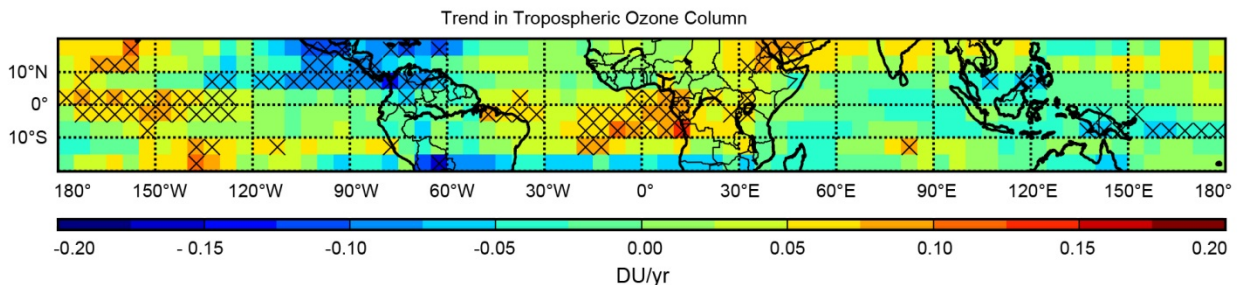


Fig. 3-11: Global trend map, for tropospheric Ozone in DU/year. The crosses mark the regions where the trend was significant (larger than 2σ). While over the tropical Atlantic and Pacific positive trends are observed, a decline in the tropospheric ozone is found over Central America.

Conclusions

Currently the different trends in tropospheric ozone columns can partly be explained. However, for some regions an explanation needs further studies. The increases over central Africa reaches out to the

Central Atlantic. The growing population in Central Africa means growing need for food and energy. Fire clearing of the rainforest for expanding agricultural areas or using wood for energy production are common approaches for satisfying these demands. Burning wood releases both NO_x and Volatile Organic Compounds (VOCs) which are the main ozone precursors. A similar explanation in combination with the rapid economic growth over the last two decades might hold for India and Indochina, even though the trend seems to be insignificant here. The TTOC increase over the central Pacific can hardly be explained by local pollution. In the upcoming years we will investigate the reasons for the unexplained increase there as well as for the decrease observed over Central America.

References

Lerot, C., Van Roozendaal, M., van Gent, J., Loyola, D. and Spurr, R.: The GODFIT algorithm: A direct fitting approach to improve the accuracy of total ozone measurements from GOME. *International Journal of Remote Sensing*, 31, 543-550, doi:10.1080/01431160902893576, 2010.

Lerot, C., Van Roozendaal, M., Spurr, R., Loyola, D., Coldewey-Egbers, M., Kochenova, S., van Gent, J., Koukoulis, M., Balis, D., Lambert, J.-C., Granville, J. and Zehner, C.: Homogenized total ozone data records from the European sensors GOME / ERS-2, SCIAMACHY / Envisat and GOME-2 / MetOp-A. *Journal of Geophysical Research*, 119, 3, 1639-1662, doi:10.1002/2013JD020831, 2014.

Valks, P., Hao, N., Gimeno Garcia, S., Loyola, D., Dameris, M., Jöckel, P., and Delcloo, A.: Tropical tropospheric ozone column retrieval for GOME-2. *Atmospheric Measurement Techniques*, 7, 2513-2530, doi:10.5194/amt-7-2513-2014, 2014.

3.6 Improved OCRA Cloud Fraction Retrieval Over Bright Surfaces

R. Lutz, S. Gimeno García, F. Romahn, D. Loyola

Clouds play a crucial role in the global radiation budget and are therefore of particular interest for climate studies and long term monitoring. But also in the retrieval of trace gas species, clouds are an important factor because their presence does significantly affect the calculation of the trace gas vertical columns. Knowledge about cloud properties, like cloud coverage (or cloud fraction) as well as cloud height and cloud optical thickness, are therefore a necessary ingredient in each trace gas retrieval.

Clouds can be characterized most efficiently by combining information from the UVN (Ultraviolet/Visible/Near Infrared) part of the spectrum with information in the micrometer range roughly between 1.6 and 10 μ . However, most instruments intended to provide trace gas information for Ozone, NO₂, SO₂ etc. are operating only in the UVN part of the spectrum. Examples for such instruments are the Global Ozone Monitoring Experiments (GOME and GOME-2), the Ozone Monitoring Instrument (OMI) and the upcoming TROPOspheric Monitoring Instrument (TROPOMI), which will have an additional channel in the SWIR.

The Optical Cloud Recognition Algorithm (OCRA – Loyola 1998) has been developed to retrieve the radiometric cloud fractional cover from information of the UVN range. Its basic characteristic is the comparison of a measured reflectance for a ground scene with a pre-calculated cloud-free reflectance background map (see Lutz *et al.* (2015) for a detailed description of the OCRA concept as well as its application to GOME-2 satellite data).

The OCRA cloud fraction algorithm relies on the two assumption that clouds appear to be “white” and “bright”. In this context, “white” means that cloud reflectance does not have a wavelength dependency in the UVN part and “bright” means that clouds have a higher reflectance than the underlying surface. The first assumption justifies the OCRA color space approach, which relates the deviation of the measured reflectance from the “white” situation (i.e. cloud fraction = 1) and the cloud-free situation (i.e. cloud fraction = 0) to a fractional cloud coverage in the range [0,1]. The second assumption holds true for most surface conditions but reaches its limits when dealing with very bright surfaces like snow or ice covered land, sea ice, permanent ice or oceanic sun glint. An approach to correct for the latter has been presented in the last annual report and here we would like to present an approach to improve the OCRA cloud fraction retrieval over snow/ice covered surfaces. Based on a global set of data covering all possible reflectances – from very dark (very low reflectance) to extremely

bright (very high reflectance) – and all possible intermediate scenes (associated with small/medium/high cloud coverage), OCRA defines a fixed scaling factor which more or less acts as an upper threshold. This upper threshold therefore defines to which position in the [0,1] cloud fraction interval a measured reflectance is scaled to. Using only one scaling factor for all possible surface conditions leads to an underestimation of the cloud fraction over very bright surfaces like snow and ice. This can be seen in Fig. 3-12. Shown are the radiometric cloud fractions based on OCRA for 2 February 2005 for measurements from the OMI instrument. In an attempt to correct for the underestimation of the cloud fraction over snow/ice surfaces, surface dependent scaling factors have been calculated for the following scenes: dry snow over land, ice over land, sea ice and permanent ice. The information on surface conditions have been taken from the near-realtime Ice and Snow Extent (NISE) snow ice information which is stored in the level 1 OMI data product. Fig. 3-13 shows the effect of implementing these adapted scaling factors: The improvement is evident in Antarctica and also at high latitudes, e.g. Alaska, Greenland, Siberia.

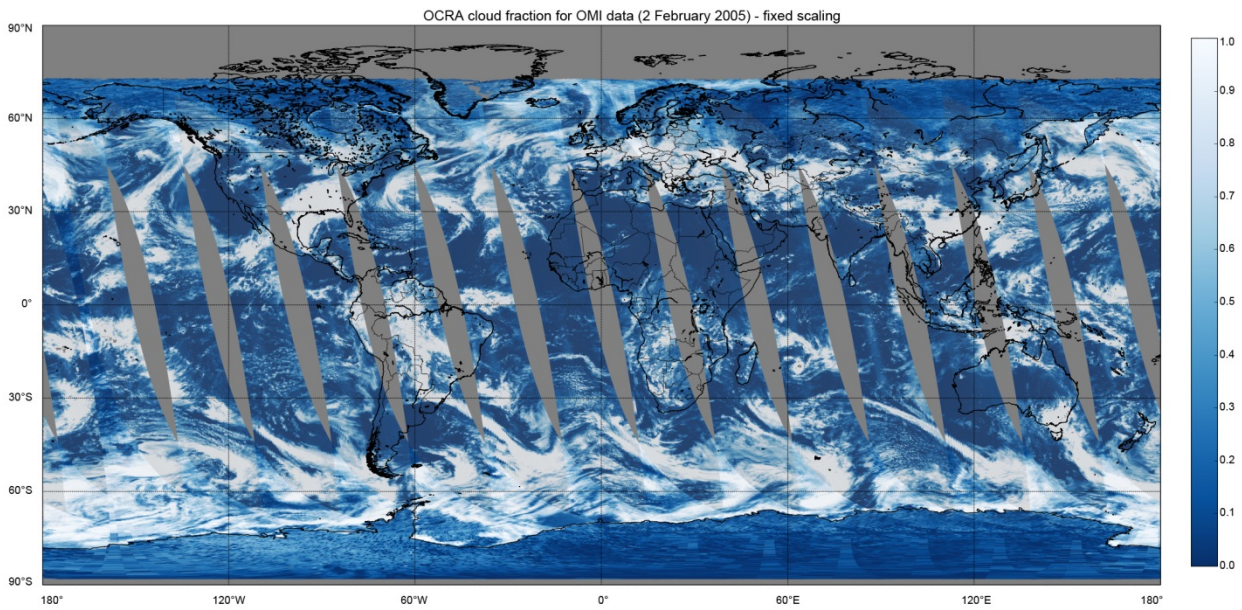


Fig. 3-12: OCRA radiometric cloud fraction for OMI data from 2 February 2005 with fixed scaling factor, independent on the surface (see text).

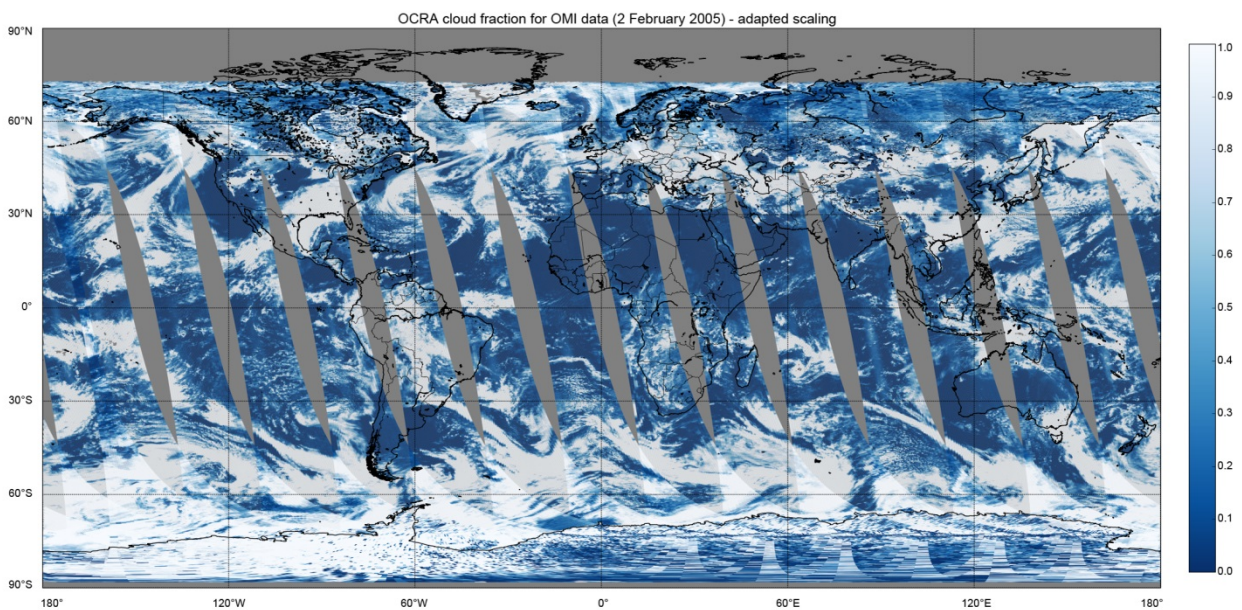


Fig. 3-13: Same as Fig. 3-12, but with adapted, surface dependent scaling factors (see text).

A qualitative comparison with MODIS (Moderate Resolution Imaging Spectroradiometer) real color RGB imagery supports the validity of this approach but further investigations on a larger data set are to be done in order to consolidate this algorithm update. It is also foreseen to adapt these algorithm updates to GOME-2 data and to implement them into the operational chain of the GOME-2 Data Processor (GDP).

References

Loyola, D.: A new cloud recognition algorithm for optical sensors. Geoscience and Remote Sensing Symposium Proceedings, IGARSS '98, IEEE International, 2 572-574, 1998.

Lutz, R., Loyola, D., Gimeno García, S., and Romahn, F.: OCRA radiometric cloud fractions for GOME-2 on MetOp-A/B. Atmospheric Measurement Techniques Discussion, 8, 13471-13524, doi:10.5194/amtd-8-13471-2015, 2015

3.7 Cloud Top Height and Optical Depth Retrieval using ROCINN

S. Gimeno García, R. Lutz, F. Romahn, D. Loyola, R. Spurr (RT Solutions)

Cloud information from UV/VIS/NIR spectrometers aboard spacecraft platforms is highly valuable for the construction of cloud property climatologies, since it is complementary to the information retrieved using IR spectrometers, imagers and active sensors (cloud radars and lidars). Clouds, when present, are the main modulators of the radiation transport across the atmosphere. They are very diverse in terms of composition (ice, liquid water), thickness (thin cirri to thick cumulonimbi), variability (homogeneous stratocumuli to inhomogeneous cumuli), altitude, etc. Consequently, the modeling of the cloud-radiation interaction is one of the most challenging tasks in the atmospheric science.

The distance that photons travel across the atmosphere before being captured by a space-borne instrument can be greatly affected by clouds. Absorption by atmospheric molecules is not only proportional to the molecular number density but also to the photon path length. Therefore, the effect of clouds on the photon path length is of particular interest in atmospheric remote sensing. During the retrieval processing, changes in the absorption bands within the spectra are analyzed. These changes can be linked to variations in the molecular number density but also to variations in the photon path length. Therefore, precise cloud information to correct for variations in the photon path length is mandatory for the accurate retrieval of atmospheric trace gases.

The ROCINN (Retrieval Of Cloud Information Through Neural Networks) algorithm retrieves cloud top height/pressure (CTH/P), cloud optical depth (COT) and cloud albedo (CA) from measurements in and around the oxygen A-band (~760 nm) taking as input the cloud fraction (CF) computed with the Optical Cloud Recognition Algorithm (OCRA). OCRA is a RGB color space approach which maps actual reflectance measurements to cloud radiometric fractions by comparison to cloud-free reflectance monthly maps that have been previously computed.

There are two variants of the ROCINN algorithm: one that treats clouds as reflecting boundaries (ROCINN-CRB), i.e. Lambertian equivalent reflectors and a second one that treats clouds as scattering layers (CAL). The ROCINN-CRB algorithm has been successfully used operationally for the GOME/ERS-2 and GOME-2/MetOp-A and -B instruments since over one decade. The CAL algorithm treats clouds in a more realistic way and provides cloud properties closer to reality. ROCINN V3.0 in the CRB and CAL variants has been included into the latest UPAS operational processor and is the baseline algorithm for the generation of cloud products from the atmospheric Sentinels.

Fig. 3-14 shows cloud albedo and cloud height as retrieved by ROCINN-CRB. These cloud properties were retrieved using GOME-2A data from 1 July 2009. The ROCINN-CRB cloud albedo product is much smoother than the OCRA cloud radiometric fractions (not shown here) and can be regarded as a kind of radiometric correction to it during the ROCINN inversion process. The ROCINN-CRB cloud height product exhibits much more variability capturing even the variability inside cloud mesoscale systems.

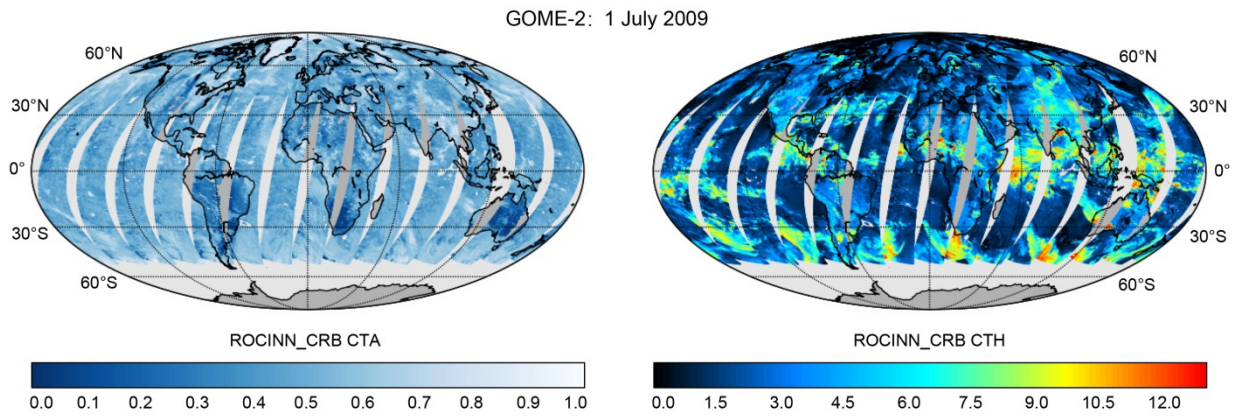


Fig. 3-14: GOME-2A cloud albedo (left) and cloud height (right) of 1 July 2009 using the cloud retrieval algorithm ROCINN-CRB.

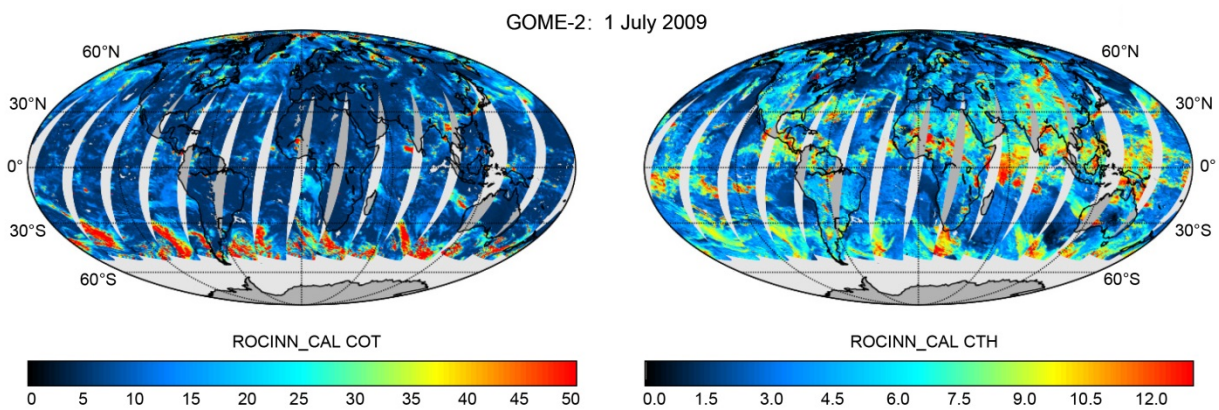


Fig. 3-15: Cloud optical thickness (left) and cloud top height (right). Same data as in Fig. 3-14.

Fig. 3-15 illustrates cloud optical thickness and cloud height as retrieved by ROCINN-CAL. The cloud properties correspond to the same data as Fig. 3-14. The ROCINN-CAL cloud optical thickness captures much more variability than the closely related quantity cloud albedo (Fig. 3-14, left panel). The main reason for that is that the CAL cloud model explicitly depends on the optical property COT instead of the radiometric quantity CA which has a lower correlation with CF allowing for better separation of the cloud information. Additionally, the CAL cloud top height is systematically higher than the CRB counterpart approaching the actual height of the cloud top boundary in opposition to the CRB cloud height which represents an altitude at the cloud radiometric centroid (below CTH and usually above cloud bottom height).

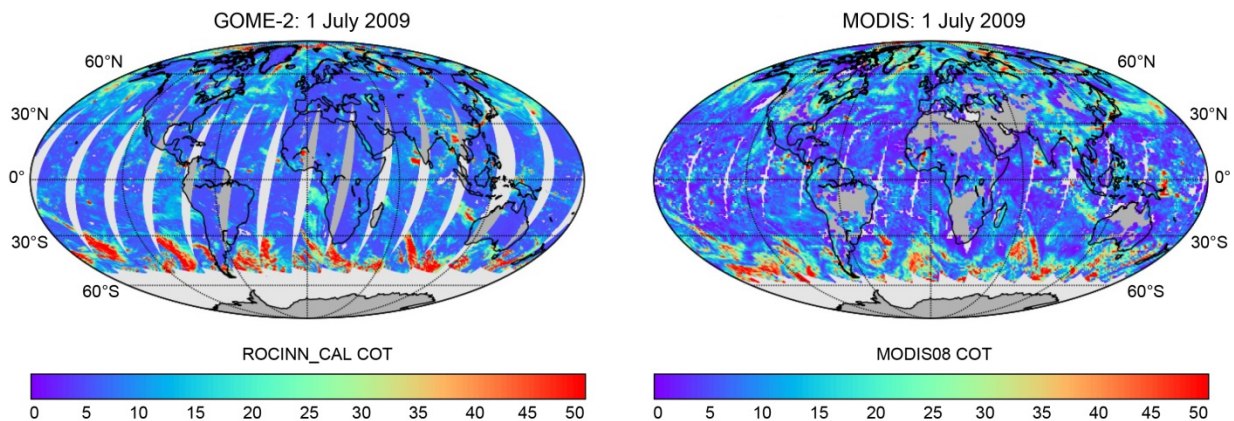


Fig. 3-16: Cloud optical thickness retrieved from GOME-2A data (left) and MODIS/Terra (right). Same date as in Fig. 3-15. The ROCINN-CAL COT has been replotted with a different color table for comparison purposes.

Fig. 3-16 compares the GOME-2A COT retrieved with ROCINN-CAL and the MODIS MOD08 COT product. The GOME-2 instrument is mounted on EPS/MetOp-A and MODIS on NASA-EOS/Terra which have an equatorial crossing time around 9:30 AM and 10:30 AM local time, respectively. Although both instruments have a time delay of about one hour, the COT retrieved by both instruments shows a good qualitative agreement.

References

Gimeno García, S., Lutz, R., Romahn, F., Loyola, D., Spurr, R.: GOME-2 cloud top height and optical depth retrieval using ROCINN V3.0. Proceedings of ATMOS 2015, SP-735, ESA Atmospheric Science Conference, University of Crete, Heraklion, Greece, 2015.

Schüssler, O., Loyola, D., Doicu, A., Spurr, R.: Information Content in the Oxygen A-Band for the Retrieval of Macrophysical Cloud Parameters. IEEE Transactions on Geoscience and Remote Sensing, 52, no. 6, pp. 3246-3255, 2014.

Loyola, D., Thomas, W., Livschitz, Y., Ruppert, T., Albert, P., Hollmann, R.: Cloud properties derived from GOME/ERS-2 backscatter data for trace gas retrieval. IEEE Transactions on Geoscience and Remote Sensing, 45/9, 2747-2758, 2007.

3.8 ADM-Aeolus Mie and Rayleigh Algorithm Performance Assessment

K. Schmidt, O. Reitebuch (IPA), and D. Huber (DoRIT)

The main goal of the ESA ADM-Aeolus mission consists in the acquisition of global vertical wind profiles from space using Lidar technology to improve the accuracy of weather and climate prediction. The Aeolus satellite will carry a Doppler wind Lidar, called *Aladin*, which will probe the lowermost 30 km of the atmosphere at a wavelength of 355 nm. It will measure Doppler shifts in the spectra of the laser light backscattered by moving atmospheric particles such as aerosols, cloud particles, and air molecules. Therefore both a Mie and a Rayleigh spectrometer are used and line-of-sight wind velocities can be derived.

Our involvement concerns investigations on the impact of different *Aladin* instrument settings and atmospheric scenes on the performance of the Mie and Rayleigh wind results. Recommendations for further algorithm refinements and quality control shall be derived.

We use the ADM-Aeolus End-to-End Simulator (E2S) for simulating the measurement flow for different atmospheric scenarios including wind conditions. Annotated instrument source packet data, suitable for L0-L1a-L1b processing, are the output of these simulations. Comparisons between the input and the resulting L1b Mie and Rayleigh channel winds allow assessing the algorithm.

Fig. 3-17 shows an example of such investigations. It has been obtained for a synthetic input wind velocity profile with strong wind speed gradients and two wind maxima of 30 m/s at an altitude of 0.5 km and 100 m/s at a height of 10 km (black line in the left figure). A high altitude cirrus cloud with an optical thickness of 0.4 has been taken into account, just ranging from 8 km to 12 km in the upper wind speed maximum (green lines in Fig. 3-17). Note that the E2S V.3.05 default aerosol extinction and backscatter profiles have been used. Their maxima are located in the altitude range of about 0 km to 3 km, just at the lower wind speed maximum. Note furthermore that the Downhill-Simplex Mie core algorithm has been applied in the L1 processing (see *Schmidt et al. 2015* for more details on the atmospheric and instrument settings).

Fig. 3-17 demonstrates that the mean L1b Rayleigh (red line) and Mie channel winds (blue line) obtained follow the trend of the input wind profile (left hand side of Fig. 3-17). Note that they have been averaged over various observations executed during an orbit over the Pacific Ocean. In particular, the presence of the aerosols and cirrus cloud particles enables Mie channel measurements in the maximum wind speed regions. On the other hand, the optical thickness of the cirrus cloud is small enough so that Rayleigh channel wind observations are still possible below it. However, their errors are

relatively large, mainly due to the aerosol contamination (right hand side of Fig. 3-17). Larger Rayleigh and Mie channel errors have been also obtained at the cloud boundaries having the largest wind gradients. This issue needs further investigation.

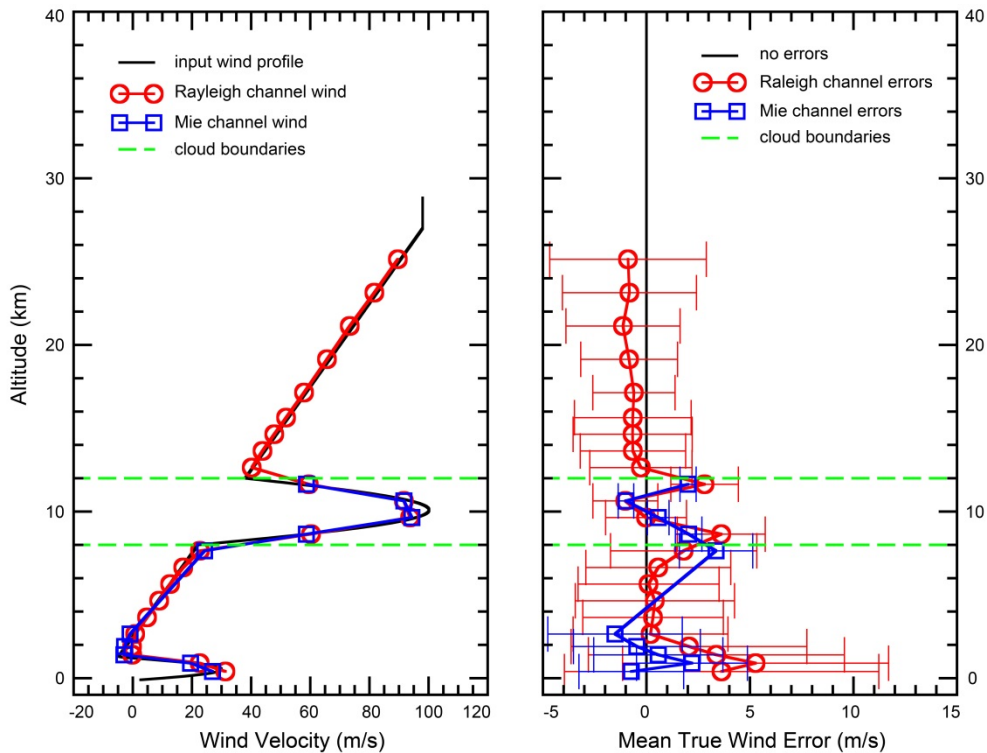


Fig. 3-17: Left: Comparison of the mean Rayleigh (red line) and Mie channel wind profile (blue line), obtained by an (E2S V.3.05 + L1bP V.6.04) simulation, with the corresponding synthetic input wind velocity profile (black line). Right: Obtained mean true wind errors including their standard deviations as error bars. The range of a cirrus cloud considered is marked by the green dashed lines.

References

Schmidt, K., Reitebuch, O., and Huber, D.: Mie and Rayleigh Algorithm Performance Assessment, AE.TN.DLR.5100.2.20151214, V.1.0, 14.12.2015.

3.9 Development of Atmosphere-Water Coupled Radiative Transfer

D.S. Efremenko, T. Trautmann

Atmospheric correction is the process of removing the effects of the atmosphere on the reflectance values of images taken by satellite or airborne sensors. A common approach for this is to eliminate the influence of the atmosphere by using the solution of the radiative transfer equation (RTE). At the German Remote Sensing Data Center (DFD) the ATCOR (Atmospheric/Topographic Correction for Satellite Imagery) software package was developed. Currently we are working on the project AC2020, in which our intention is to extend the ATCOR capabilities with respect to usability for water bodies. For this reason we are developing the coupled atmosphere/ocean radiative transfer model.

We have been working on designing a coupled radiative transfer model by generalizing the matrix exponential formalism to the case of multi-layer medium with different refractive indexes. This activity resulted in the radiative transfer solver CDOME (Coupled Discrete Ordinate with Matrix Exponential). In 2015 our coupled radiative transfer model was validated against several coupled models including LIDORT (Spurr et al. 2007), SCIATRAN (Rozanov et al. 2014) and FEMWAT (Bulgarelli et al. 1999). The comparison of these codes is given in Fig. 3-18. We obtained an agreement within 2%. Note that this difference appears mostly in the post-processing step involving computations of the TMS correction,

single scattering correction, etc. All considered radiative transfer codes provide results with discrepancy less than 0.1% for the phase functions smoothed by the delta-M truncation. Currently we are planning a new benchmark campaign to remedy such disagreements.

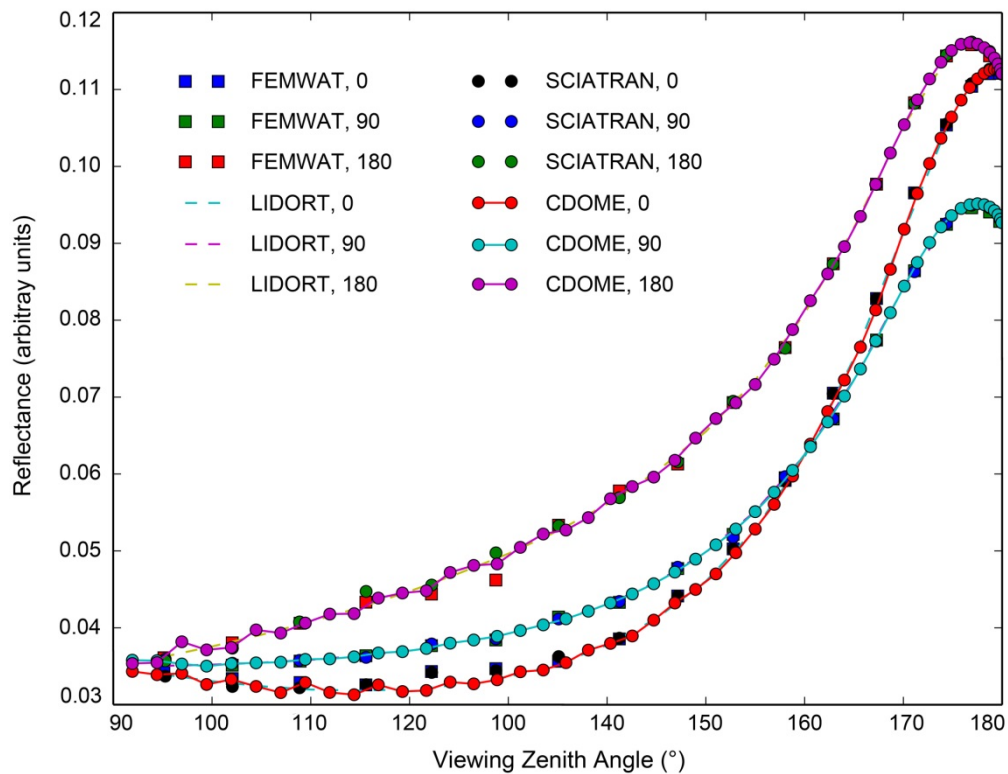


Fig. 3-18: Angular distribution of the radiance reflected by multilayer coupled atmosphere-ocean model at three relative azimuth angles (0, 90, 180 degrees). Results are from the following radiative transfer codes: FEMWAT, LISORT, SCIATRAN and CDOME.

References

Spurr, R., Stamnes, K., Eide, H., Li, W., Zhang, K., Stamnes, J.: Simultaneous retrieval of aerosols and ocean properties: A classic inverse modeling approach. I. Analytic Jacobians from the linearized CAO-DISORT model. *Journal of Quantitative Spectroscopy and Radiative Transfer*, 104, 428-449, 2007.

Rozanov, V.V., Rozanov, A.V., Kokhanovsky, A.A., Burrows, J.P.: Radiative transfer through terrestrial atmosphere and ocean: Software package SCIATRAN. *Journal of Quantitative Spectroscopy and Radiative Transfer*, 133, 13-71, 2014.

Bulgarelli, B., Kisselev, V., Roberti, L.: Radiative Transfer in the Atmosphere-Ocean System: The Finite-Element Method. *Applied Optics*, 38, 1530-1542, 1999.

3.10 First Retrieval Results of Atmospheric Temperature from ML-CIRRUS Campaign

J. Xu, F. Schreier, T. Trautmann, M. Kenntner (IPA), M. Szajkowski (WRUT), J. Zhang (TUM)

The MTP (Microwave Temperature Profiler) instrument (Mahoney and Denning 2009) aboard research aircrafts was designed to regionally map spatial and temporal aspects of atmospheric temperature in the upper troposphere and lower stratosphere. MTP employs double sideband biased mixers and detects oxygen lines at the frequency range of 55 to 60 GHz. The HALO-MTP instrument uses local oscillator (LO) frequencies of 56.363, 57.612, and 58.363 GHz. Essentially, a measurement cycle contains a set of 30 brightness temperatures at 3 LO frequencies and at 10 viewing angles.

The retrieval code TIRAMISU (Temperature Inversion Algorithm for Microwave Sounding), built on GARLIC (Generic Atmospheric Radiation Line-by-line Infrared Code) and PILS (Profile Inversion for Limb Sounding), has been used to derive vertical profiles of atmospheric temperature from the measurement data. Python scripts have been implemented to process the data in an efficient manner. The state vector comprises the temperature profile and a polynomial for baseline offset.

This study focused on the ML-CIRRUS campaign that took place between 26 March and 15 April 2014. The objective area was cirrus and contrail cirrus in the mid latitude tropopause region in Europe and the North Atlantic. The corresponding results are important to resolve a variety of phenomena in the Upper Troposphere Lower Stratosphere (UTLS) region and to potentially improve the space-borne temperature soundings.

Fig. 3-19 depicts first retrieval results from a morning flight which took place on 11 April 2014 over Great Britain. As the HALO aircraft was ascending gradually, we obtained more vertical information accordingly. The variations between each temperature profile may be due to the fact that the instrument was in a warming-up stage and had not been fully stable.

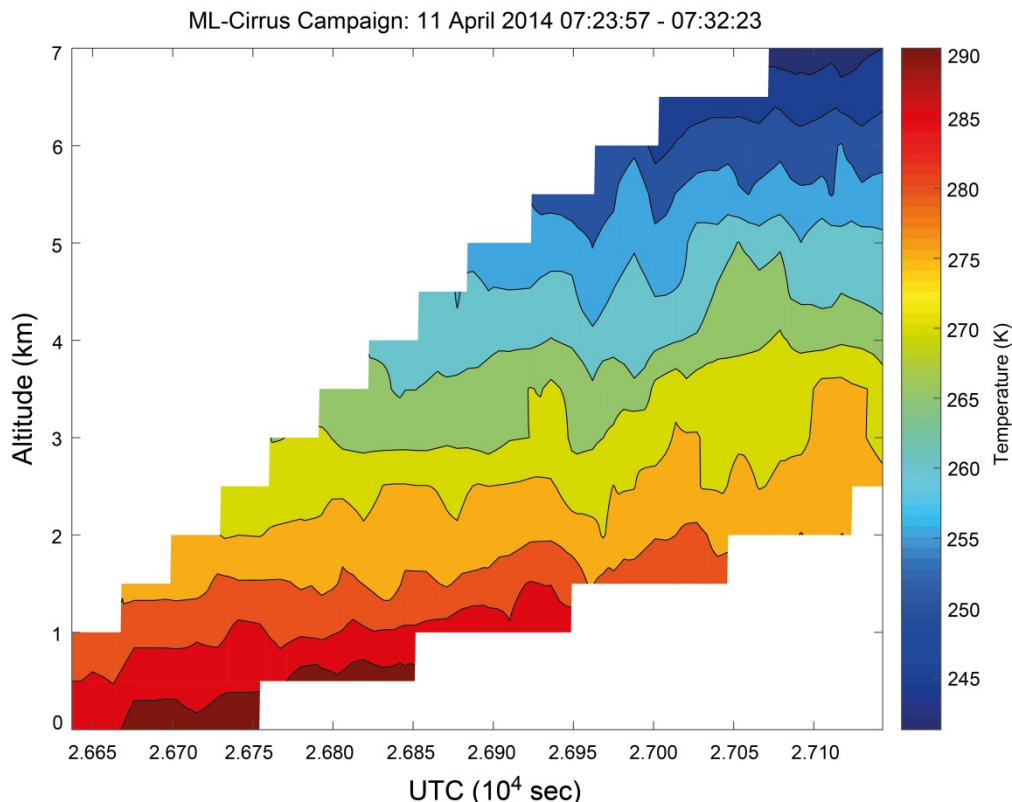


Fig. 3-19: Retrieved atmospheric temperature with respect to altitude and measuring time (UTC second). The retrievals are done for the morning data from a ML-CIRRUS campaign flight which took place on 11 April 2014.

In Fig. 3-20, the modeled intensities after convergence in units of brightness temperature are compared against the observed ones for a cycle of the MTP data. Overall, both intensities reach an agreement except a few discrepancies at 55°.

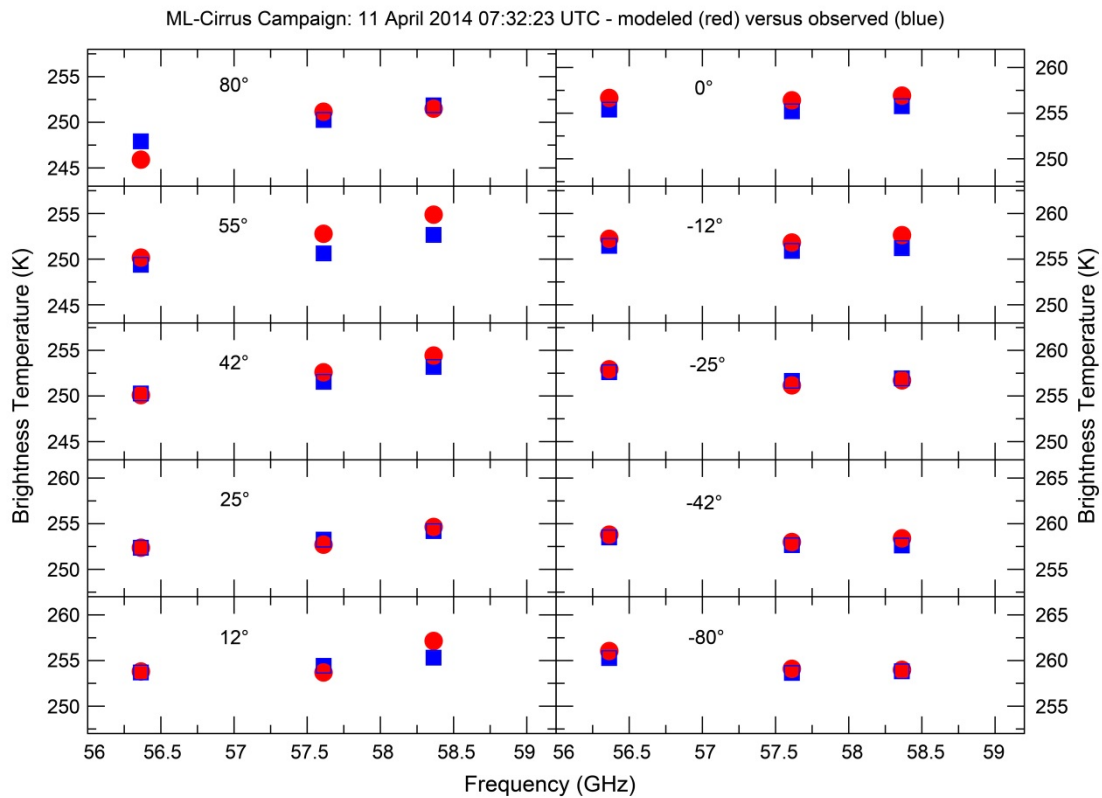


Fig. 3-20: Comparison of the modeled intensities after convergence with the observed intensities for one cycle of the MTP data which was measured in the ML-CIRRUS campaign. 10 viewing angles relative to the horizon are indicated in each subfigure.

Ongoing efforts to improve the MTP products are currently focusing on modernizing/optimizing the retrieval software. Furthermore, an intercomparison of the inversion performance between TIRAMISU and the Bayesian statistical method (*Nielson-Gammon et al. 2008*) will be conducted. Ground-based observations and in-situ profiles using dropsondes will be used to validate the MTP profiles.

References

Mahoney, M.J. and Denning, R.: A State-of-the-art Airborne Microwave Temperature Profiler (MTP). Proceedings of the 33rd International Symposium on the Remote Sensing of the Environment, Stresa, Italy, 4-8 May, 2009.

Nielson-Gammon, J.W., Powell, C.L., Mahoney, M.J., Angevine, W.M., Senff, C., White, A., Berkowitz, C., Doran, C., Knupp, K.: Multisensor estimation of mixing heights over a coastal city. *Journal of Applied Meteorology and Climatology*, 47, 27-43, doi:10.1175/2007JAMC1503.1, 2008.

3.11 Py4CA_TS – Python Tools for Computational Atmospheric Spectroscopy

F. Schreier, S. Gimeno García, J. Xu

Radiative transfer modeling is an important aspect of atmospheric physics and chemistry, both for Earth and planetary atmospheres. In particular, for the analysis of remote sensing data as well as for theoretical investigations such as retrieval assessments, a flexible, yet efficient and reliable radiative transfer code is mandatory. In view of the increasing number of high resolution instruments and thanks to the increasing computational power, line-by-line (lbl) modeling of high resolution infrared (IR) and microwave (μ W) spectra is widely used today. Although highly optimized codes written in compiled languages such as Fortran or C/C++ are indispensable for operational processing, radiative transfer tools developed in script languages such as Python are an interesting alternative. Despite the reduced execution speed, script based tools are attractive because they allow for “rapid prototyping”, can be executed on a large variety of platforms, and provide easy access to intermediate quantities, hence facilitating visualization and better understanding of the physics.

Py4CA_TS is a (partial) re-implementation of GARLIC, our *Generic Atmospheric Radiation Line-by-line Infrared Code* (Fortran) which has been in development since several years. Compute-intensive code sections utilize the Numeric/Scientific Python modules for highly optimized array-processing. In the framework of the ESAS-Light study funded by ESA-ESTEC, the lbl modules of Py4CA_TS were selected to provide a user-friendly tool to generate high resolution molecular optical depths as an input for the libradtran radiative transfer solver (see our 2010 annual report).

Until recently the tools provided in Py4CA_TS could only be used as commands from the Unix/Linux shell. The individual steps of an IR/ μ W radiative transfer computation (Fig. 3-21) are implemented in separate scripts (Python modules) to

- to extract lines of relevant molecules in the spectral range of interest,
- to compute lbl cross sections for given pressure(s) and temperature(s),
- to combine cross sections to absorption coefficients and optical depths,
- and to integrate along the line-of-sight to transmission and radiance/intensity.

All these scripts read their input from external files and save their results in files, too. As a consequence, I/O operations can become quite time-consuming and a large part of the scripts was devoted to check the consistency of the input.

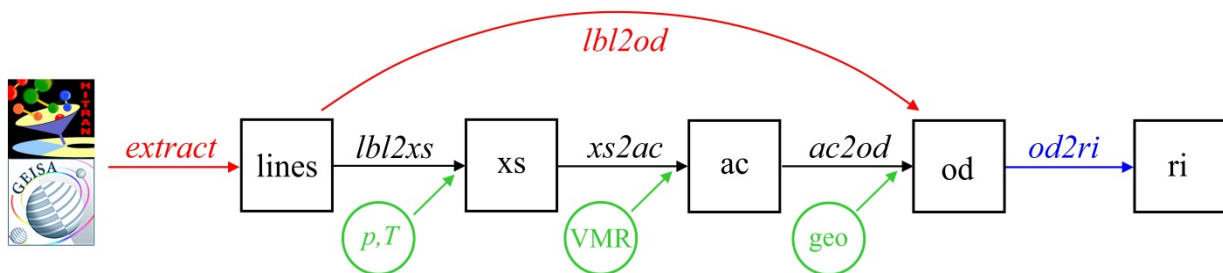
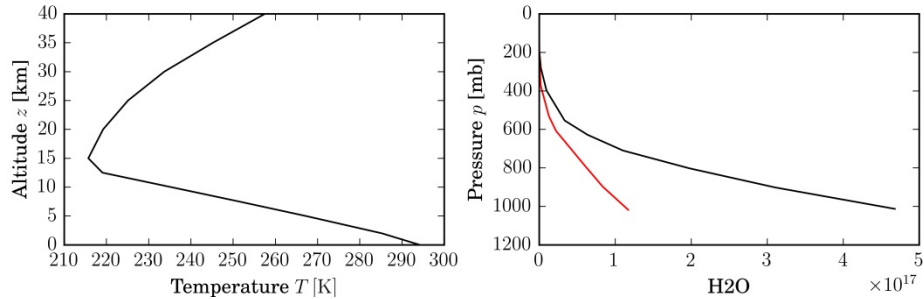


Fig. 3-21: Sketch of the individual steps of an IR/ μ W radiative transfer computation.

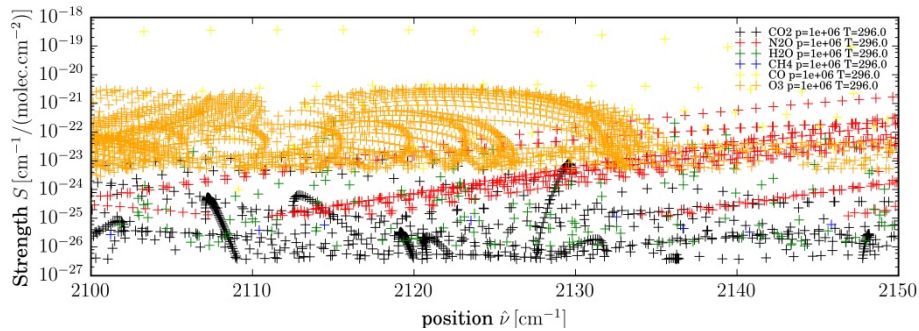
However, in view of the impressive advancements and progress of inter-active Python shells, in particular IPython (see www.ipython.org), the scripts have been substantially rewritten to provide an easy way to do lbl modeling within (i)python. In essence, the main computational function of each Python module can be called directly in the (i)Python interpreter and typically returns an array of the spectrum. For example, the lbl2xs function returns molecular absorption cross section(s), and the Python module lbl2xs.py reads its input data first, calls its lbl2xs function, and saves (writes) the cross section data to some output file(s). Most functions have a variety of optional arguments, e.g. pressure and temperature etc. in case of lbl2xs. In addition to the computational functions the interactive Py4CA_TS environment offers a variety of I/O utilities and several functions to ease the visualization of the (intermediate) results.

Python 2.7.6 (default, Nov 21 2013, 15:55:38) [GCC]
 IPython 1.0.0 -- An enhanced Interactive Python.
 INFO --- py4cats: setup done

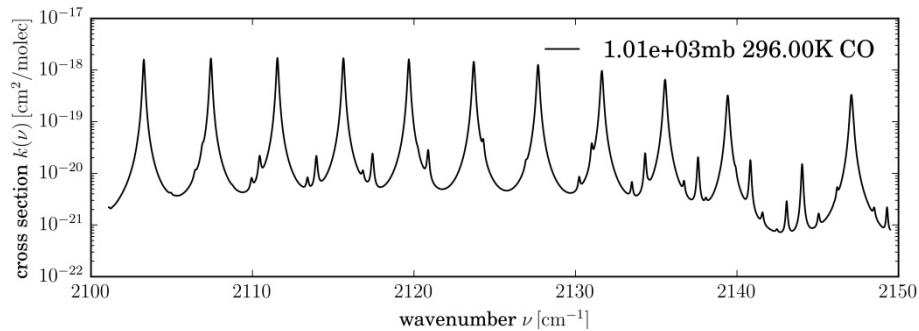
```
In [1]: mls = atmos1D('/data/atmos/20/mls.xy',zToA=40);
...: mlw = atmos1D('/data/atmos/20/mlw.xy',zToA=40);
In [2]: atmPlot(mls); atmPlot([mls,mlw],'H2O','mb')
```



```
In [3]: dll = extract_lines('/data/hitran/86/lines', (2100.,2150.), 'main')
3784 lines of 6 molecules extracted (returning a dictionary of line lists)
In [4]: atlas(dll)
```



```
In [5]: xs = lbl2xs(dll['CO']) # explore cross sections for CO only
In [6]: xsPlot(xs)
```



```
In [7]: vGrid, dod = lbl2od(mls,dll) # delta optical depths for all gases
In [8]: odPlot(dod,vGrid) # quickplot
```

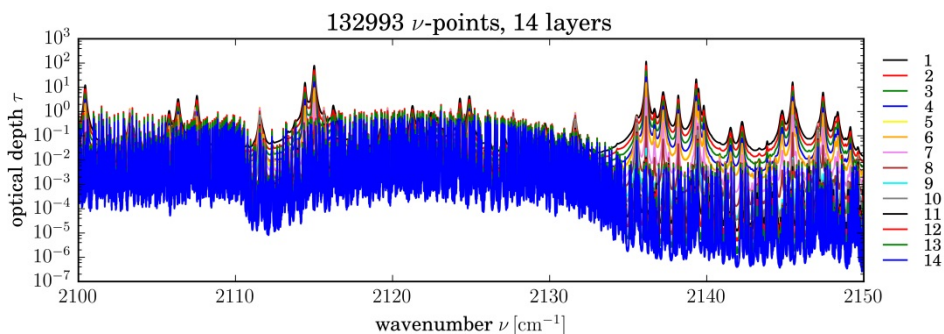


Fig. 3-22: Illustration of a typical lbl workflow.

Fig. 3-22 gives an impression of a “typical” workflow. First atmospheric data for two midlatitude summer/winter atmospheres and line-parameters from the Hitran database are read and plotted. To get an idea about the CO absorption, its cross section is computed and plotted. Finally, the layer optical depths for all molecules are evaluated and can now be used as input for any radiative transfer solver.

Py4CATs can be downloaded from <http://atmos.eoc.dlr.de/tools/Py4CATs>.

3.12 A Look Into Various Regularization Parameter Selection Methods

J. Xu, F. Schreier, A. Doicu, T. Trautmann

Inverse problems occurring in atmospheric science aim to estimate atmospheric state parameters from indirect data. On the subject of these ill-posed inverse problems, the major challenge in the framework of Tikhonov regularization concerns the choice of the regularization parameter, which provides the necessary impetus to investigate the design and robustness of the inversion algorithm.

In the framework of Tikhonov regularization, the estimation of the state vector \mathbf{x} from the measurement data \mathbf{y}^δ can be formulated as a minimization problem involving the objective function

$$\mathcal{F}(\mathbf{x}) = \|\mathbf{F}(\mathbf{x}) - \mathbf{y}^\delta\|^2 + \lambda \|\mathbf{L}(\mathbf{x} - \mathbf{x}_a)\|^2.$$

The regularization parameter λ plays an important role in whether a solution gives an optimal compromise between the residual term $\|\mathbf{F}(\mathbf{x}) - \mathbf{y}^\delta\|^2$ and the penalty term $\|\mathbf{L}(\mathbf{x} - \mathbf{x}_a)\|^2$.

In this study, we compared the retrieval performance of five regularization parameter selection methods, i.e.

- the expected error estimation (EEE),
- the discrepancy principle (DP),
- the generalized cross-validation (GCV),
- the maximum likelihood estimation (MLE), and
- the L-curve (LC).

To achieve this goal, we considered the temperature test problem using synthetic data by MTP (Microwave Temperature Profiler, see chapter 3.10), which was designed to be mounted on an aircraft. It is worth mentioning that these methods are formulated in a semi-stochastic setting and the noise level can be estimated as $\Delta^2 = m\sigma^2$ with m being the number of measurements and σ being the noise standard deviation. The selection criterion with constant regularization parameter is taken into account, which means that the minimization of the Tikhonov function is done a few times with different regularization parameters.

The atmospheric temperature profile was retrieved from the MTP data in a spectral interval ranging from about 56 to 59 GHz. The output of each MTP measurement contained a set of 30 brightness temperatures with respect to 3 frequencies and 10 viewing angles. The observer altitude was set to 10.0 km. The exact state vector was chosen as an interpolated version of a climatological profile discretized in a denser step close to the observer and in a coarser step far from the observer. The noisy data vectors were generated for an ensemble of 42 climatological atmospheres and three noise standard deviation scenarios ($\sigma = 0.05, 0.1, \text{ and } 0.2$), which means that the number of noisy data realizations was 126. For each noisy data vector, the regularization parameter was estimated by a particular parameter selection method.

A summary of the analysis of the regularization parameter selection methods is shown in Table 3-1. The average values of the solution errors and residual over noisy data realizations – for the three noise standard deviations (σ) – are presented regardless of whether the particular method fails in some situations. Most methods except the L-curve lead to comparable residuals after convergence for the three noise realizations.

Method	Relative Solution Error			Residual		
	$\sigma = 0.05$	$\sigma = 0.1$	$\sigma = 0.2$	$\sigma = 0.05$	$\sigma = 0.1$	$\sigma = 0.2$
EEE	0.15	1.15	5.10	3.01	17.15	26.49
DP	1.31	2.48	8.02	3.97	17.50	26.22
GCV	0.30	2.39	9.37	3.15	16.92	26.18
MLE	0.12	1.80	5.79	3.04	17.01	26.63
LC	2.68	3.47	6.94	5.15	21.93	30.50

Table 3-1: Average values of relative solution errors and residuals of temperature retrieval for five regularization parameter selection methods.

Figure 3-23 depicts an example of retrieved temperature profiles by using the five regularization parameter selection methods. The regularization parameter chosen by the error estimation and the maximum likelihood estimation reproduces the retrieved profile close to the true profile, whereas the parameter chosen by the discrepancy principle and the L-curve is a bit overestimated and the retrieval seems a bit off from the true profile.

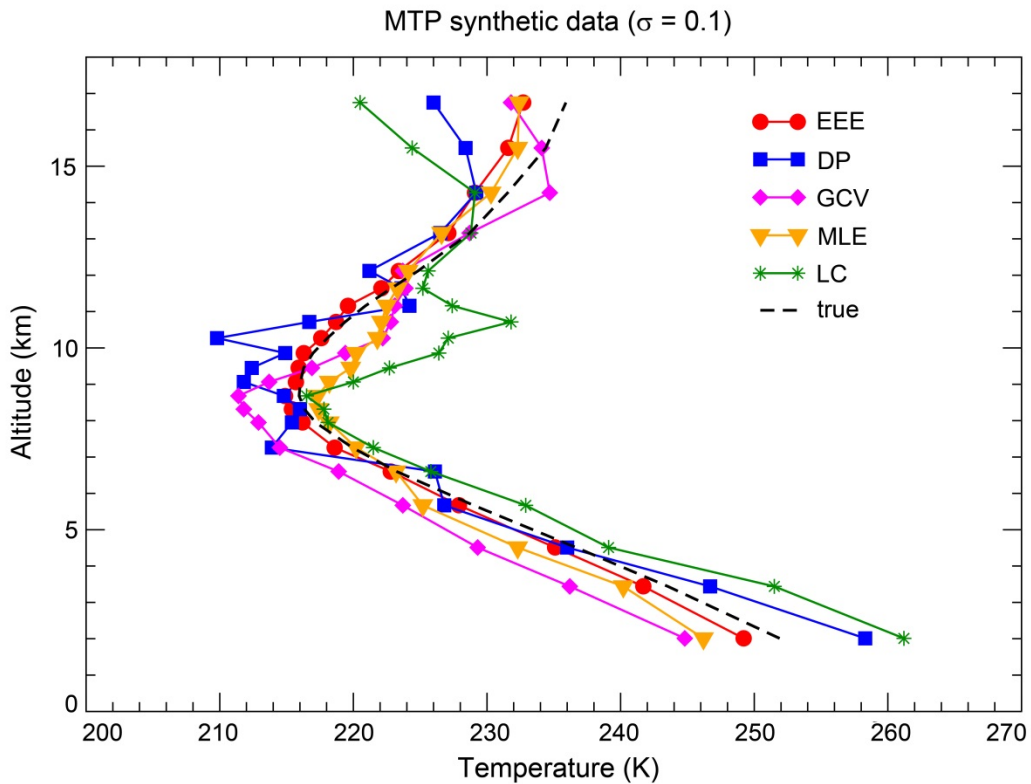


Fig 3-23: Temperature retrieval from a cycle of MTP synthetic data. The five regularization parameter selection methods are used for the comparison.

Based on these results we may draw the following conclusions:

- The expected error estimation depends on the knowledge of a solution domain with physical meaning. Although the chosen regularization parameter gives the best estimate, it is time-consuming as compared to other methods.
- The solution errors corresponding to the discrepancy principle are very sensitive to the control parameter.
- The generalized cross-validation curve may have a very flat minimum which is difficult to be located.
- The maximum likelihood estimation is comparable with the expected error estimation, despite occasional failures by producing under-regularized solutions.

- The L-curve method sometimes leads to unconvincing results with overestimated λ , even though the implementation is efficient.

Practical tests of different parameter selection methods reveal that at the current stage, there is currently no method balancing up accuracy and efficiency in the best possible manner.

References

Doicu A., Trautmann T., and Schreier S.: Numerical Regularization for Atmospheric Inverse Problems. Springer-Verlag, Berlin Heidelberg, Germany, doi: 10.1007/978-3-642-05439-6, 2010.

Engl H.W., Hanke M., and Neubauer A.: Regularization of Inverse Problems. Kluwer Academic Publishers, Dordrecht, The Netherlands, 2000.

3.13 The Invariant Imbedding T-Matrix Approach: Revision

A. Doicu, D.S. Efremenko, T. Trautmann

In atmospheric radiative transfer and remote sensing, accurate computations of electromagnetic scattering by large particles with extreme geometries are often required. The null-field method (otherwise known as the extended boundary condition method) is suitable for analyzing the electromagnetic scattering by large and highly aspherical particles. The method was initially proposed by *Waterman (1965)*. In the framework of the null-field method, the transition matrix relating the expansion coefficients of the scattered and incident field is derived as

$$\mathbf{T} = -\mathbf{Q}^{11} (\mathbf{Q}^{31})^{-1},$$

where the matrix \mathbf{Q}^{31} is obtained by imposing the null-field condition inside a spherical surface enclosed in the particle, and the matrix \mathbf{Q}^{11} is obtained from Huygens principle. The elements of the \mathbf{Q} matrices are expressed as integrals of products of spherical vector wave functions (SVWF) over the particle surface. Despite its wide range of applicability, the method suffers from numerical problems regarding convergence and loss of accuracy. The reason is that for large and/or strongly deformed particles, the matrix \mathbf{Q}^{31} becomes severely ill-conditioned, and the inversion process is negatively influenced by round-off errors. The null-field method is used to initialize the iterative procedure involved in the invariant imbedding method, or equivalently, to compute the T matrix of a partial volume of the particle whose surface is the initial position in the invariant imbedding iteration. This fact motivates our research in the field of electromagnetic scattering by large particles (*Doicu et al. 2015*).

In 2015 we were focused on the theoretical fundamentals of the invariant imbedding T matrix approach. We rediscovered the recurrence relation for the T matrix by using an integral-matrix approach. The invariant imbedding T matrix approach originates from an electromagnetic volume integral equation in spherical coordinates and on the equivalence between the scattering by a nonspherical particle and the scattering by the inhomogeneous circumscribed sphere. Essentially, it is assumed that the particle is entirely contained within a sphere of radius R and interior D , and is completely described by specifying the relative refractive index $m_r(\mathbf{r})$ as a function of the position vector \mathbf{r} in D . In the exterior of D , we have $m_r(\mathbf{r}) = 1$. The method can be summarized as follows:

1. Starting from a volume integral equation and using the representation of the free space dyadic Green function in terms of spherical vector wave functions, an ordinary Fredholm integral equation for the radial amplitude vector is derived.
2. The Fredholm integral equation is discretized with respect to the radial coordinate, the invariant imbedding procedure is applied to the discretized equation, and a two-terms recurrence relation for the \mathbf{T} -matrix is obtained.
3. Passing to the limit $\Delta R \rightarrow 0$ in the \mathbf{T} -matrix recurrence relation, where ΔR is the radial grid spacing, a matrix Riccati equation for the \mathbf{T} -matrix is derived.

In our analysis we derive the matrix Riccati equation for the T matrix by applying directly the invariant

imbedding procedure on the continuous form of the Fredholm integral equation. We developed a numerical method for integrating the Riccati equations, which yields a new recurrence relation for the **T**-matrix. Finally, we rediscover the **T**-matrix recurrence relation established by *Johnson (1988)* in the framework of an integral-matrix approach.

The theoretical foundation of the invariant imbedding **T**-matrix approach has been revised, the connection with the superposition **T**-matrix method has been established, and two new recurrence relations for the **T**-matrix have been derived. This method is especially attractive because it can be used in combination with the null-field method with multiple spherical vector wave functions to handle strongly deformed particles of large size parameter.

References

Doicu A., Eremin Y., Efremenko D., Trautmann T.: Methods with discrete sources for electromagnetic scattering by large axisymmetric particles with extreme geometries. *Journal of Quantitative Spectroscopy and Radiative Transfer*, 164, 137-146, 2015.

Johnson, B.R.: Invariant imbedding T-matrix approach to electromagnetic scattering. *Applied Optics*, 27, 4861-4873, 1988.

Waterman, P.C.: Matrix formulation of electromagnetic scattering. *Proceedings 1965 IEEE*, 53, 805-812, 1965.

3.14 A Combination of Rayleigh Scattering and Mach-Zehnder Interferometry to Violate the CHSH-Inequality

T. Rother

In 1964 J.S. Bell published a famous paper regarding the Einstein-Podolsky-Rosen (EPR) paradox. In this paper he derived an inequality – formulated in terms of correlation functions – for a certain class of probability experiments. He proved that this inequality must hold for any classical probability experiment but may be violated in Quantum Mechanics. In 1969, 5 years later, J. Clauser, M. Horne, A. Shimony, and R. Holt published an alternative inequality – the so-called CHSH-inequality – that has become a much cited relation (*Clauser et al. 1969*). The impossibility to violate the CHSH-inequality by any classical experiment is an aspect being controversially discussed in Physics until today. A first classical optics experiment was proposed and performed by Borges et al. in 2010. They used a special setup with a non-separable spin-orbit mode of a laser beam to demonstrate the violation of the CHSH-inequality if formulated in terms of intensities rather than in probabilities (*Borges et al. 2010*).

Based on our experience in light scattering we were able to propose an alternative classical optics experiment which also results in a violation of the CHSH-inequality if formulated in terms of intensities. The corresponding experimental setup is presented in Fig. 3-24.

The CHSH-inequality reads

$$|C(\alpha, \beta) - C(\alpha, \beta')| + |C(\alpha', \beta) + C(\alpha', \beta')| \leq 2 .$$

The correlation functions that enter into the CHSH-inequality are calculated according to

$$C(\alpha, \beta) = \frac{1}{I_g} (I_{hh} + I_{vv} - I_{hv} - I_{vh})$$

where

$$I_g = (I_{hh} + I_{vv} + I_{hv} + I_{vh}).$$

Correlation measurements can be applied in a similar manner as known from scattering experiments, i.e. the deviation of an initially given correlation or a combination of correlations can be used to gain

information about the disturbance that causes this deviation. The CHSH-inequality – especially if used with parameter sets resulting in a maximum violation – is just one example that provides us with such an initial combination of correlations.

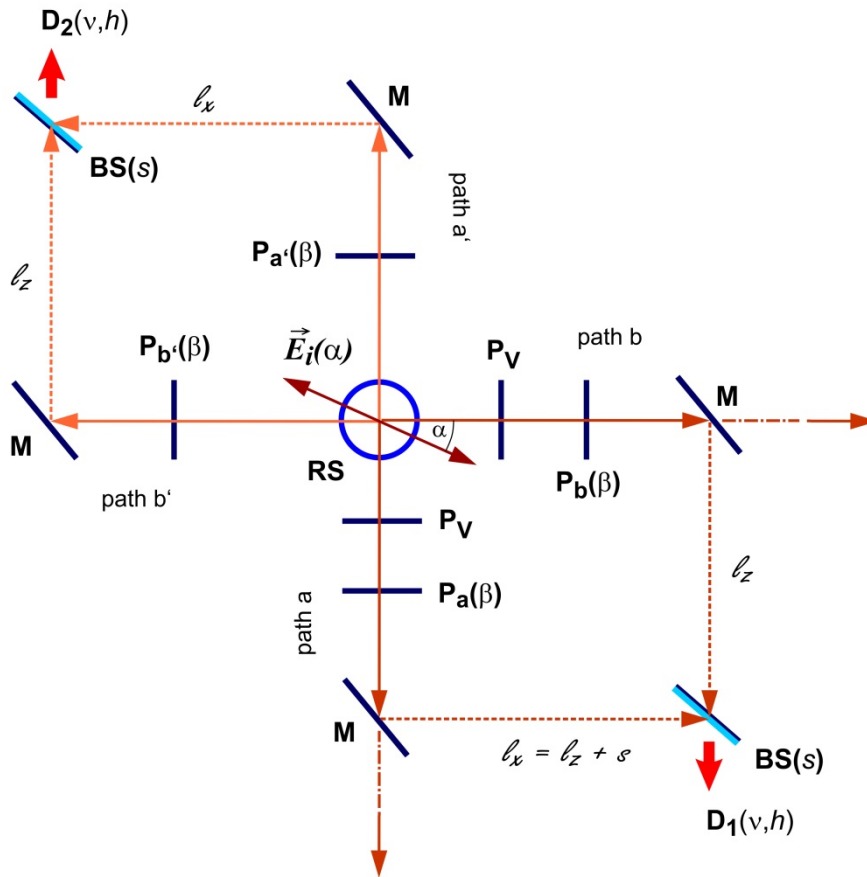


Fig. 3-24: Combination of a Rayleigh scatterer (**RS**) with two Mach-Zehnder interferometers and 6 additional $\lambda/2$ -wave plates (**P_v**, **P_a(β)**, **P_{a'}(β)**, **P_b(β)**, **P_{b'}(β)**) to rotate the plane of polarization. Intensities measured at **D₁(ν, h)**: $I_{\nu\nu}$, $I_{\nu h}$; intensities measured at **D₂(ν, h)**: I_{hh} , $I_{h\nu}$

Furthermore it can be demonstrated that a T-matrix and a Green's function both relate to the experiment shown above. The T-matrix is determined in a similar way known from light scattering. It represents the decisive element of the interaction part of the Green's function. A statistical operator can alternatively be used to describe this experiment. This statistical operator – well-known from Quantum Mechanics – contains negative weighting functions. These functions may be interpreted as sinks of two of the intensities measured in the experiment.

The combination of classical light scattering with correlation experiments such as proposed in Fig. 3-24 may open new ways for the development of diagnostic methods in modern optics. More details about the proposed experiment and its description in terms of a corresponding Green's function as well as a statistical operator can be found in *Rother (2015)*.

References

Clauser, J.F., Horne, M.A., Shimony, A., Holt, R.A.: Proposed experiment to test local hidden-variable theories, *Physical Review Letters*, 23, 880, 1969.

Borges, C.V.S., Hor-Meyll, M., Huguenin, J.A.O. and Khoury, A.Z.: Bell-like inequality for spin-orbit separability of a laser beam, *Physical Review A*, 82, 033833, 2010.

Rother, T.: Violation of a Bell-like inequality by a combination of Rayleigh scattering with a Mach-Zehnder setup, *Journal of Quantitative Spectroscopy and Radiative Transfer*, doi:10.1016/j.jqsrt.2015.09.002, 2015.4.

4. Atmospheric Remote Sensing – Applications

4.1 Bromine Oxide in the Polar Atmosphere

M. Begoin, N. Hao, P. Valks, D. Loyola

Ozone depletion events (ODE) in the Arctic and Antarctica boundary layer are a well-known phenomenon in polar springtime (*Simpson et al. 2007*). During these events, tropospheric ozone can nearly completely and very rapidly vanish from the atmosphere over a wide area. First reported in the 1980s in the Arctic and later also in Antarctica, ODEs turned out as a recurring episode with a seasonal cycle.

The ozone loss could be linked to the occurrence of halogens in the lower atmosphere and here bromine has been identified as the key halogen species. During an auto-catalytic heterogeneous reaction process, bromine molecules are released from sea salt to the gas phase and photochemically cleaved into bromine radicals (Br), which are then destroying ground-level ozone. Needing low temperatures and sufficient sunlight, this reaction cycle only occurs in polar springtime. As this process is leading to an exponential increase of bromine radicals (Br, BrO) in the atmosphere, it is also known as “bromine explosion”. These highly reactive bromine radicals can also play an important role in the deposition of gaseous elemental mercury from the atmosphere to the sensitive polar environment.

BrO is a halogen radical that can be measured by space-borne remote sensing means, e.g. by the Global Ozone Monitoring Experiment 2 (GOME-2) instruments on-board the EUMETSAT satellites MetOp-A and MetOp-B using Differential Optical Absorption Spectroscopy (DOAS). Monthly BrO maps of Antarctica and the Arctic are showing a clear seasonal BrO cycle and a strong correlation between sea-ice covered areas and enhanced BrO values (Fig. 4-1). Directly above Antarctica and its surrounding ice shelves as well as over Greenland, no BrO is observed in monthly means. This is due to the fact that sea salt is not abundant in ice formed from snow, i.e. fresh water. Nevertheless, BrO can be transported over long distances during episodes with high wind speeds (*Jones et al. 2009*) and therefore can also appear over land-based ice. Such long-range transport events can also point to potential source regions of bromine release (*Begoin et al. 2010*). Although the release mechanism of bromine via auto-catalytic heterogeneous reactions is fully understood, the exact sources are still open to some debate. As BrO observations are clearly associated with sea ice covered regions and saline surfaces, several substrates could serve as source for atomic bromine, like sea salt aerosols, fresh sea ice surfaces, sea salt enriched snow or “frost flowers” growing on newly forming sea ice.

Due to climate change, sea ice is subject to large variations. New records in minimum sea ice coverage, especially in the Arctic, result in enhanced first year sea ice and open leads in polar regions, which may have consequences for bromine release and therefore ozone depletion in the polar boundary layer. The GOME-2 instruments on MetOp-A and MetOp-B are excellent tools for observing the long-term trend in polar BrO concentrations. The time series started by GOME-2 on MetOp-A and MetOp-B will continue. Their availability well into the future will be insured with the launch of MetOp-C in 2018.

References

Begoin, M., A. Richter, A. Weber, M. Kaleschke, L. Tian-Kunze, X. Stohl, A. Theys, N. and Burrows, J.P.: Satellite observations of long range transport of a large BrO plume in the Arctic. *Atmospheric Chemistry and Physics*, 10, 6515-6526, 2010.

Jones, A.E., Anderson, P.S., Begoin, et al.: BrO, blizzards, and drivers of polar tropospheric ozone depletion events. *Atmospheric Chemistry and Physics*, 9, 4639-4652, 2009.

Simpson W.R., von Glasow, R., Riedel, K., et al.: Halogens and polar boundary-layer ozone depletion. *Atmospheric Chemistry and Physics*, 7, 4375-4418, 2007.

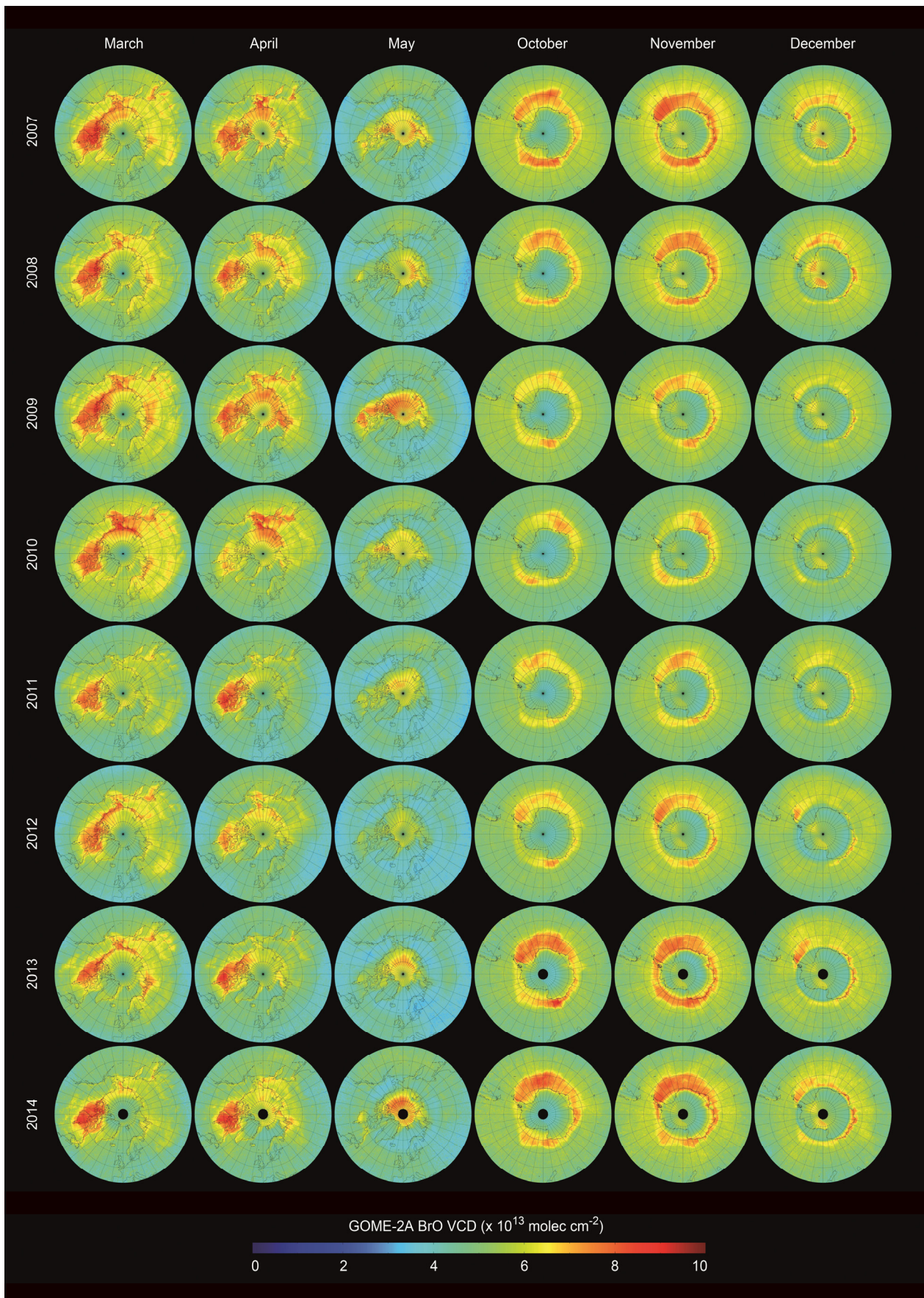


Fig. 4-1: Monthly vertical column densities of polar BrO in the Arctic (March-April-May) and Antarctic (October-November-December) for the years 2007-2014 as seen from GOME-2A.

4.2 GOME-2 Volcanic SO₂ Retrieval

P. Hedelt, D. Efremenko

In 2015 we continued the regular monitoring of SO₂ plumes as an indicator for volcanic activity. Several eruptions could be detected using GOME-2 on MetOp-A and MetOp-B.

One of the most interesting occurred at the end of 2015 when Mt. Etna displayed paroxysms. They are considered to be the strongest of the last 20 years. Paroxysms describe a series of eruptions which are characterized by frequent explosions, becoming more and more intense until they come to an end in a final violent eruption. In the morning of 3 December 2015 the paroxysms started at the *Voragine* crater of the Etna. After this first paroxysm, a second and third climax occurred in the morning (9:00 – 10:00 h UTC) and evening of the following day (20:30 – 21:15 h UTC). A fourth paroxysm happened in the afternoon of 5 December. SO₂ emissions of more than 20 DU were detected by GOME-2, showing that the SO₂ plume from the first paroxysm was transported eastwards (left panel of Fig. 4-2) and was even detectable over Japan and the Pacific Ocean five days after the event. The SO₂ plume of the morning eruption on 4 December was transported south-east, whereas the SO₂ plume from the afternoon eruption was transported south-west. The two plumes from the 5/6 December paroxysms were transported northwards. They arrived over southern Germany in the evening of December 7th and morning of December 8th, respectively, where they could be detected in-situ at the meteorological observatory Schneefernerhaus near the summit of the Zugspitze in the Bavarian Alps.

The SO₂ plume was studied with our novel algorithm called “Inverse Learning Machine (ILM)”. It permits an extremely fast and accurate retrieval of the SO₂ plume height. ILM produces a mapping between the spectral radiance and the geophysical parameters of interest using supervised learning methods. The ILM combines smart sampling methods, dimensionality reduction techniques and various linear and non-linear regression analysis schemes based on principal component analysis and neural networks. The exact location and height of the volcanic SO₂ plume is essential for accurate determination of the SO₂ emitted by volcanic eruptions and their forecast modelling for applications in aviation control.

The retrieved plume height for the Mt. Etna eruptions is in the range from 8 to 10 km (right panel of Fig. 4-2), which is in agreement with ash cloud heights determined from satellite images of MODIS (NASA/Terra and Aqua) and with measurements of SEVIRI (EUMETSAT/MSG) and CALIOP (NASA/CALIPSO).

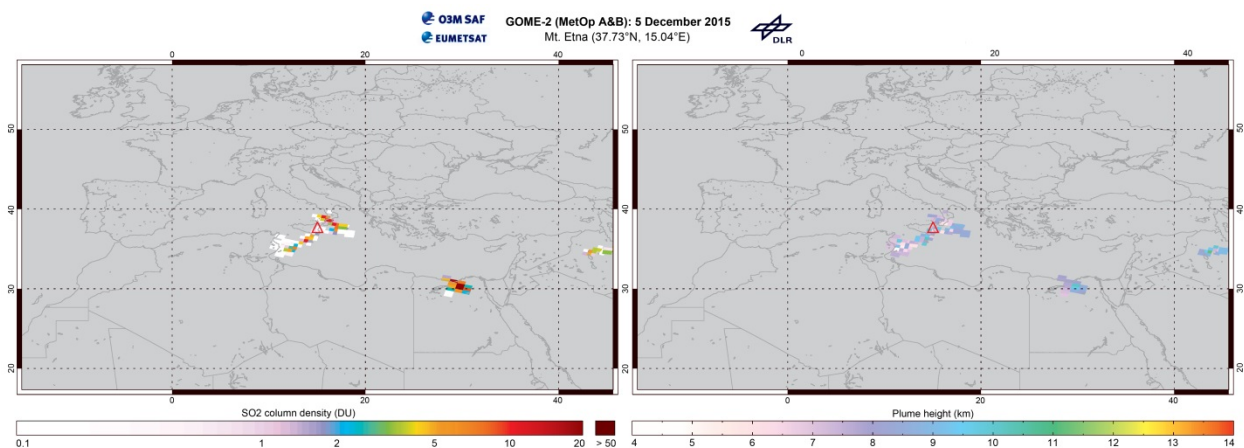


Fig. 4-2: Left: GOME-2A and GOME-2B measurement of the SO₂ plume from the Mt. Etna eruptions detected on 5 December 2015 (left) and retrieved plume height (right). The SO₂ cloud in the eastern part of the map originates from the paroxysm on 3 December, the plume south-east of Etna from the morning eruption of 4 December and the SO₂ signal close to Etna from the afternoon paroxysm of 4 December. Note that the overpass time of GOME-2 is in the morning at 9:30h UTC local time, which means that the eruption on 5 December did not yet occur at the time of the measurement.

Furthermore two volcanoes erupted in South America which had been inactive for more than three decades. On 22 April 2015 Calbuco in Chile erupted after 42 years of inactivity with strong emissions of ash. During the eruption the local population inside a 20 km exclusion zone was evacuated and international flights in and out of several major cities were delayed or canceled. The SO₂ plume could be

detected by GOME-2 on 23 April. It was observed for almost one month, showing its transport over the Atlantic Ocean towards Australia (left panel of Fig. 4-3). The retrieved plume height was in the range between 7 and 9 km (right panel of Fig. 4-3).

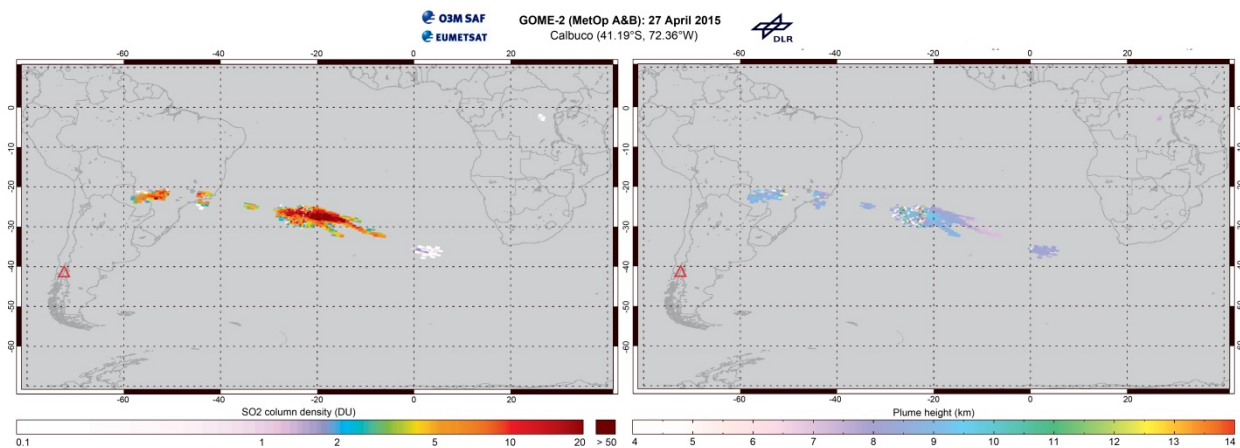


Figure 4-3: Left: GOME-2A and GOME-2B measurement of Calbuco's SO₂ plume detected on 27 April 2015 (left) and retrieved plume height (right).

On May 25, 2015 Wolf, situated on Isabela Island in the Galapagos archipelago, erupted after 33 years of inactivity. Due to the volcano's remote location neither local population nor endemic fauna was endangered. GOME-2 detected the SO₂ emissions for more than a one month until end of June (left panel of Fig. 4-4 one day after the initial eruption). The plume height retrieved by the new algorithm was in the range from 8 to 10km (right panel of Fig. 4-4).

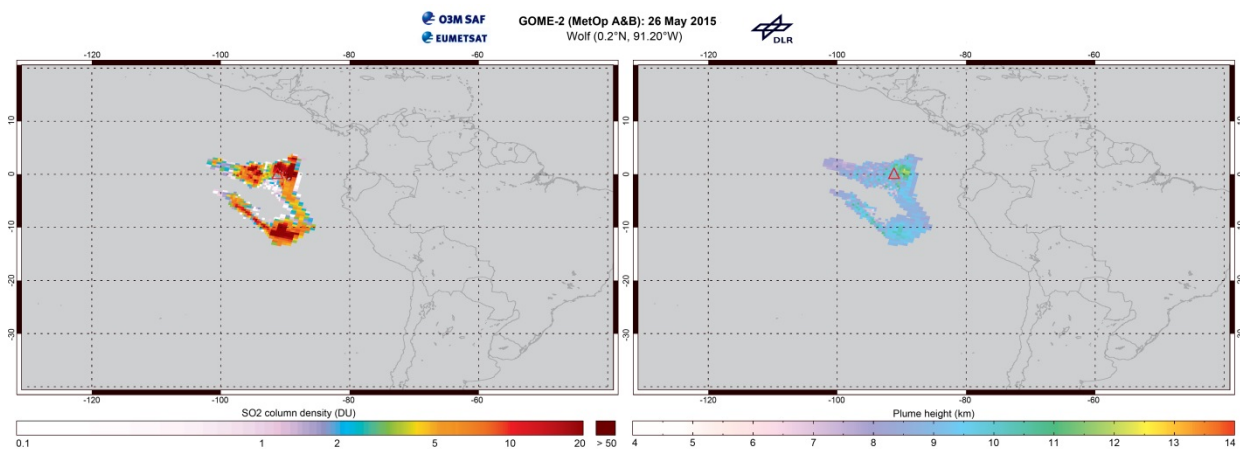


Fig. 4-4: Left: GOME-2A and GOME-2B measurement of Wolf's SO₂ emissions detected on 26 May 2015 (left) and retrieved plume height (right).

Besides its effects on local air quality and aviation safety, volcanic SO₂ may also impact the global climate. When released into the atmosphere, it is subject to wet and dry decomposition as well as oxidization to sulfate aerosols. In the lower troposphere SO₂ and sulfate aerosols only have a lifetime of a few days. However, when injected into the stratosphere during very strong eruptions its lifetime may reach several weeks, whereas sulfate aerosols can remain for over a year affecting Earth's radiative forcing by reflecting the solar irradiation and by changing the albedo and lifetime of clouds.

4.3 Modeling Air Pollution in Beijing: Emission Reduction versus Meteorological Influence

E. Risse, N. Hao, T. Trautmann

This case study used the Chemical Transport Model WRF-Chem to simulate and measure the efficiency of temporal large-scale emission reductions under different meteorological conditions. The November 2014 Asian Pacific Economic Cooperation (APEC) summit provides a unique opportunity for this study due to the extraordinarily good and well-measured air quality which is believed to be induced by intense emission-reduction measures implemented in China. Four cases had been simulated (see Table 4-1) to inter-compare between favorable and unfavorable meteorological conditions (in terms of air quality) as well as reduced and non-reduced emissions. Key variables of the simulation results were evaluated against AERONET measurements of Aerosol Optical Depth (AOD) and air quality measurements by the Chinese Ministry of Environment (CME). The inter-comparison was then performed on time- and volume-averaged total concentrations of the key variables nitrogenous oxide (NO_x) and particulate matter (PM_{2.5} and PM₁₀).

Model and Simulation Parameters	
Domain	China + surrounding (120 × 100 grid-points)
Grid size	30 × 30 km, 34 fixed pressure height levels
Timestep	90 s
Chemistry solver	CBMZ (Carbon-Bond Mechanism version Z)
Aerosol module	MOSAIC (Model for Simulating Aerosol Interactions and Chemistry)
Initial & boundary conditions (meteorological); also used for FDDA (Four Dimensional Data Assimilation)	NCEP FNL Reanalysis (Global Tropospheric Model)
Initial conditions (chemical)	MOZART (Model for Ozone and Related Chemical Tracers); Species mapped to match CBMZ bins
Emission dataset (anthropogenic)	MEIC (Multiresolution Emissions Inventory for China) 2010; Lumped to 5 sectors
Emission dataset (biogenic)	WRF-Chem Default
Emission reduction approach	50% Overall reduction over every emission sector for whole simulation period; Inside latitude/longitude rectangle around Beijing: 113°E-119°E, 36°N-42°N
Number of variables	> 350, ~50 for meteorology, ~300 for chemistry
Simulated time	3-16 November 2014 (APEC period) 3-16 November 2011 (comparison period)
Computational Performance	
Number of processors used	64
Calculation time for one time-step	5-7 s
Calculation time for one simulated day	3-4 h
Output data amount	~6 GB/d -> ~90 GB for 14 days simulation
Output step	Hourly output
Evaluation Approach	
Evaluated time (considering spin-up-time)	10-16 November for both 2011 and 2014
Evaluated measurements	5 AERONET stations (quality controlled by NASA) 13 Chinese Ministry of Environment stations (only 2014)
Measurement evaluation approach	Cross-correlation of varying simulation grid-points with all stations for PM _{2.5} , PM ₁₀ (CME), AOD (AERONET)
Comparison between simulations	Comparison of temporally and spatially averaged concentrations of NO ₂ , PM ₁₀ , PM _{2.5} , SO ₂ , O ₃

Table 4-1: Model properties and simulation settings.

Fig. 4-5 shows two examples of point-to-point comparisons between simulated variables and the corresponding real physical measurements. Depicted are timelines from model grid-points that display the highest correlations to measurements of one certain measurement-station for the reference period. It is obvious that the simulation is able to reproduce the overall course of events quite well, but are partially influenced by a phase-delay of several hours, as visible in the right panel. The phase-delay can for most stations be drastically reduced by choosing a nearby grid-point up- or downstream the dominating horizontal wind-speed as performed in the left panel.

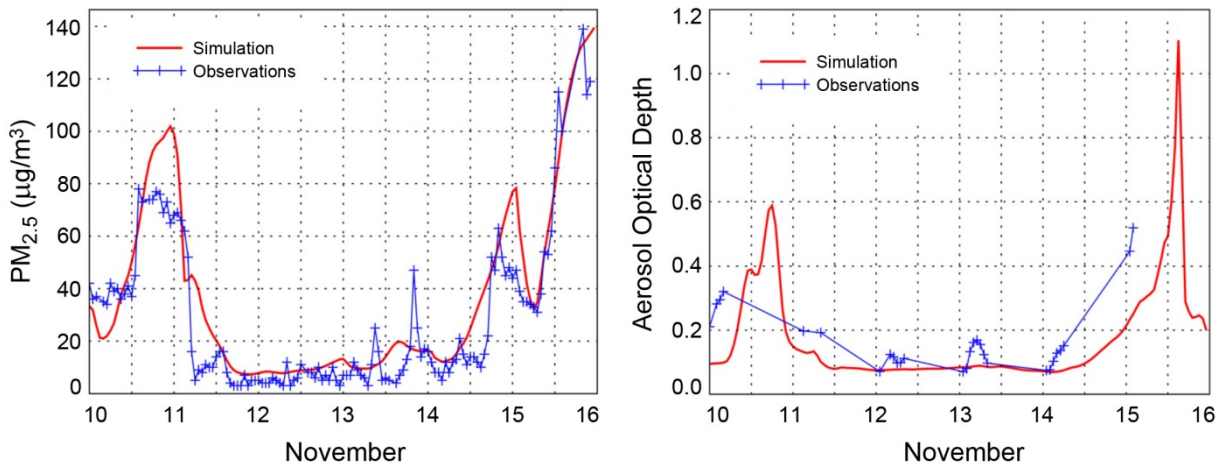


Fig. 4-5: Timelines of simulated values against measurements. Left: PM_{2.5} density measured 2014 by CME Beijing DingLou station against reduced emission simulated values at ground level for a grid-point located 120 km south-west of the station, correlation coefficient $R=0.93$. Right: Aerosol Optical Depth measured 2014 by AERONET Beijing station against simulated values at the matching grid-point, correlation coefficient $R=0.88$.

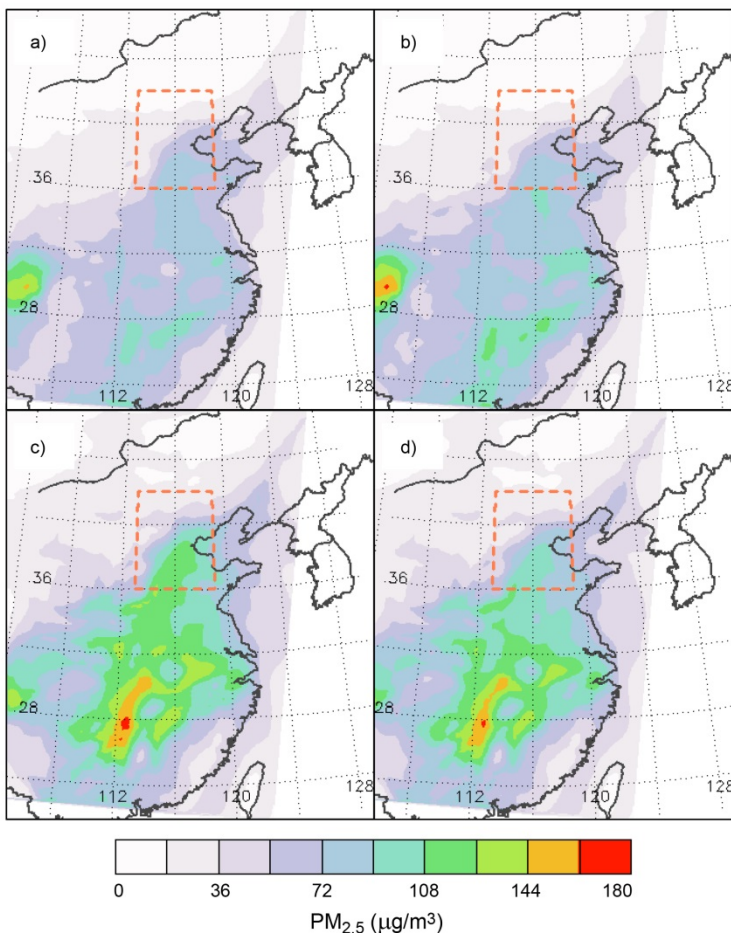


Fig. 4-6: Timely and height-averaged simulated PM_{2.5} densities from 10-15 November from ground level to ~830 m above ground. The dashed area marks the area of manipulated emissions. a): 2014 original emissions, b): 2014 reduced emissions, c): 2011 original emissions, d): 2011 reduced emissions.

Fig. 4-6 illustrates the differences in air-quality between different simulation runs. The most obvious decrease occurs between c) and d) inside the emission-reduced area, while no obvious change is visible from a) to b) in the same area. Outside the emission-reduced area, an increase in PM_{2.5} density can be noted from a) to b) and a decrease from d) to c). While the latter can be partially explained through the emission reductions in proximity to the reduced area, the former is quite contra intuitive. This divergence is most probably due to an accumulation of random perturbations in the chemistry rather than any systematic meteorological effect, since FDDA ensures that the key variables remain close to the boundary conditions. This effect decreases the

significance of the results and could better be resolved through an ensemble case study with more simulations for each case.

Studies of all time averages from 10-15 November of several species' concentrations in the Beijing area that are shown in Table 4-2 lead to the conclusion that emission reduction is much more efficient under conditions that favor high pollution, like in November 2011. Unfortunately the results are flawed by random perturbations which in this case tend to amplify this effect. However, considering the order of magnitude of an increase of 27.5% in average (over the Beijing area) PM_{2.5} concentration, this effect remains still significant.

	Beijing Area (90 km radius), ground level only	Beijing Area (90 km radius), ground to 830 m	Whole domain, ground level only	Whole domain, ground to 830 m
2014 reduced	38.41	30.76	35.37	30.73
2014 original	40.07 (+4.3%)	32.22 (+4.7%)	32.36 (-8.5%)	28.19 (-8.3%)
2011 reduced	60.99	47.95	41.81	35.60
2011 original	75.51 (+23.8%)	61.16 (+27.5%)	44.06 (+5.4%)	37.51 (+5.3%)

Table 4-2: Comparison of time and spatial average densities of PM_{2.5} for the whole domain and Beijing area (all values in $\mu\text{g}/\text{m}^3$).

The dominating factor that rules the development of bad air quality in this case is wind speed and direction. Fig. 4-7 shows the streamlines of average wind speeds in the reference period for the 2014 and 2011 cases. The overall wind direction in the left panel is from north-west-west where the density of emissions declines quickly with distance, while the dominating direction in the right panel is rather from south-west-west with a slight decrease in speed. It is known from other case studies that low winds from south-east carry heavily polluted air masses from the emission-intense industrial areas of the provinces Hebei and Shandong to Beijing. Those are the main reason for poor air quality, more significant than even the emissions from Beijing's own industrial areas in the south.

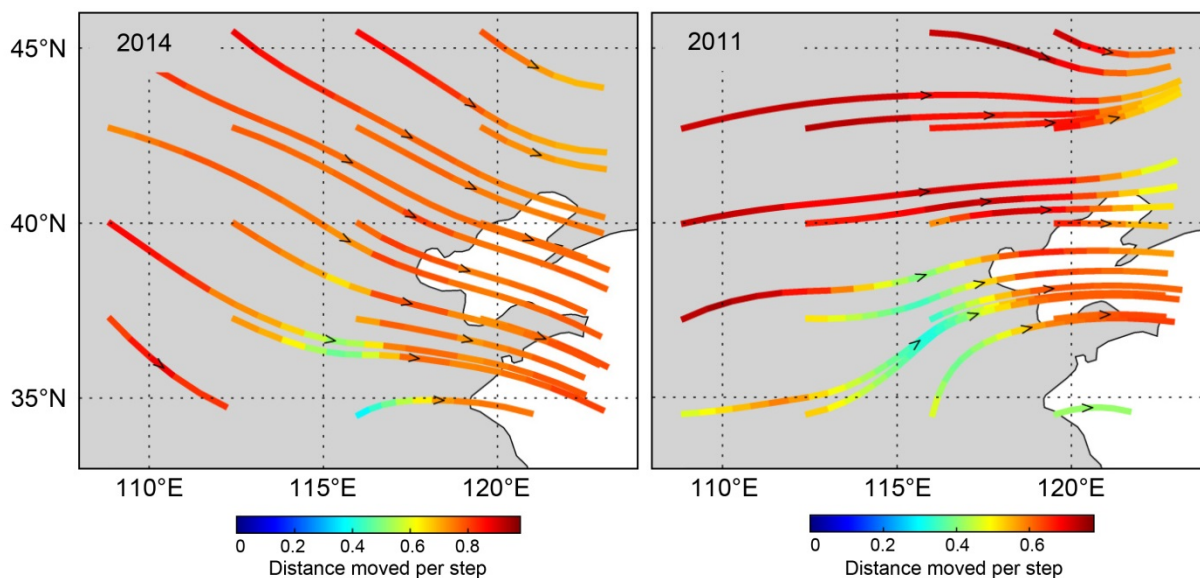


Fig. 4-7: Streamlines of time-averaged winds from 10-15 November from ground level to 830m. Left panel 2014, right panel 2011.

The result of this study, i.e. the increasing efficiency of emission-reduction with lower wind speeds and directions from south-west can be explained by considering the particle-equilibrium: Given a fixed lifetime, the average distance above ground of one particle increases proportionally to the wind speed. The total concentration of particles at one point depends on all the emission sources upstream that are located inside one "way of life" of the particles. If emissions are reduced in a certain area upstream for

a certain percentage, the impact depends on which percentage of the “way of life” is covered by this area. If winds are strong and the “way of life” is long, the percentage will be lower and therefore affecting the total concentration less than with low winds and a short “way of life”.

4.4 The ESA-CCI GOME-type Total Ozone Essential Climate Variable

M. Coldewey-Egbers, D. Loyola

In the past year we continued our work related to the GOME-type Total Ozone Essential Climate Variable (GTO-ECV) data record which has been created within the framework of the European Space Agency's Climate Change Initiative (ESA-CCI). Total ozone column observations from GOME (Global Ozone Monitoring Experiment), SCIAMACHY (SCanning Imaging Absorption SpectroMeter for Atmospheric CHartography), and GOME-2A have been combined into one homogeneous time series, thereby taking advantage of the high inter-sensor consistency which has been achieved through the application of the common retrieval algorithm GODFIT version 3. The data record spans the 15-year period from March 1996 to June 2011. It contains global monthly mean total ozone columns on a $1^\circ \times 1^\circ$ grid. Geophysical ground-based validation using Brewer, Dobson, and UV-visible instruments has shown an excellent agreement and long-term stability for almost all latitudes apart from a few outliers which are mostly due to spatial and temporal sampling issues. A detailed description of the creation of the data record and presentation of the validation results can be found in *Coldewey-Egbers et al. (2015)*.

Level 3 algorithm and merging approach

The level 3 algorithm is designed to map the level 2 measurements, processed with the GODFIT_V3 retrieval algorithm (*Lerot et al. 2014*), onto a daily fixed global grid of $1^\circ \times 1^\circ$. Each grid cell contains an average of all level 2 data from the same day overlapping with the level 3 cell. Cell values are computed as weighted averages with the fractional area of overlap of the satellite ground pixel with the given grid cell used as weight. The gridding algorithm is applied separately to GOME, SCIAMACHY, and GOME-2A measurements.

The next step is to merge the individual level 3 data sets from the three sensors into one homogeneous record using an inter-instrument calibration approach. We apply an external adjustment to SCIAMACHY and GOME-2A results with respect to the GOME results in order to account for inter-sensor differences, which possibly remain from the level 2 algorithm. The calculation of the correction factors is based on a comparison of 1° zonal monthly means. The correction factors comprise two parts:

- a “basic” correction for each month of the year in terms of low-order polynomials as a function of latitude, and
- an offset for each individual month, which is added to the “basic” correction. This offset does not depend on latitude, but it accounts for the time-dependence, i.e. short-term fluctuations, in the differences.

The correction factors are then applied to the SCIAMACHY and GOME-2A daily gridded data. Once SCIAMACHY and GOME-2A data have been adjusted, $1^\circ \times 1^\circ$ monthly mean data are computed for each instrument thereby taking into account that a sufficient number of measurements equally distributed over time is available. Subsequently, the three data sets are combined into one single record as follows: Only one instrument is used at a time, i.e. the merged GTO-ECV total ozone time series contains GOME measurements from March 1996 to March 2003, adjusted SCIAMACHY measurements from April 2003 to March 2007, and adjusted GOME-2A measurements from April 2007 to June 2011. The complete data record with typical total ozone features is shown in Fig. 4-8. Highest ozone values occur in northern hemispheric springtime, whereas monthly mean values are below 200 DU from September to November south of 70° S. Extreme events such as the anomalous Antarctic ozone hole in 2002 and the severe ozone loss in 1997 and 2011 in the Arctic are visible.

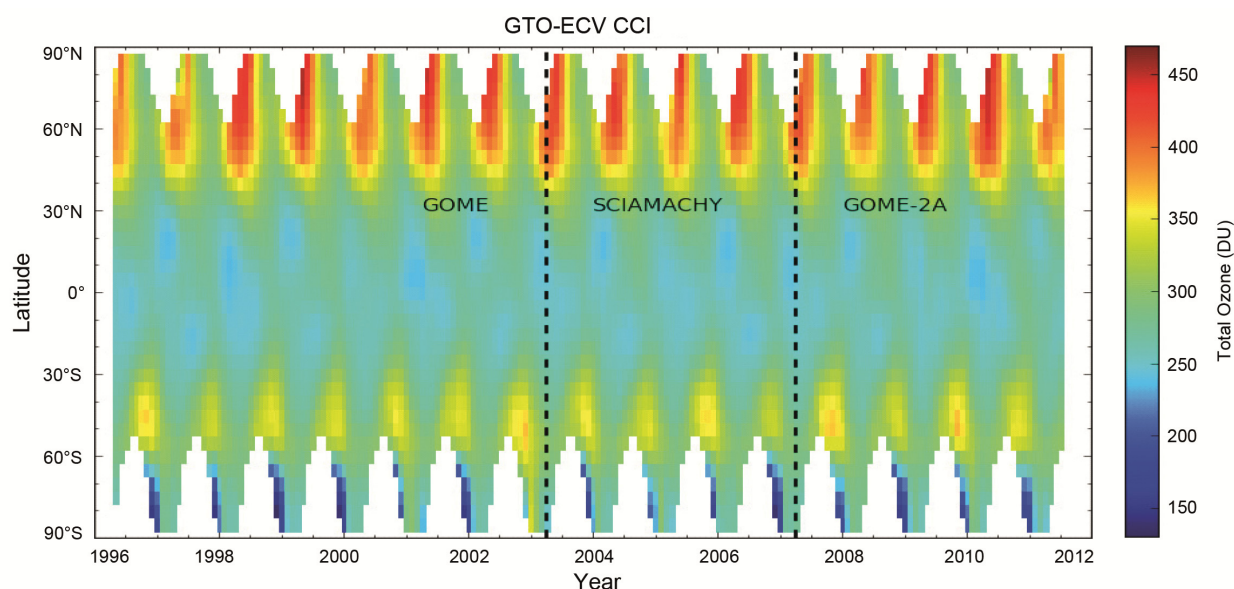


Fig. 4-8: GTO-ECV CCI total ozone column data record 1996-2011 as a function of latitude. Vertical black dashed lines indicate the change-over from GOME to SCIAMACHY in April 2003 and from SCIAMACHY to GOME-2A in April 2007.

Summary of geophysical validation results

The validation of level 2 satellite total ozone columns using independent ground-based observations has been a substantial part of retrieval algorithm development for many decades. Taking into account that the long-term climate study of the ozone content is based on using level 3 gridded products, one must ensure that the transition from level 2 to level 3 does not introduce artifacts. These might be induced by the level 3 algorithm through sampling issues or by the merging approach through improper adjustment.

In conclusion, the GTO-ECV CCI level 3 validation results were found to be very consistent with the separate GOME, SCIAMACHY, and GOME-2A level 2 validation comparisons (*Koukouli et al. 2015*). In particular, on a monthly mean basis, for the Dobson comparisons, both the northern and southern hemisphere time series are in very close agreement. Similarly, for the Brewer comparisons (northern hemisphere), an excellent agreement is found apart from a handful of outliers. On a seasonal basis, both the Brewer and the Dobson level 3 comparisons show close agreement to the level 2 comparisons.

The mean bias and standard deviation is $1.00 \pm 0.75\%$ for the Dobson comparison and $0.16 \pm 0.66\%$ for the Brewer comparison, respectively. The decadal drift and drift error calculated from the Northern Hemisphere time series amounts to $-0.12 \pm 0.12\%$ and $0.17 \pm 0.11\%$, respectively. It is evident that the product easily meets the ESA-CCI user requirement levels and, hence, we conclude that the current GTO-ECV CCI level 3 total ozone product is of the same high quality as the constituent level 2 total ozone products.

Outlook

Our study demonstrates that the current GTO-ECV CCI data record is suitable for a variety of applications. In particular it is useful for the long-term monitoring of the past evolution of the ozone layer (e.g., *Weber et al. 2015*; *WMO 2014*). Due to its excellent decadal stability – the relative drift compared to the ground-based reference is less than 1% per decade – it is valuable for long-term trend analysis of the ozone field. The high spatial resolution of the data record enables us to investigate ozone changes on global as well as regional scales as recently demonstrated by *Coldewey-Egbers et al. (2014)*. Furthermore, global long-term data records such as GTO-ECV CCI can be compared with Chemistry-Climate Model simulations in order to evaluate these model projections and to calibrate the efficiency of the models' systems.

The second phase of ESA-CCI is dedicated to a reduction of sampling errors using spatio-temporal statistical tools and an extension of the GTO-ECV data record. GOME-2 on MetOp-B was launched in September 2012 and the data will be included in the new version. In addition measurements performed with the Ozone Monitoring Instrument (OMI) onboard the NASA Aura satellite (2004 to present) and

data from the Ozone Mapping and Profiler Suite (OMPS) onboard the NASA Suomi National Polar-orbiting Partnership satellite (2011 to present) will be included. Thereby we can take advantage of OMI's excellent long-term stability over the ten plus years of operation. The GOME-2 on MetOp-C is planned to be launched in 2018, and together with the Sentinel-5 precursor (to be launched in 2016) and the Sentinel-4 and Sentinel-5 sensors (to be launched by the end of this decade), these future instruments will contribute to the extension of this reference data set.

References

Coldewey-Egbers, M., Loyola, D., Braesicke, P., Dameris, M., Van Roozendael, M., Lerot, C. and Zimmer, W.: A new health check of the ozone layer at global and regional scales. *Geophysical Research Letters*, 41, 4363-4372, doi:10.1002/2014GL060212, 2014.

Coldewey-Egbers, M., Loyola, D., Koukoulis, M., Balis, D., Lambert, J.-C., Verhoelst, T., Granville, J., Van Roozendael, M., Lerot, C., Spurr, R., Frith, S.M. and Zehner, C.: The GOME-type Total Ozone Essential Climate Variable (GTO-ECV) data record from the ESA Climate Change Initiative. *Atmospheric Measurement Techniques*, 8, 3923-3940, doi:10.5194/amt-8-3923-2015, 2015.

Koukoulis, M.E., Lerot, C., Lambert, J.-C., Goutail, F., Granville, J., Pommereau, J.-P., Balis, D., Zyrichidou, I., Van Roozendael, M., Labow, G., Frith, S.M., Loyola, D., Coldewey-Egbers, M., Spurr, R. and Zehner, C.: Evaluating a new homogeneous total ozone climate data record from GOME/ERS-2, SCIAMACHY/Envisat and GOME-2/MetOp-A. *Journal of Geophysical Research*, 120, 12296-12312, doi:10.1002/2015JD023699, 2015.

Lerot, C., Van Roozendael, M., Spurr, R., Loyola, D., Coldewey-Egbers, M., Kochenova, S., van Gent, J., Koukoulis, M., Balis, D., Lambert, J.-C., Granville, J. and Zehner, C.: Homogenized total ozone data records from the European sensors GOME / ERS-2, SCIAMACHY / Envisat and GOME-2 / MetOp-A. *Journal of Geophysical Research*, 119, 3, 1639-1662, doi:10.1002/2013JD020831, 2014.

Weber, M., Steinbrecht, W., Roth, C., Coldewey-Egbers, M., van der A, R., Degenstein, D., Fioletov, V., Frith, S., Froidevaux, L., Long, C., Loyola, D. and Wild, J.: Stratospheric Ozone. In: *State of the Climate in 2014*. *Bulletin American Meteorological Society*, 96, 7, S44-S46, 2015.

WMO: Scientific Assessment of Ozone Depletion: 2014. WMO Global Ozone Research and Monitoring Project – Report No. 55, Geneva, Switzerland, 2014.

4.5 Analysis of MAX-DOAS measurements at UFS

Z. Wang, N. Hao, A. Doicu

The UFS (Umweltforschungsstation Schneefernerhaus), located directly below the summit of Germany's highest mountain Zugspitze (2962 m), is a rare observation site in Germany with mostly clean and unpolluted air. It is ideal for measurements of both stratospheric composition and trace gases in the free-troposphere. Thus detecting pollution events in the free-troposphere, an indicator for short- or long-range transport of air pollutants, can be achieved.

The MAX-DOAS (Multi-AXis Differential Optical Absorption Spectroscopy) instrument at the UFS has been in operation since February 2011 (see also annual report 2009). The telescope is located on the terrace of UFS, facing toward the south. It is driven by a step motor and can scan in vertical direction. The elevation angle can vary between -10° and 90° . During the daytime, the telescope sequentially scans 8 different elevation angles: 30° , 20° , 10° , 5° , 2° , 1° , -2° (2° downwards) and 90° (zenith). Each scanning cycle takes about 10 minutes. Through a special optical fiber with one entrance and two exits, the light collected by the telescope is divided into two beams and transmitted into two spectrometers, one for the UV (320-478 nm) region, and the other for the VIS (427-649 nm) region. Both of the two spectrometers consist of single-dimensional photodetectors with 2040 pixels. The spectra measured by the two spectrometers are recorded synchronously.

Measurement of the vertical profiles of tropospheric aerosol and trace gases

With the zenith spectrum of each scanning cycle used as the reference spectrum, the DSCDs (Differential Slant Column Densities) of the oxygen dimer O_4 , nitrogen dioxide (NO_2), formaldehyde (HCHO) and nitrous acid (HONO) are calculated from the non-zenith spectra, using the DOAS method. Fig. 4-9 shows the DSCD results of 3 July 2014.

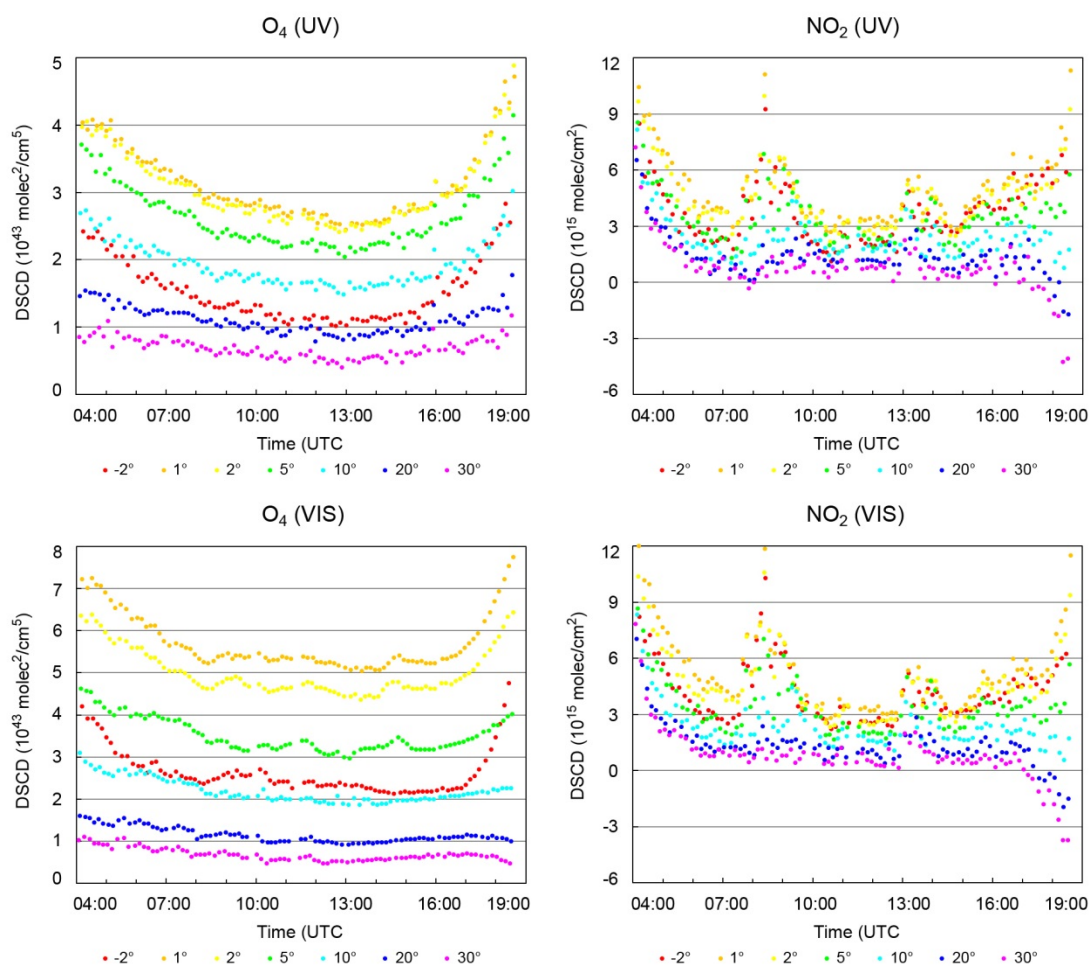


Fig. 4-9: DSCD results (O_4/NO_2 , UV/VIS) of 3 July 2014.

Afterwards, the vertical profiles of aerosol are retrieved from the DSCDs of O_4 , using the bePRO profiling tool developed at BIRA-IASB (Royal Belgian Institute for Space Aeronomy). It is based on the optimal estimation method and includes the LIDORT radiative transfer model as a forward model. Fig. 4-10 shows the aerosol profiles (VIS band) on 3 July 2014.

The vertical profiles of trace gases such as NO_2 , HCHO and HONO are retrieved from the obtained aerosol profiles and the DSCDs of the trace gases. This retrieval is also performed with the bePRO s/w package. Fig. 4-11 shows the NO_2 profiles (VIS band) on 3 July 2014.

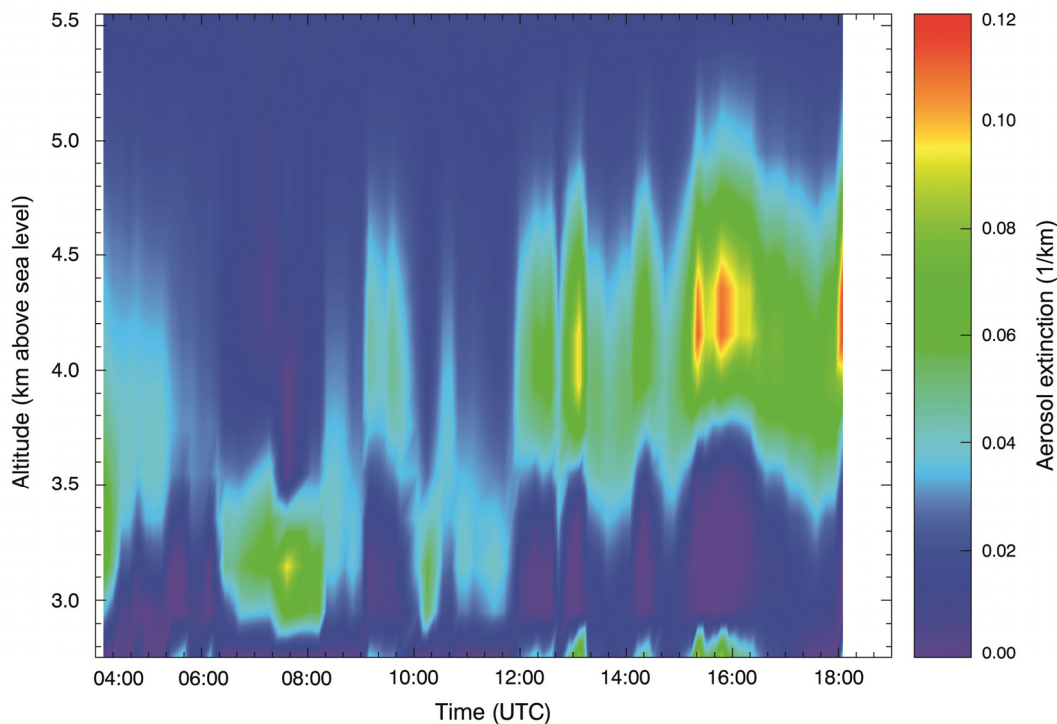


Fig. 4-10: Aerosol vertical profiles on 3 July 2014 (VIS).

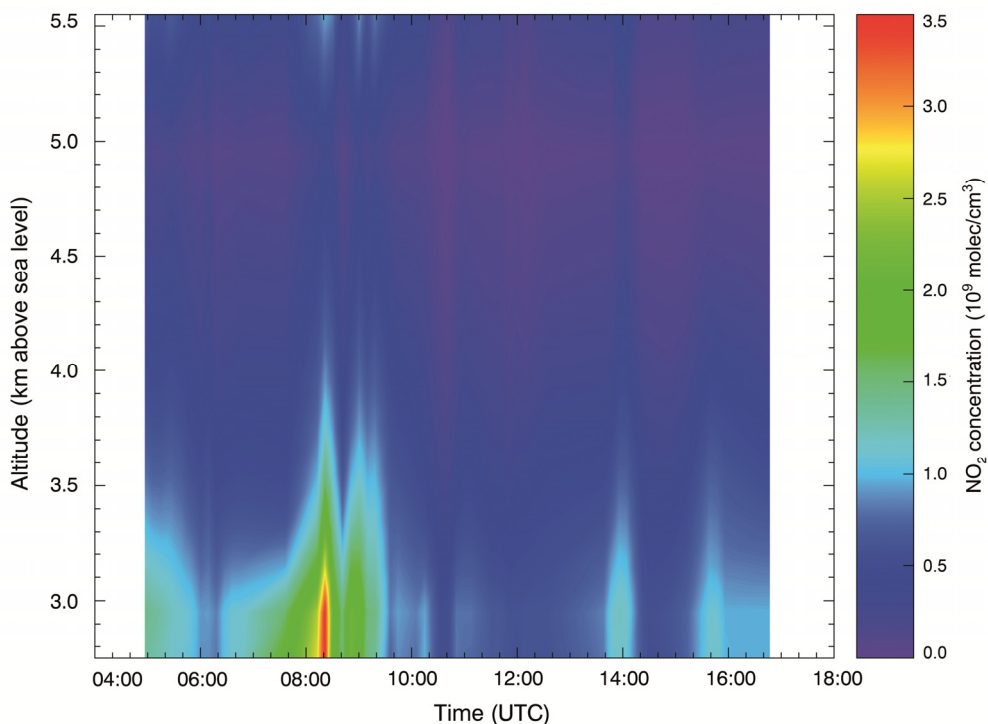


Fig. 4-11: NO_2 vertical profiles on 3 July 2014 (VIS).

Measurement of the total vertical column densities of trace gases

The Slant Column Densities (SCDs) of O_3 and NO_2 are calculated from the zenith spectra measured during twilight hours, with a fixed zenith spectrum measured on the noon of a summer day used as the reference spectrum. As the light path at noon is much shorter than that during twilight hours, the trace gas absorption in the reference spectrum can be neglected.

The Air Mass Factors (AMFs) of O_3 and NO_2 are obtained from a look-up table developed at BIRA-IASB. The AMF data in the look-up table are calculated using the UVSPEC/DISORT radiative transfer (RT) model which includes a treatment of the multiple scattering in a pseudo-spherical geometry. The Vertical Column Densities (VCDs) of O_3 and NO_2 can then be derived by dividing the SCDs by the corresponding AMFs.

Fig. 4-12 shows the total VCDs of O_3 and NO_2 measured in 2014. For a comparison, the results measured by the GOME-2A satellite are also plotted in Fig. 4-12. It can be seen that the total VCDs of O_3 measured by MAX-DOAS coincides well with the satellite data, and there is little difference between the morning data and the evening data. As for the total VCDs of NO_2 , the difference between MAX-DOAS and satellite results, as well as the difference between the morning data and the evening data, are bigger than those of O_3 . This might be due to the relatively high NO_2 concentration in the troposphere and the strong diurnal variation of tropospheric NO_2 concentration.

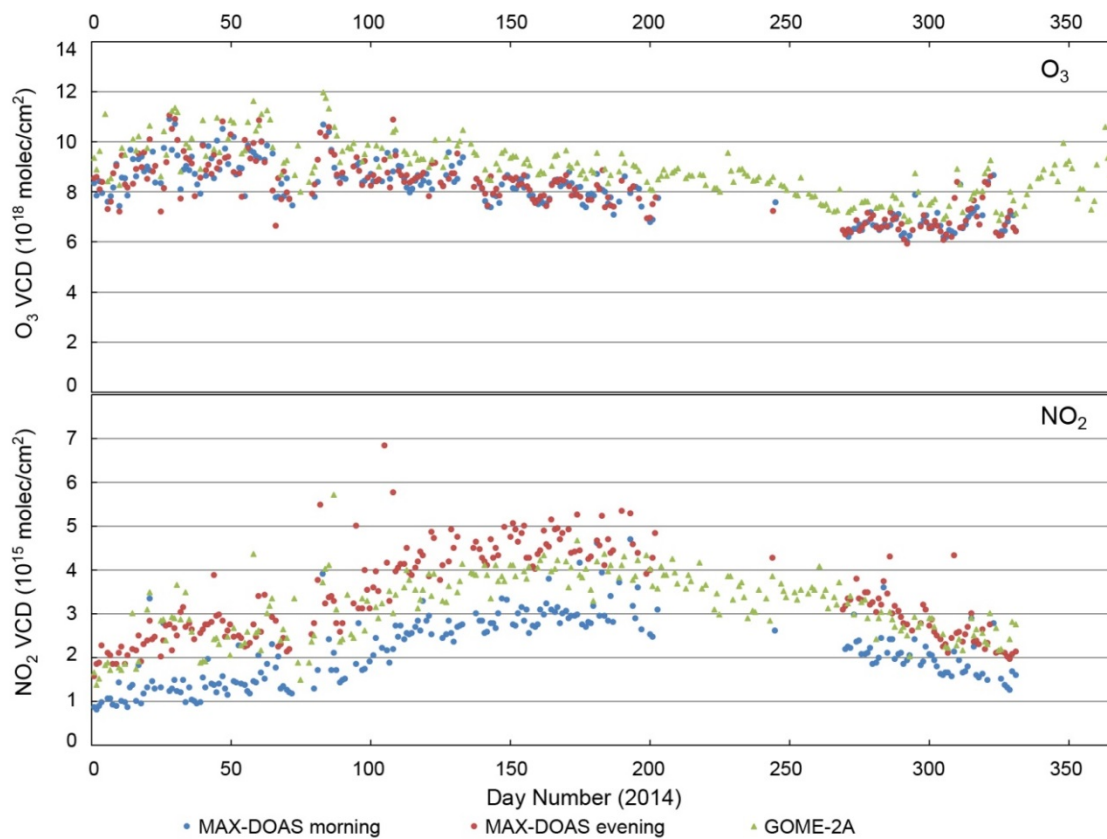


Fig. 4-12: Total VCDs of O_3 (top) and NO_2 (bottom) in 2014.

4.6 Space-borne Remote Sensing of the Polar Atmosphere

M. Gottwald, D. Loyola, T. Trautmann

The atmosphere above the Arctic and Antarctica is one of the most remote and inaccessible regions on Earth. Triggered by the prevailing extreme environment we find unique dynamic and chemical processes, which never occur at medium and low latitudes. However, such polar phenomena can impact our climate even on a global scale. For a long time the polar areas were a pristine realm, unaffected by our civilization. This has changed in the past decades. With the discovery of the ozone hole over Antarctica more than 30 years ago and the detection of traces of tropospheric pollution on snow and ice it became apparent that anthropogenic activities have now also reached these distant parts of the *System Earth*.

In order to understand this system on the whole, we have to study the polar atmosphere from the bottom to the top. It starts at the boundary layer with interactions between the troposphere and the cryosphere, continues in the stratosphere with its unique ozone chemistry and reaches up to the mesosphere and lower thermosphere, where solar-terrestrial interactions begin to become relevant.

Stratospheric and tropospheric trace gases

Our department is engaged threefold in this research area. Most important are investigations concerning the stratospheric ozone. This occurs now in the framework of the ESA Climate Change Initiative (CCI) but has a long history. Details can be found in previous annual reports, notably 2011 (*DLR Science Award 2011: Global Long-term Environmental Satellite Data for Climate Monitoring*), 2013 (*The Ozone CCI Project*) and 2014 (*The WMO Ozone Assessment – The Ozone Hole will Close in the Second Half of the 21st Century*).

Our current responsibilities in the payload data ground segment for GOME-2 on EUMETSAT's MetOp satellite series comprises continuous development of algorithms for trace gas retrievals and corresponding implementation in operational processors. The Satellite Application Facility on Atmospheric Composition Monitoring (AC SAF, formerly Ozone Monitoring SAF – O3M SAF) is the hosting entity for these activities. Among the retrieved trace gas species is the halogen compound bromine oxide (BrO). Plumes of enhanced BrO can regularly be observed in the Arctic, as well as in the Antarctic, shortly after the end of the polar winter (see chapter 4-1). Then, produced by inorganic emissions and the bromine explosion cycle, it initiates strong ozone depletion events in the polar boundary layer.

EO missions with polar capabilities

There exists a fundamental difference between polar research addressing cryospheric or atmospheric topics. While cryospheric themes can directly focus on the Arctic or Antarctica, i.e. the regions which contain almost the entire terrestrial ice sheets and glaciers, studies of the polar atmosphere often have to widen their scope. For example, the stratospheric chemistry leading to severe ozone depletion over the South Pole does not only require understanding what occurs in the region encased by the polar vortex but also has to address the processes at medium and low latitudes. This is the region where ozone is produced and subsequently transported to the poles. Another aspect concerns how the space-borne instruments have to be operated for successfully acquiring data over both poles. Imaging cryospheric measurements, e.g. using radar sensors, require careful acquisition planning. This has to address viewing geometries, on-board data storage capabilities and availability of ground stations for data downlink. Atmospheric sensors are different. They are operated continuously throughout the orbit. Their "polar capabilities" have been built into the instrument design, e.g. via autonomously setting appropriate measurement parameters when the platform is crossing the polar regions and low sunlight levels require certain exposure times. Imaging EO missions have to be well coordinated for yielding maximum return for a particular topic, e.g. polar science, while atmospheric spectrometric missions perform their polar "duties" as part of their continuous measurement sequences along the orbit. However, here the atmospheric data content has to be identified in and extracted from the overall data volumes.

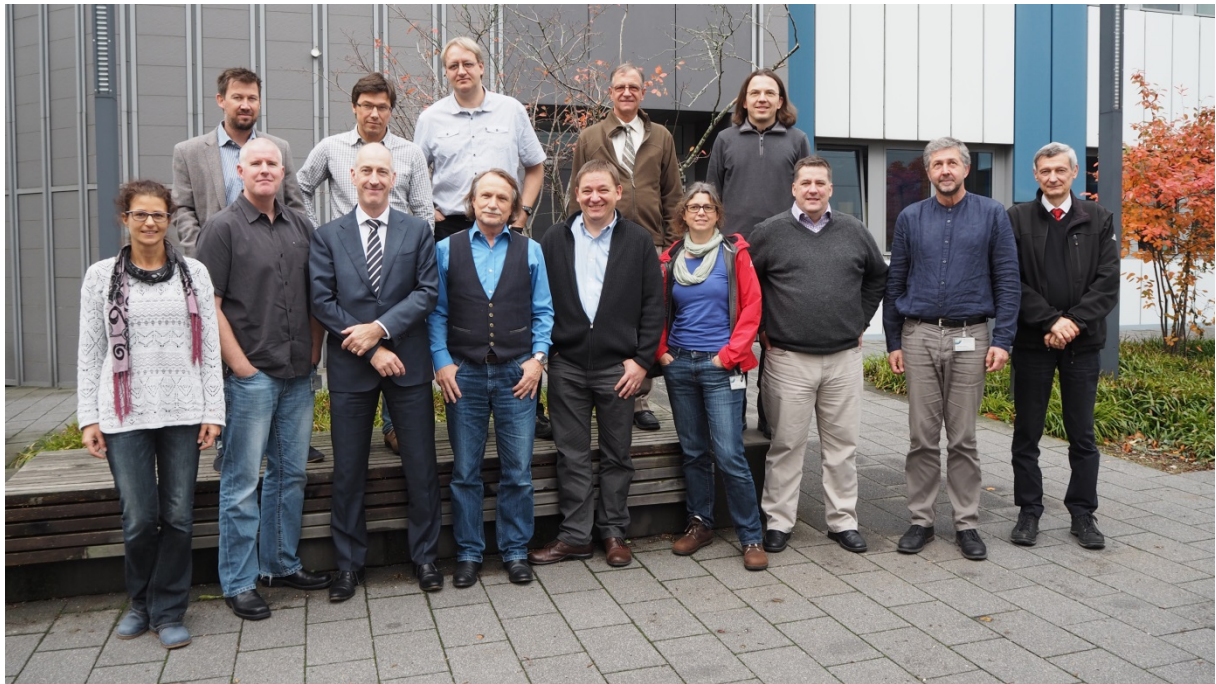


Fig. 4-13: Participants at the 2015 annual meeting of the PSTG. Front (left to right): D. Floricioiu (DLR/IMF), S. Howell (Government of Canada, Climate Processes Section), M. Drinkwater (Mission Science Division, ESA ESTEC), M. Gottwald (DLR/IMF), D. Small (Dept. Geography, University of Zurich, Switzerland), A. Bartsch (Zentralanstalt für Meteorologie und Geodynamik, Austria), Y. Crevier (Canadian Space Agency, Canada), F. Montagner (EUMETSAT Marine Applications Manager, Darmstadt), M. Ondras (WMO Observing Systems Division, Switzerland). Top (left to right): M. Zemp (Dept. Geography, University of Zurich, Switzerland), T. Nagler (ENVEO IT GmbH, Austria), F. Paul (Dept. Geography, University of Zurich, Switzerland), D. Ball (DB Geoservices Inc., Canada), B. Scheuchl (Department of Earth System Science, University of California, Irvine, USA)

Our third, and more strategically oriented polar involvement concerns the coordination of the worldwide fleet of EO missions for polar research, just in the light of the characteristics of the different types described above. In support of the International Polar Year (IPY) 2007-2008, the World Meteorological Organization (WMO) had established the Space Task Group (STG). The members of the STG had been selected from space agencies operating Earth Observation missions which could be used in support of polar research. The main STG purpose was to coordinate such missions to the maximum extent within their respective rules and to streamline data access. Because of STG's success, at the end of the IPY it was decided to continue the EO mission coordination effort, now under the group's title "Polar Space Task Group".

DLR is represented in the PSTG by two members, one coming from our department. This is particularly important since the polar atmosphere receives growing attention in the strategic goals of the PSTG. Our participation in past (GOME/ERS-2, SCIAMACHY/ENVISAT), current (GOME-2/MetOp) and future (Sentinel-5 Precursor, Sentinel-4, Sentinel-5, ADM-Aeolus and MERLIN) satellite missions will contribute significantly to missions providing polar atmospheric knowledge. At the annual PSTG-meeting, which was hosted by DLR-EOC from 5-7 October 2015 (Fig. 4-13), we could highlight our involvement in atmospheric remote sensing missions. Especially MERLIN, the DLR/CNES undertaking for developing and operating a space-borne lidar for measuring the global concentrations of the greenhouse gas methane, generated increased interest. With globally rising temperatures we expect that thawing permafrost will become a major source for this trace gas. MERLIN will not only help to better understand greenhouse effects but also how permafrost regions will develop. In the Arctic they constitute a unique ecosystem. Anthropogenically triggered global change could damage it in an irreversible manner.

4.7 Analysis of the Jacobian Matrices for the Atmospheres of Exoplanets

M. Vasquez, F. Schreier, T. Trautmann

Since the discovery of the first extrasolar planet about 20 years ago, more than 2000 exoplanets have been detected and confirmed, including some Earth-like planets in the host star's habitable zone. Meanwhile even spectra of a few exoplanets have become available. Thus, attention is now slowly shifting from mere "detection" to towards more detailed "studies" by means of remote sensing. Special emphasis has been put on investigations of possible atmospheres around exoplanets.

Whether retrieval of their state parameters, e.g. temperature and composition, from acquired spectra provides reliable results can be assessed by Jacobians. We performed such studies using GARLIC, our Generic Atmospheric Radiation LbL Infrared Code (see annual report 2013). The calculated Jacobians using algorithmic differentiation (see annual report 2014) referred to the 500 to 2000 cm^{-1} spectral range. Planets around different types of host stars (F, G, K, and M) were considered. Their atmospheres differ in temperature profile and tropospheric water concentrations. While the F star planet possesses a very strong temperature inversion in the stratosphere, it is absent in the M star planet.

The results are given in Table 4-3. It presents the condition numbers of Jacobians for three of four unknowns (i.e. one parameter is assumed to be known) for all four different planets and three different atmospheric altitudes. The atmospheric parameter excluded is denoted by "exc_X".

Surface	exc_CO₂	exc_H₂O	exc_O₃	exc_Temperature
F star planet	2.79e+04	1.26e+03	1.12e+03	1.39e+04
G star planet	5.41e+04	1.49e+03	3.02e+03	1.96e+04
K star planet	8.18e+04	1.65e+03	5.21e+03	2.66e+04
M star planet	1.17e+05	1.83e+03	8.46e+03	3.39e+04
15 km	exc_CO₂	exc_H₂O	exc_O₃	exc_Temperature
F star planet	4.17e+03	2.02e+03	1.63e+02	4.19e+03
G star planet	1.09e+03	2.16e+03	6.58e+01	1.36e+03
K star planet	1.39e+03	1.74e+03	7.02e+01	1.22e+03
M star planet	2.07e+03	1.29e+03	1.02e+02	1.56e+03
50 km	exc_CO₂	exc_H₂O	exc_O₃	exc_Temperature
F star planet	2.07e+03	1.28e+03	1.02e+02	1.56e+03
G star planet	1.13e+02	2.03e+02	1.97e+02	2.57e+01
K star planet	1.45e+02	4.36e+02	3.49e+02	7.73e+01
M star planet	3.05e+02	8.91e+02	7.67e+02	1.02e+02

Table 4-3: Condition numbers for different atmospheric parameters at three altitudes.

In most cases, the M star planet shows a larger condition number than the rest of the planets, most likely related to the missing temperature inversion in its stratosphere. The condition number is found to decrease in the planets with increasing temperature inversion. With the exclusion of one of the atmospheric parameters, the impact on the Jacobian matrices varies depending on the altitude considered. At the surface, the greatest variation occurs when CO₂ is excluded followed by the temperature.

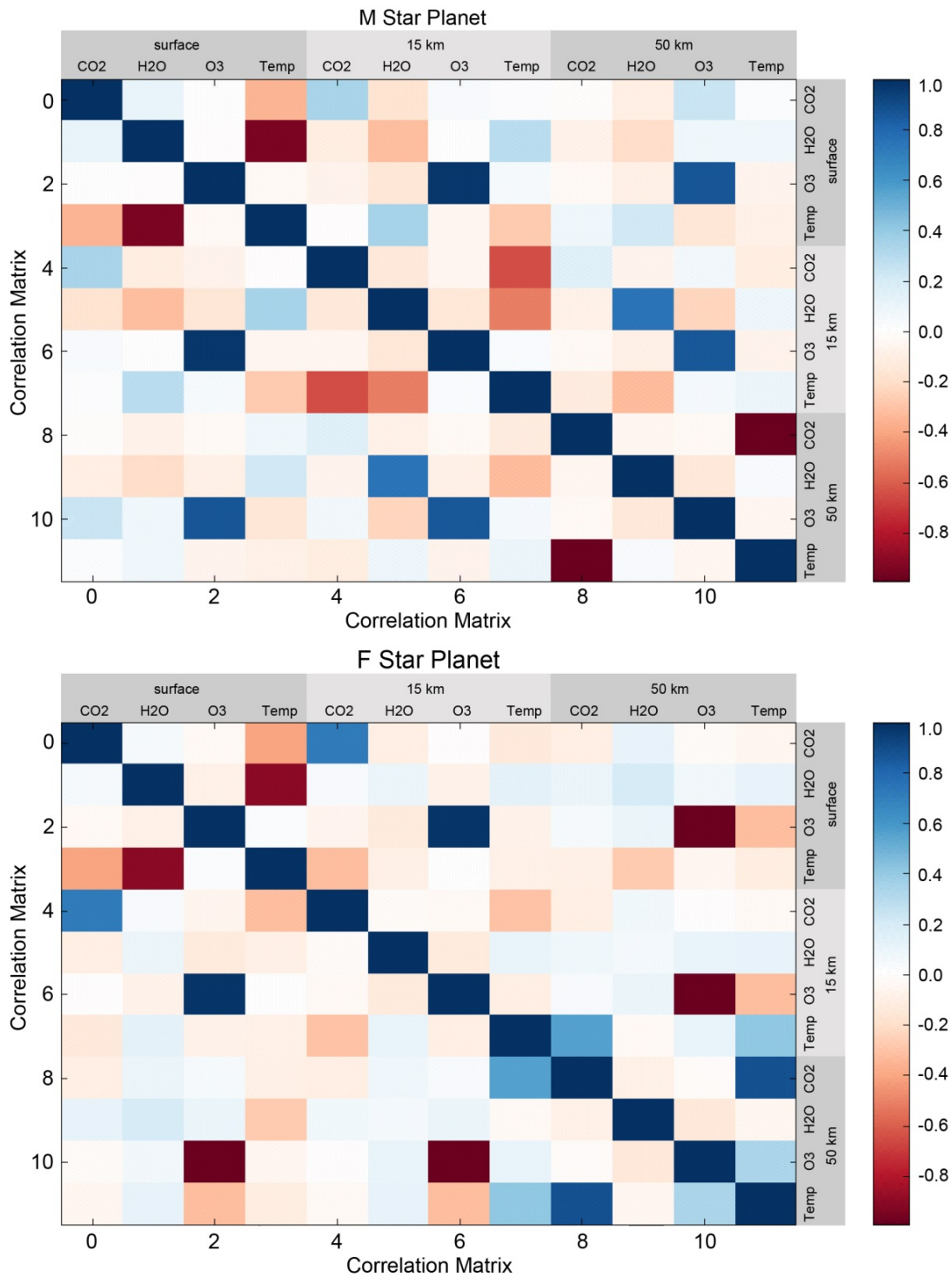


Fig. 4-14: Correlation matrices of the Jacobians of an M and F Earth-like planets.

Taking all three levels into account, the condition number greatly increases. With the exclusion of water vapor and temperature at 50 km, the condition number becomes small, especially in the case of the M star planet. This condition number is even smaller than in the atmosphere of the rest of the planets. In case that the temperature at the surface and troposphere is combined with the one at 50 km, the condition number for the M star planet reaches extremely large values.

Considering all parameters for all three atmospheric levels, the condition number reaches very large values. However, when taking into account a shorter wavelength range and all molecules, the condition number drops tremendously. This is also noticed with the combination of other atmospheric altitudes.

The correlation matrices (see Fig. 4-14) for the M star planet shows differences against the F star planet, especially for an altitude of 50 km, where the temperature inversion is absent. In general, the correlations for the M star planet at this altitude result to be larger. There is also a strong correlation between CO₂ absorption and the temperature at 15 km for the M star planet.

5. Documentation

5.1 Books and Book Contributions

Gottwald, M., Fritz, T., Breit, H., Schättler, B., Harris, A.: Mapping terrestrial impact craters with the TanDEM-X digital elevation model. In: Osinski, G.R., and Kring, D.A., eds., *Large Meteorite Impacts and Planetary Evolution V*, Geological Society of America Special Paper 518, 177-211, doi:10.1130/2015.2518(12)2000, 2015.

Rother, T.: *Greenfunktionen Klassischer Teilchen und Felder*. BoD Verlag Norderstedt, ISBN 978-3-7386-1338-4, 2015.

5.2 Journal Papers

Antón, M., Loyola, D., Roman, R., Vömel, H.: Validation of GOME-2/MetOp-A total water vapour column using reference radiosonde data from the GRUAN network. *Atmospheric Measurement Techniques*, 8(3), 1135-1145, Copernicus Publications, doi: 10.5194/amt-8-1135-2015, 2015.

Bai, J., Duhl, T., Hao, N.: Biogenic volatile compound emissions from a temperate forest, China: model simulation. *Journal of Atmospheric Chemistry* (10874), 1-31, doi: 10.1007/s10874-015-9315-3, 2015.

Buchwitz, M., Reuter, M., Schneising, O., Boesch, H., Guerlet, S., Dils, B., Aben, I., Armante, R., Bergamaschi, P., Blumenstock, T., Bovensmann, H., Brunner, D., Buchmann, B., Burrows, J.P., Butz, A., Chédin, A., Chevallier, F., Crevoisier, C.D., Deutscher, N.M., Frankenberg, C., Hase, F., Hasekamp, O.P., Heymann, J., Kaminski, T., Laeng, A., Lichtenberg, G., De Mazière, M., Noël, S., Notholt, J., Orphal, J., Popp, C., Parker, R., Scholze, M., Sussmann, R., Stiller, G.P., Warneke, T., Zehner, C., Bril, A., Crisp, D., Griffith, D.W.T., Kuze, A., O'Dell, C., Oshchepkov, S., Sherlock, V., Suto, H., Wennberg, P., Wunch, D., Yokota, T., Yoshida, Y.: The Greenhouse Gas Climate Change Initiative (GHG-CCI): Comparison and quality assessment of near-surface-sensitive satellite-derived CO₂ and CH₄ global data sets. *Remote Sensing of Environment*, 162, 344-362, doi:10.1016/j.rse.2013.04.024, 2015.

Cleaves, H.J., Meringer, M., Goodwin, J.T.: 227 Views of RNA: Is RNA Unique in Its Chemical Isomer Space? *Astrobiology*, 15(7), 538-558. doi: 10.1089/ast.2014.1213, 2015.

Coldewey-Egbers, M., Loyola, D., Koukouli, M.L., Balis, D., Lambert, J.-C., Verhoelst, T., Granville, J., Van Roozendaal, M., Lerot, C., Spurr, R., Frith, S., Zehner, C.: The GOME-type Total Ozone Essential Climate Variable (GTO-ECV) data record from the ESA Climate Change Initiative. *Atmospheric Measurement Techniques*, 8(9), 3923-3940, Copernicus Publications. doi: 10.5194/amt-8-3923-2015, 2015.

Ding, J., van der A, R., Mijling, B., Levelt, P.F., Hao, N.: NO_x emission estimates during the 2014 Youth Olympic Games in Nanjing. *Atmospheric Chemistry and Physics*, 15(16), 9399-9412, Copernicus Publications, doi: 10.5194/acp-15-9399-2015, 2015.

Doicu, A., Eremin, Y., Efremenko, D.S., Trautmann, T.: Methods with discrete sources for electromagnetic scattering by large axisymmetric particles with extreme geometries. *Journal of Quantitative Spectroscopy and Radiative Transfer*, 164, 137-146, <http://dx.doi.org/10.1016/j.jqsrt.2015.06.007>, 2015.

Grossi, M., Valks, P., Loyola, D., Aberle, B., Slijkhuis, S., Wagner, T., Beirle, S., Lang, R.: Total column water vapour measurements from GOME-2 MetOp-A and MetOp-B. *Atmospheric Measurement Techniques*, 8, 1111-1133, doi: 10.5194/amt-8-1111-2015, 2015.

Hassinen, S., Balis, D., Bauer, H., Begoin, M., Delcloo, A., Eleftheratos, K., Gimeno Garcia, S., Granville, J., Grossi, M., Hao, N., Hedelt, P., Hendrick, F., Hess, M., Heue, K.-P., Hovila, J., Jønch-Sørensen, H.,

Kalakoski, N., Kauppi, A., Kiemle, S., Kins, L., Koukouli, M. E., Kujanpää, J., Lambert, J.-C., Lang, R., Lerot, C., Loyola, D., Pedernana, M., Pinardi, G., Romahn, F., Van Roozendaal, M., Lutz, R., De Smedt, I., Stammes, P., Steinbrecht, W., Tamminen, J., Theys, N., Tilstra, L. G., Tuinder, O.N.E., Valks, P., Zerefos, C., Zimmer, W., and Zyrichidou, I.: Overview of the O3M SAF GOME-2 operational atmospheric composition and UV radiation data products and data availability. *Atmospheric Measurement Techniques Discussion*, 8, 6993–7056, 2015.

Ilardo, M., Meringer, M., Freeland, S.J., Rasulev, B., Cleaves, H.J.: Extraordinarily adaptive properties of the genetically encoded amino acids. *Scientific Reports*, 5, 1-6, Nature Publishing Group, 2015.

Koukouli, M.E., Lerot, C., Lambert, J.-C., Goutail, F., Granville, J., Pommereau, J.-P., Balis, D., Zyrichidou, I., Van Roozendaal, M., Labow, G., Frith, S.M., Loyola, D., Coldewey-Egbers, M., Spurr, R. and Zehner, C.: Evaluating a new homogeneous total ozone climate data record from GOME/ERS-2, SCIAMACHY/Envisat and GOME-2/MetOp-A. *Journal of Geophysical Research*, 120, 12296-12312, doi:10.1002/2015JD023699, 2015.

Letu, H., Bao, Y., Xu, J., Qing, S., Bao, G.: Radiative properties of cirrus clouds based on hexagonal and spherical ice crystals models. *Spectroscopy and Spectral Analysis*, 35(5), 1165-1168, doi: 10.3964/j.issn.1000-0593(2015)05-1165-04, 2015.

Román, R., Antón, M., Cachorro, V.E., Loyola, D., Ortiz de Galisteo, J.P., de Frutos, A., Romero-Campos, P.M.: Comparison of total water vapor column from GOME-2 on MetOp-A against ground-based GPS measurements at the Iberian Peninsula. *Science of the Total Environment*, 533, 317-328 doi: 10.1016/j.scitotenv.2015.06.124, 2015.

Rother, T.: Violation of a Bell-like inequality by a combination of Rayleigh scattering with a Mach-Zehnder setup. *Journal of Quantitative Spectroscopy and Radiative Transfer*, doi:10.1016/j.jqsrt.2015.09.002, 2015.

Schreier, F., Gimeno Garcia, S., Vasquez, M., Xu, J.: Algorithmic vs. finite difference Jacobians for infrared atmospheric radiative transfer. *Journal of Quantitative Spectroscopy and Radiative Transfer*, 164, 147-160, doi: 10.1016/j.jqsrt.2015.06.002, 2015.

Weber, M., Steinbrecht, W., Roth, C., Coldewey-Egbers, M., van der A, R., Degenstein, D., Fioletov, V.E., Frith, S., Froidevaux, L., Long, C., Loyola, D., Wild, J.: Stratospheric Ozone. In: *State of the Climate in 2014*, *Bulletin of the American Meteorological Society*, 96(7), 44-546, 2015.

5.3 Conference Proceeding Papers and Presentations

Azam, F., Noël, S., Eichmann, K.-U., Richter, A., Wittrock, F., Hilboll, A., Schönhardt, A., Buchwitz, M., Reuter, M., Rozanov, A., Bovensmann, H., Burrows, J.P., Lerot, C., Daan, H., Keppens, A., Theys, N., De Smedt, I., Van Roozendaal, M., Lichtenberg, G., Gretschan, S., Schreier, F., Gimeno-García, S., Meringer, M., Doicu, A., Brizzi, G., Dehn, A., Fehr, T.: Development and verification of SCIAMACHY operational ESA Level 2 version 6/7 products. *Proceedings of ATMOS 2015*, SP-735, ESA Atmospheric Science Conference, University of Crete, Heraklion, Greece, 2015.

Cleaves, H.J., Meringer, M., Goodwin, J.T.: 227 Views of RNA: Is RNA Unique in Its Chemical Isomer Space? *AbSciCon – Astrobiology Science Conference 2015*, Chicago, IL, USA, 2015.

Coldewey-Egbers, M., Loyola, D., Braesicke, P., Dameris, M., Van Roozendaal, M., Lerot, C., Koukouli, M., Balis, D.: Global and Regional Ozone Trends Using 20 Years of European Satellite Data. *Proceedings of ATMOS 2015*, SP-735, ESA Atmospheric Science Conference, University of Crete, Heraklion, Greece, 2015.

Engelen, R., Flemming, J., Hedelt, P., Inness, A., Suttie, M., Valks, P.: Assimilating Volcanic SO₂ Satellite Data in the Copernicus Atmosphere Monitoring Service Global Data Assimilation System. *Proceedings of ATMOS 2015*, SP-735, ESA Atmospheric Science Conference, University of Crete, Heraklion, Greece, 2015.

- Gottwald, M., Fritz, T., Breit, H., Schättler, B., Harris, A.: How can the TanDEM-X Digital Elevation Model Support Terrestrial Impact Crater Studies? Bridging the Gap III: Impact Cratering in Nature, Experiments and Modeling, Freiburg, Deutschland, 2015.
- Gottwald, M., Fritz, T., Breit, H., Schättler, B., Harris, A.: The TanDEM-X DEM – Status of the New Dataset for Studying Topography of the Global Impact Crater Record. 78th Annual Meeting Meteoritical Society 2015, Berkeley, Kalifornien, USA, 2015.
- Gottwald, M., Krieg, E., Lichtenberg, G., Reissig, K., Noël, S., Bramstedt, K., Bovensmann, H.: SCIAMACHY Operations History and the New Level 1b Product – an Approach for Long-term Data Preservation. Proceedings of ATMOS 2015, SP-735, ESA Atmospheric Science Conference, University of Crete, Heraklion, Greece, 2015.
- Gottwald, M.: Irdische Einschlagkrater im Radarbild. *Sterne und Weltraum*, 4, 26-37, 2015.
- Gottwald, M.: IMPAKT-SPUREN – Terrestrische Einschlagkrater im Bild von TanDEM-X. Lecture on the occasion of the opening of the exhibition IMPAKT-SPUREN – Einschlagkrater der Erde im Radarbild der TanDEM-X Mission, 26 November 2015, Nördlingen, Germany, 2015.
- Hamidouche, M., Trautmann, T., Gottwald, M., Lichtenberg, G.: The MERLIN Lidar Instrument for Atmospheric CH₄: Quality and Performance Monitoring. In: Proceedings of AGU Fall Meeting. AGU Fall Meeting, San Francisco, CA, USA, 2015.
- Hamidouche, M., Trautmann, T., Gottwald, M., Lichtenberg, G.: The new MERLIN Instrument for Atmospheric Methane: Quality and Performance Monitoring. Gordon Research Conference: Radiation and Climate, Lewiston, USA, 2015.
- Hamidouche, M.: In-flight ISRF retrieval. ESA Workshop on requirements, calibration and characterization of the ISRF, Noordwijk, The Netherlands, 2015.
- Hamidouche, M.: Infrared Astronomy: Unveiling the Hidden Universe. Infrarottechnik – Grundlagen, Trends, moderne Anwendungen, 19-22 October 2015, Wessling, Germany, 2015.
- Hao, N., Van Roozendaal, M., Ding, A. J., Hendrick, F., Staedt, S., Ding, J., Shen, Y., van der A, R., Valks, P.: About two years of MAXDOAS measurements of air pollutants at SORPES in Nanjing, China: validation of satellite observation and model simulation. Dragon 3 Symposium, Interlaken, Switzerland, 2015.
- Hao, N., Van Roozendaal, M., Ding, A. J., Hendrick, F., Staedt, S., Ding, J., van der A, R., Valks, P.: Validation of satellite measurements and model simulation in China using MAXDOAS measurements. 7th International DOAS workshop, Brussels, Belgium, 2015.
- Hao, N., Ding, A.J., Van Roozendaal, M., Hendrick, F., Shen, Y., Valks, P.: Two years of MAXDOAS measurements of air pollutants at SORPES station in Nanjing, China. In: Geophysical Research Abstracts, Copernicus Publications, European Geosciences Union General Assembly 2015, Vienna, Austria, 2015.
- Hao, N., Ding, A.J., Van Roozendaal, M., Hendrick, F., Shen, Y., Valks, P.: MAXDOAS measurements of NO₂, HONO, SO₂ and HCHO at SORPES station in Nanjing, China. 2015 EUMETSAT Meteorological Satellite Conference, Toulouse, France, 2015.
- Hao, N., Wang, Z., Hendrick, F., Van Roozendaal, M., Holla, R., Valks, P.: Long-term MAX-DOAS measurement of trace gases and aerosol in the Environmental Research Station Schneefernerhaus. Virtual Alpine Observatory Symposium 2015, Salzburg, Austria, 2015.
- Hao, N., Loyola, D., Van Roozendaal, M., Lerot, C., Spurr, R., Koukouli, M., Zyrichidou, I., Inness, A., Valks, P., Zimmer, W., Balis, D.: The operational Near-Real-Time Total Ozone Retrieval Algorithm for GOME-2 on MetOp-A & MetOp-B and perspectives for TROPOMI/S5P. Proceedings of ATMOS 2015, SP-735, ESA Atmospheric Science Conference, University of Crete, Heraklion, Greece, 2015.
- Hedelt, P., Valks, P., Loyola, D.: Monitoring volcanic SO₂ emissions using GOME-2/Metop-A & -B. Proceedings of ATMOS 2015, SP-735, ESA Atmospheric Science Conference, University of Crete, Heraklion, Greece, 2015.

- Hedelt, P., Valks, P., Loyola, D.: Monitoring the Bardarbunga eruption using GOME-2/Metop-A & -B. ISRSE36, Berlin, Germany, 2015.
- Hedelt, P., Valks, P., Loyola, D.: Monitoring volcanic SO₂ emissions using GOME-2/Metop-A & -B. EUMETSAT Meteorological Satellite Conference, Toulouse, France, 2015
- Heue, K.-P., Hao, N., Valks, P., Loyola, D., Miles, G., Siddans, R., Raphoe, N.: Tropical Tropospheric Ozone observed from GOME_2 and perspectives for TROPOMI. Proceedings of ATMOS 2015, SP-735, ESA Atmospheric Science Conference, University of Crete, Heraklion, Greece, 2015.
- Koukoulis, M.L., Balis, D., Theys, N., Brenot, H., van Gent, J., Hendrick, F., Wang, T., Valks, P., Hedelt, P., Lichtenberg, G., Richter, A., Krotkov, N.: OMI/Aura, SCIAMACHY/Envisat and GOME2/MetopA Sulphur Dioxide Estimates; the case of Eastern Asia. Proceedings of ATMOS 2015, SP-735, ESA Atmospheric Science Conference, University of Crete, Heraklion, Greece, 2015.
- Lichtenberg, G., Slijkhuis, S., Aberle, B., Scherbakov, D., Meringer, M., Noël, S., Bramstedt, K., Liebing, P., Bovensmann, H., Snel, R., Krijger, M., Van Hees, R., van der Meer, P., Lerot, C., Fehr, T., Dehn, A., Brizzi, G.: SCIAMACHY: New Level 0-1 Processor and Plans for the Future. Proceedings of ATMOS 2015, SP-735, ESA Atmospheric Science Conference, University of Crete, Heraklion, Greece, 2015.
- Lichtenberg, G., Slijkhuis, S., Aberle, B., Scherbakov, D., Meringer, M., Noël, S., Bramstedt, K., Liebing, P., Bovensmann, H., Snel, R., Krijger, M., Van Hees, R., van der Meer, P., Lerot, C., Fehr, T., Dehn, A., Brizzi, G.: SCIAMACHY: Impact of calibration changes on SCIAMACHY CO retrievals. International Workshop on Greenhouse Gas Measurements from Space (IWGGMS) #11, Caltech Pasadena, U.S., June 2015
- Loyola, D., Efremenko, Dmitry S., Hedelt, P., Pedernana, M.: Extreme fast volcanic SO₂ plume height retrieval from UVN sensors. Proceedings of ATMOS 2015, SP-735, ESA Atmospheric Science Conference, University of Crete, Heraklion, Greece, 2015.
- Meringer, M., Gretschan, S., Lichtenberg, G., Hilboll, A., Richter, A., Burrows, J.P.: Limb-Nadir Matching for Tropospheric NO₂: A New Algorithm in the SCIAMACHY Operational Level 2 Processor. Proceedings of ATMOS 2015, SP-735, ESA Atmospheric Science Conference, University of Crete, Heraklion, Greece, 2015.
- Meringer, M.: Mapping the Chemical Universe of Biomolecules for Astrobiology. ELSI Seminar, Tokyo, Japan, 2015.
- Reitebuch, O., Wandinger, U., Lehmann, V., Nikolaus, I., Potthast, R., Schmidt, K., Weissmann, M., Freudenthaler, V.: Experimental Validation of Aeolus with the ALADIN Airborne Demonstrator. ADM-Aeolus Science & Cal/Val Workshop, Frascati, Italy, 2015.
- Reitebuch, O., Huber, D., Marksteiner, U., Nikolaus, I.: Algorithm Baseline for Aeolus L1B Product and Calibration. ADM-Aeolus Science & Cal/Val Workshop, Frascati, Italy, 2015.
- Rother, T.: Violation of a Bell-like inequality by a combination of Rayleigh scattering with a Mach-Zehnder interferometry. 15th Electromagnetic and Light Scattering Conference (ELS-XV), Leipzig, Germany, 2015
- Rother, T.: Die seltsamen Eigenschaften des Lichtes. Lecture on the occasion of the DLR SchoolLab award 2015, 26 November 2015, Neustrelitz, Germany, 2015.
- Schmidt, K., Rother, T.: On the Independent Scattering Assumption in the Electromagnetic and Acoustic Case. 15th Electromagnetic and Light Scattering Conference (ELS-XV), Leipzig, Germany, 2015.
- Schmidt, D., Gimeno García, S., Schreier, F., Lichtenberg, G.: Impact of Spectroscopic Line Parameters on Carbon Monoxide Column Density Retrievals from Shortwave Infrared Nadir Observations. Proceedings of ATMOS 2015, SP-735, ESA Atmospheric Science Conference, University of Crete, Heraklion, Greece, 2015.
- Schreier, F.: Atmosphärische IR-Fernerkundung – Strahlungstransport und Inversion. Infrarottechnik – Grundlagen, Trends, moderne Anwendungen, 19-22 October 2015, Wessling, Germany, 2015.

- Schreier, F., Gimeno García, S., Hedelt, P., Vasquez, M.: GARLIC – A Generic Atmospheric Radiation Line-by-line Infrared Code for Earth and Planetary Science. Atmosphere Science in the Context of CHEOPS, TESS, K2 and PLATO, Berlin, Germany.
- Schreier, F., Lichtenberg, G.: Validation of Vertical Profiles & Column Densities Retrieved from Nadir IR Sounders. 7th GOSAT RA PI Meeting, Caltech, Pasadena, USA, 2015.
- Schreier, F., Gimeno Garcia, S., Kohlert, D.: How to Tackle the Computational Challenges of Line-by-line Modelling. Spectroscopy of Exoplanets, Cumberland Lodge, Great Park, Windsor, UK, 2015.
- Slijkhuis, S., Aberle, B., Coldewey-Egbers, M., Loyola, D., Dehn, A., Fehr, T.: GOME/ERS-2: New Homogeneous Level 1B Data from an old Instrument. Proceedings of ATMOS 2015, SP-735, ESA Atmospheric Science Conference, University of Crete, Heraklion, Greece, 2015.
- Theys, N., De Smedt, I., van Gent, J., Danckert, T., Hörmann, C., Hedelt, P., Wagner, T., Van Roozendael, M., Veeffkind, P.: Sulfur dioxide retrievals from TROPOMI : algorithmic developments, verification on synthetic spectra and application to OMI measurements. Proceedings of ATMOS 2015, SP-735, ESA Atmospheric Science Conference, University of Crete, Heraklion, Greece, 2015.
- Trautmann, T.: Space-borne Monitoring of the Earth's Atmospheric Composition. Invited lecture, Climate Change Research Centre, University of New South Wales, Sydney, Australia, February 2015.
- Valks, P., Hao, N., Hedelt, P., Grossi, M., Loyola, D., Pinardi, G., Theys, N., Van Roozendael, A., Delcloo, A., Wagner, T., Bauer, H., and Zimmer, W.: Tropospheric trace-gas column observations from the GOME-2 instruments on MetOp-A and MetOp-B. In: Geophysical Research Abstracts, Copernicus Publications, European Geosciences Union General Assembly 2015, Vienna, Austria, 2015.
- Valks, P., Begoin, M., Hao, N., Hedelt, P., Heue, K.-P., Grossi, M., Loyola, D., De Smedt, I., Pinardi, G., and Van Roozendael, M.: Trace gas column observations from GOME-2 on MetOp. EUMETSAT Meteorological Satellite Conference, Toulouse, France, 2015.
- Valks, P., Hao, N., Hedelt, P., Begoin, M., Grossi, M., Loyola, D., Pinardi, G., Theys, N., De Smedt, I., Van Roozendael, M., and Wagner, T.: Operational trace-gas column observations from GOME-2. Proceedings of ATMOS 2015, SP-735, ESA Atmospheric Science Conference, University of Crete, Heraklion, Greece, 2015.
- Vasquez, M., Schreier, F., Trautmann, T.: A First Look at Inverse Problems for the Atmospheres of M and G Earth-like Planets. Atmosphere Science in the Context of CHEOPS, TESS, K2 and PLATO, Berlin, Germany, 2015.
- Xu, J., Schreier, F., Doicu, A., Birk, M., Wagner, G., Trautmann, T.: Remote Sensing of Stratospheric Trace Gases by TELIS. Proceedings of ATMOS 2015, 735, 1-6. Proceedings of ATMOS 2015, SP-735, ESA Atmospheric Science Conference, University of Crete, Heraklion, Greece, 2015.
- Xu, J., Schreier, F., Kenntner, M., Fix, A., Trautmann, T.: Retrieval of Atmospheric Temperature from Airborne Microwave Radiometer Observations. Proceedings of ATMOS 2015, SP-735, Atmospheric Science Conference, University of Crete, Heraklion, Greece, 2015.
- Xu, J., Schreier, F., Doicu, A. and Trautmann, T.: Observing atmospheric composition and temperature by far infrared and microwave emission sounding. 4th International Symposium on Atmospheric Light Scattering and Remote Sensing, 1-5 June 2015, Wuhan, China, 2015.

5.4 Attended Conferences

ADM-Aeolus Science & Cal/Val Workshop, Frascati, Italy, 10-13 February 2015.

Atmosphere Science in the Context of CHEOPS, TESS, K2 and PLATO, Berlin, Germany, 2-4 March 2015.

European Geosciences Union General Assembly 2015, Vienna, Austria, 12-17 April 2015.

ELSI Seminar, Tokyo, Japan, 22 April 2015.

ISRSE36, Berlin, Germany, 10-15 May 2015.

ESA Workshop on requirements, calibration and characterization of the ISRF, Noordwijk, The Netherlands, 28 May 2015.

4th International Symposium on Atmospheric Light Scattering and Remote Sensing, Wuhan, China, 1-5 June 2015.

ESA Atmospheric Science Conference, University of Crete, Heraklion, Greece, 8-12 June 2015.

7th GOSAT RA PI Meeting, Caltech, Pasadena, California, USA, 15 June 2015.

15th Electromagnetic and Light Scattering Conference (ELS-XV), Leipzig, Germany, 21-26 June 2015.

Dragon 3 Symposium, Interlaken, Switzerland, 22-26 June 2015.

7th International DOAS workshop, Brussels, Belgium, 6-8 July 2015.

AbSciCon – Astrobiology Science Conference 2015, Chicago, IL, USA, 15-19 July 2015.

Spectroscopy of Exoplanets, Cumberland Lodge, Great Park, Windsor, UK, 24-26 July 2015.

Gordon Research Conference: Radiation and Climate, Lewiston, Maine, USA, 26-31 July 2015.

78th Annual Meeting Meteoritical Society 2015, Berkeley, California, USA, 27-31 July 2015.

2015 EUMETSAT Meteorological Satellite Conference, Toulouse, France, 21-25 September 2015.

Bridging the Gap III: Impact Cratering in Nature, Experiments and Modeling, Freiburg, Germany, 21-26 September 2015.

Earth Observation (EO) Open Science 2.0 Conference, ESA-ESRIN, Frascati, Italy, 12-14 October 2015.

Virtual Alpine Observatory Symposium 2015, Salzburg, Austria, 27-30 October 2015.

AGU Fall Meeting, San Francisco, California, USA, 14-18 December 2015.

5.5 Academic Degrees

- Gimeno García, S.: Simulation of solar radiative transfer and comparison with spectro-radiometric measurements. Dissertation, Faculty of Civil, Geo and Environmental Engineering, Technical University of Munich. (Supervisors: Prof. Dr. Richard Bamler and PD Dr. A. Doicu)
- Hochstaffl, P.: Master thesis, Institute of Atmospheric and Cryospheric Sciences, University of Innsbruck, completed in February 2016. (Supervisors: Dr. F. Schreier and Prof. Dr. T. Karl, University Innsbruck)
- Risse, E.: The effect of air pollution regulations under the influence of different meteorological conditions over China. (Supervisors: Dr. N. Hao, Prof. Dr T. Trautmann and Prof. Dr. J. Sesterhenn, Technical University of Berlin)
- Sasi, S.: Cloud internal mixing model for ozone retrieval. Master thesis, Faculty of Civil, Geo and Environmental Engineering, Technical University of Munich, completed in March 2015. (Supervisor: PD Dr. A. Doicu)
- Schüssler, O.: Combined Inversion Methods for UVVIS Nadir Sounding. Dissertation, Faculty of Civil, Geo and Environmental Engineering, Technical University of Munich. (Supervisors: Prof. Dr. Richard Bamler, PD Dr. A. Doicu and Dr. D. Loyola)
- Städt, S.: Mini MAX-DOAS measurements of air pollutants over China. Master thesis, Free University of Berlin. (Supervisors: Dr. N. Hao and Prof. Dr. J. Fischer, Free University of Berlin)
- Szajkowski, M.: Development of pre- and post-processing tools for the analysis of microwave temperature profiling observations. Master thesis, Wrocław University of Technology. (Supervisors: Dr. F. Schreier and Prof. Dr. W. Urbańczyk, Wrocław University of Technology)
- Wang, Z.: MAX-DOAS observations of trace gases and aerosol from the Environmental Research Station Schneefernerhaus. Dissertation. Faculty of Civil, Geo and Environmental Engineering, Technical University of Munich. (Supervisors: Dr. N. Hao and PD. Dr. A. Doicu)
- Xu, J.: Inversion for Limb Infrared Atmospheric Sounding. Dissertation, Civil Engineering and Surveying, Technical University of Munich, thesis defence in May 2015. (Supervisors: Prof. Dr. Richard Bamler, PD. Dr. A. Doicu, Dr. F. Schreier and Prof. Dr. S. Bühler, University of Hamburg)

Abbreviations and Acronyms

AAI	Aerosol Absorbing Index
AC	Atmospheric Composition
ADM-Aeolus	Atmospheric Dynamics Mission Aeolus
AERONET	Aerosol Robotic Network
ALH	Aerosol Layer Height
AMF	Air Mass Factor
AOD	Aerosol Optical Depth
APEC	Asian Pacific Economic Cooperation
ATBD	Algorithm Theoretical Baseline Document
ATC	Active Thermal Control
ATCOR	Atmospheric & Topographic Correction
ATP	Atmosphärenprozessoren
BIRA-IASB	Belgisch Instituut voor Ruimte-Aëronomie / Institut d'Aéronomie Spatiale de Belgique
BIRRA	Beer Infrared Retrieval Algorithm
BRF	Bidirectional Reflectance Factor
BVOC	Biogenic Volatile Organic Compounds
CA	Cloud Albedo
CAL	Clouds as Scattering Layers
CALIOP	Cloud-Aerosol Lidar with Orthogonal Polarization
CALIPSO	Cloud-Aerosol Lidar and Infrared Pathfinder Satellite Observation
CAMS	Copernicus Atmospheric Monitoring Service
CBMZ	Carbon-Bond Mechanism version Z
CCD	Convective Cloud Differential
CCI	Climate Change Initiative
CDOME	Coupled Discrete Ordinate with Matrix Exponential
CDOP	Continuous Development and Operations Phase
CF	Cloud Fraction
CFI	Customer Furnished Item
CHSH	Clauser-Horne-Shimony-Holt
CME	Chinese Ministry of Environment
CNES	Centre Nationale d'Études Spatiales
COT	Cloud Optical Depth
CRB	Cloud as Reflecting Boundaries
CTH	Cloud Top Height
CTH/P	Cloud Top Height/Pressure
CTI	Configurable Transfer Item
DAOD	Differential Absorption Optical Depth
DB	Database
DFD	Deutsches Fernerkundungsdatenzentrum
DLR	Deutsches Zentrum für Luft- und Raumfahrt
DOAS	Differential Optical Absorption Spectroscopy
DP	Discrepancy Principle
DSCD	Differential Slant Column Densities
DU	Dobson Unit
E2S	End-to-End Simulator
ECV	Essential Climate Variable
EEE	Expected Error Estimation
ENVISAT	Environmental Satellite
EO	Earth Observation
EOC	Earth Observation Center
EOS	Earth Observing System
EPR	Einstein-Podolsky-Rosen
ERS	European Remote Sensing Satellite
ESA	European Space Agency

ESAS	Earth's Surface-Atmosphere System
ESRL	Earth System Research Laboratory
ESTEC	European Space Research and Technology Center
EUMETSAT	European Organisation for the Exploitation of Meteorological Satellites
FDDA	Four Dimensional Data Assimilation
FEMWAT	Finite Element Method Water
FOCC	Flight Operation Control Center
FOS	Flight Operation Segment
FPN	Fixed Pattern Noise
FRESCO	Fast Retrieval Scheme for Clouds from the Oxygen A-band
GARLIC	Generic Atmospheric Radiation Line-by-Line Infrared Code
GCAPS	Generic Calibration Processing System
GCV	Generalized Cross-Validation
GDP	GOME Data Processor
GMD	Global Monitoring Division
GODFIT	GOME Direct Fitting
GOME	Global Ozone Monitoring Experiment
GTO	GOME-type Total Ozone
HALO	High Altitude and Long Range Research Aircraft
HK	Housekeeping
ILM	Inverse Learning Machine
IMF	Institut für Methodik der Fernerkundung
IPA	Institut für Physik der Atmosphäre
IPDA	Integrated Path Differential Absorption
IPY	International Polar Year
IR	Infrared
ITCZ	Inter-tropical Convergence Zone
IUP-IFE	Institut für Umweltphysik / Institut für Fernerkundung
KNMI	Koninklijk Nederlands Meteorologisch Instituut
L0	Level 0
L1	Level 1
L2	Level 2
L2PF	Level 2 Processing Facility
LbL	Line-by-Line
LC	L-Curve
LER	Lambertian Equivalent Reflectance
LIDORT	Linearized Discrete Ordinate Radiative Transfer
LLI	Life Limited Item
LO	Local Oscillator
LOA	Laboratoire d'Optique Appliquée
MAX-DOAS	Multi-Axis DOAS
MDS	Measurement Data Set
MEIC	Multiresolution Emissions Inventory for China
MERLIN	Methane Remote Sensing Lidar Mission
MetOp	Meteorological Operational Polar Satellites of EUMETSAT
ML-CIRRUS	Midlatitude Cirrus
MLE	Microwave Likelihood Estimation
MLS	Microwave Limb Sounder
MODIS	Moderate Resolution Imaging Spectroradiometer
MOSAIC	Model for Simulating Aerosol Interactions and Chemistry
MOZART	Model for Ozone and Related Chemical Tracers
MPIC	Max-Planck-Institut für Chemie
MSG	METEOSAT Second Generation
MTG	METEOSAT Third Generation
MTG-S	METEOSAT Third Generation Sounder
MTP	Microwave Temperature Profiler

NASA	National Aeronautics and Space Administration
NCEP	National Centers for Environmental Prediction
NCEP FNL	NCEP Final
NDACC	Network for the Detection of Atmospheric Composition Change
netCDF	Network Common Data Format
NIR	Near-Infrared
NLC	Noctilucent Cloud
NRT	Near-realtime
NSO	Netherlands Space Office
O3M	Ozone Monitoring
OBM	Optical Bench Module
OCR	Operations Change Request
OCRA	Optical Cloud Recognition Algorithm
ODE	Ozone Depletion Event
OMI	Ozone Monitoring Instrument
OMPS	Ozone Mapping and Profiler Suite
ORR	Operational Readiness Review
OSDF	Orbit Sequence Definition File
PDGS	Payload Data Ground Segment
PF	Processing Facility
PIK	Processor Integration Kit
PILS	Profile Inversion for Limb Sounding
PM	Particulate Matter
PMD	Polarization Measurement Device
PSTG	Polar Space Task Group
QBO	Quasi-Biennial Oscillations
RAL	Rutherford Appleton Laboratory
RGB	Red-Green-Blue
RMS	Root Mean Square
ROCINN	Retrieval of Cloud Information using Neural Networks
RT	Radiative Transfer
RTE	Radiative Transfer Equation
RTS	RT Solutions
S4	Sentinel-4
S5	Sentinel-5
S5P	Sentinel-5 Precursor
SAA	South Atlantic Anomaly
SACURA	Semi-Analytical Cloud Retrieval Algorithm
SAF	Satellite Application Facility
SCD	Slant Column Density
SCIAMACHY	Scanning Imaging Absorption Spectrometer for Atmospheric Chartography
SCIATRAN	Radiative transfer model for SCIAMACHY
SEVIRI	Spinning Enhanced Visible and Infrared Imager
SHADOZ	Southern Hemisphere Additional Ozonesondes
SOC	Stratospheric Ozone Column
SOST	SCIAMACHY Operations Support Team
SQWG	SCIAMACHY Quality Working Group
SRON	Netherlands Institute for Space Research
STP	Space Task Group
STS	Stratosphere-Troposphere Separation
SWIR	Shortwave Infrared
SZA	Sun Zenith Angle
TC	Thermal Control
TCCON	Total Carbon Column Observing Network
TIRAMISU	Temperature Inversion Algorithm for Microwave Sounding
TMS	Truncated Multi+Single

TOZ	Total Ozone Column
TROPOMI	Tropospheric Ozone Monitoring Instrument
TTOC	Tropical Tropospheric Ozone Columns
TUM	Technical University Munich
UFS	Umwelt Forschungsstation Schneefernerhaus
UPAS	Universal Processor for UV/VIS Atmospheric Spectrometers
UTC	Coordinated Universal Time
UTLS	Upper Troposphere Lower Stratosphere
UV	Ultraviolet
UVN	UV-Vis-NIR
VCD	Vertical Column Density
VIS	Visible
VOC	Volatile Organic Compound
VZA	View Zenith Angle
WMO	World Meteorological Organization
WRF	Weather Research and Forecasting
WRUT	Wroclaw University of Technology

DLR at a Glance

DLR is the national aeronautics and space research center of the Federal Republic of Germany. Its extensive research and development work in aeronautics, space, energy, transport and security is integrated into national and international cooperative ventures. In addition to its own research, as Germany's Space Agency, DLR has been given responsibility by the federal government for the planning and implementation of the German space program. DLR is also the umbrella organization for the nation's largest project management agency.

Approximately 8000 people are employed at 16 locations in Germany: Cologne (headquarters), Augsburg, Berlin, Bonn, Braunschweig, Bremen, Göttingen, Hamburg, Jülich, Lampoldshausen, Neustrelitz, Oberpfaffenhofen, Stade, Stuttgart, Trauen and Weilheim. DLR has also offices in Brussels, Paris, Tokyo and Washington, D.C.

Remote Sensing Technology Institute Institut für Methodik der Fernerkundung

DLR's Remote Sensing Technology Institute (IMF) is located in Oberpfaffenhofen, Berlin-Adlershof, Bremen and Neustrelitz.

IMF carries out research and development for retrieving geoinformation from remote sensing data. It conducts basic research on physical principles of remote sensing and develops algorithms, techniques, and operational processing systems for synthetic aperture radar, optical remote sensing, and spectrometric sounding of the atmosphere. The processing systems are in operational use for national, European, and international Earth observation missions.

For preparation and in support of space missions, IMF operates a suite of optical airborne sensors and laboratories. The institute contributes its expertise to novel sensor and mission concepts.

The German Remote Sensing Data Center (DFD) and IMF form DLR's Earth Observation Center (EOC).



DLR

**Deutsches Zentrum
für Luft- und Raumfahrt e.V.**

in der Helmholtz-Gemeinschaft

Institut für Methodik der Fernerkundung

Oberpfaffenhofen
82234 Weßling

www.dlr.de/eoc